Control of a bidirectional DC-DC converter for grid-connected electric vehicles

João Jorge Teodoro Coelho

Supervised by:

Prof. Dr. Américo Vicente Teixeira Leite

Prof. Dra. Ângela Paula Barbosa de Silva Ferreira

Prof. Dr. Alberto Vinicius de Oliveira

Bragança

2018-2019

Control of a bidirectional DC-DC converter for grid-connected electric vehicles

João Jorge Teodoro Coelho

Dissertation presented to the School of Technology and Management of Polytechnic Institute of Bragança to the Fulfillment of the Requirements for the Master of Science Degree in Industrial Engineering (Electrical Engineering branch), in the scope of Double Degree with Federal University of Technology - Paraná

Supervised by:

Prof. Dr. Américo Vicente Teixeira Leite

Prof. Dra. Ângela Paula Barbosa de Silva Ferreira

Prof. Dr. Alberto Vinicius de Oliveira

Bragança

2018-2019

Dedication

To my parents,

Edson Estevam Coelho and Eva Clair Teodoro Coelho.

Acknowledgments

I would like to acknowledge firstly to God, for the opportunity to conclude the biggest stage of my life.

Secondly, I want to express my acknowledgments to the Federal University of Technology - Paraná (UTFPR), Campus Toledo, for the years of learning and for all the provided background, and also, I acknowledge the Polytechnic Institute of Bragança (IPB), for the given opportunity to develop this research. I would like to thank both institutions for the opportunity of studying abroad and for all the effort made to accomplish this objective.

Furthermore, I appreciate all the provided support and effort by my menthors, professor Ph.D. Vicente Leite, professor Ph.D. Ângela Ferreira and professor Ph.D. Alberto Vinicius de Oliveira during the development of this project. A special thanks to professor José Batista, who has provided all the needed components to the development of the experimental tests.

Equally important, I would like to thank my relatives, for all the given support and encouragement during my studies and difficulty moments.

In addition, I acknowledge all the exchanged support and knowledge with my laboratory colleagues, in special, Matheus Montanini, for all the provided support in the development of this project.

Finally, I would like to thank all my friends, and specially my girlfriend, Ana Marques, for the given support during the difficulty moments. Without them, this thesis would not be possible.

Abstract

Due the increasing concerns about air pollution which contributes for the global warming growth, there is a vast dissemination of Electric Vehicle (EV) worldwide, considering that those vehicles are not polluting gases emitters and are pondered as clean means of transportation.

With an increasing projection for those vehicles on next years, and due to the big amount of EV unities spread around the globe, numerous researches have been studying the utilization of those vehicles as a distributed energy storage system that, if connected with the electric grid, can provide many services for the power system. Hence, considering a promising future for EV and that the connection with the grid will be essential, studies concerning the interconnection between the electric network and the vehicles have been proved necessary.

Therefore, the main objective of this thesis consists of developing a control technique for a Bidirectional DC-DC Converter (BDC), which is part of a bidirectional interface, that is responsible for connecting an EV battery with the grid. The bidirectional interface works with two operating modes, the Vehicle-to-Grid (V2G) mode - which can provide ancillary services for the utility grid, as the power supply - and the Grid-to-Vehicle (G2V) mode - which the main target is the battery charging process.

The system has been validated not only by computational simulations, with Mathlab and Simulink softwares, but also experimentally, by using a realtime interface from dSPACE. The latter is in charge of interconnecting the power structure and the control algorithm developed on the Simulink environment. The experimental validation of the system was succesfully achieved.

Keywords: Bidirectional DC-DC Converter, Electric Vehicle, Vehicle-to-Grid, Grid-to-Vehicle

Resumo

Devido às crescentes preocupações com a poluição do ar que contribui para o crescimento do aquecimento global, a disseminação dos veículos elétricos tem vindo a crescer por todo o mundo, por não emitirem gases poluentes, e sendo assim considerados como meios de transportes limpos.

Com a projeção de crescimento destes veículos para os próximos anos, e graças à grande quantidade de unidades já em circulação, várias pesquisas estudam a utilização destes meios de transporte como unidades distribuídas de armazenamento de energia e que, quando ligados à rede elétrica podem fornecer vários serviços. Considerando então que o futuro é promissor para os veículos elétricos e que a integração dos mesmos com a rede será essencial, pesquisas quanto à interligação entre ambos tem-se mostrado necessárias.

Com isso, o principal objetivo desta tese consiste em desenvolver uma técnica de controle para um conversor DC-DC bidirecional, que faz parte de uma interface bidirecional cujo o intuito é fazer a interligação entre a bateria de um veículo elétrico e a rede elétrica. O sistema conta com dois modos de funcionamento, o modo veículo para rede - (V2G) - que pode fornecer serviços auxiliares para a rede elétrica, como o fornecimento de potência, e o modo rede para o veículo - (G2V), cujo objetivo principal consiste no carregamento da bateria do veículo elétrico.

A validação do sistema foi realizada computacionalmente com o auxílio dos programas MATLAB e Simulink e, em seguida, o sistema foi validado experimentalmente utilizando uma carta de controle em tempo real da dSPACE. Esta carta de controle é responsável por fazer a interligação entre a estrutura de potência e o controle desenvolvido em Simulink. A validação experimental do sistema foi realizada com sucesso.

Palavras-chave: conversor DC-DC bidirecional, Veículo Elétrico, Ligação Veículo-Rede

Contents

List of Tables

List of Figures

Acronyms

BADC Bidirectional AC-DC Converter. 6, 31–34, 37, 38, 79, 80, 84

BDC Bidirectional DC-DC Converter. vii, 6–8, 11, 12, 14, 17, 26, 31–35, 39–41, 46, 70, 74, 79, 81, 84, 85

BEV Battery Electric Vehicle. 5

DAB Dual Active Bridge. 12

DSP Digital Signal Processor. 85

ECU Electronic Control Unit. 45

EV Electric Vehicle. vii, 1, 3–6, 8, 27, 29, 32, 85

EVI Electric Vehicles Initiative. 4, 5

G2V Grid-to-Vehicle. vii, 7, 14, 33, 34, 36, 37, 40, 41, 54, 61, 62, 64, 67, 68, 70, 74, 76, 79, 82–85

ICV Internal Combustion Vehicle. 1, 4

IEA International Energy Agency. 1

IGBT Insulated-Gate Bipolar Transistor. 32, 35, 39, 40, 49, 86

PHEV Plug-in Hybrid Electric Vehicle. 5

PI Proportional-Integral. 14, 15, 34–36, 40, 51, 67, 68, 70, 74, 80, 81, 83, 84

PID Proportional-Integral-Derivative. 8, 22–26

PWM Pulse-Width Modulation. 14, 35, 36, 39, 40, 49

RTI Real-Time Interface. 7, 50

SOC State-of-Charge. 15, 28, 52, 54, 57, 59, 62, 64, 72, 79, 80, 86

UPS Uninterruptible Power Supply. 27, 29

V2G Vehicle-to-Grid. vii, 7, 14, 33–37, 40, 41, 51, 52, 61–63, 67, 68, 70, 72, 74, 79–83

VRLA Valve Regulated Lead-Acid. 17, 28, 29, 32

Chapter 1

Introduction

Although it seems that the EV technology is something recent, those vehicles date all the way back to 1837, right after the development of the primary batteries and the electric motor. According to [1], EV are older than the internal combustion engine. Despite that, with the invention of the electric starter motor, EV started losing space for the conventional gasoline-powered cars, due to lower cost and longer ranges of the Internal Combustion Vehicle (ICV), compared to higher cost of both electric-powered cars, as a result of high cost of the batteries, as explained in [1].

Even with this fall on the vehicles market, due to the recent concerns about the increase of global warming, EV became popular again as an alternative for reducing air pollution, since those vehicles are emission-free.

1.1 Electric vehicles around the world and the market projection

Concerning the improvement on air quality, the Norway Minister of Transport, Jon Georg Dale, declared this year (2019) that Norway sees the rise of EV as one of the most important measures to reduce climate emissions [2]. In addition, one of the biggest cities in the world, Paris, unveiled plans to eliminate ICV by 2030 and becomes carbon neutral by 2050 [3]. Even more audacious, in 2017 the Transport Minister of India announced that he intends to replace, in the whole country, from ICV to electric-powered vehicles until 2030, while France and the United Kingdom hope to complete the same task only on 2040 [4].

According to the International Energy Agency (IEA) [5] [6], the electric car fleet

around the world exceeded 5.1 million in the last year, where China remained as the world's largest electric car market in 2018, with almost 1.1 million cars sold and a fleet of 2.3 million units, while Europe got the second place with a fleet of 1.2 million electric cars (and a total of sales around 385,000 in the last year) and the United States came on third with 1.1 million units (around 361,000 sales in 2018). Beyond that, figure 1.1 brings the electric car sales for some countries and the respective electric car share in the market from 2013 to 2018. It is evident that Norway leads the subject among the electric car market share (with almost 50% of cars sold being electric-powered, in 2018), followed by Iceland in second (although not illustrated in figure 1.1), and by Sweden in third [5].

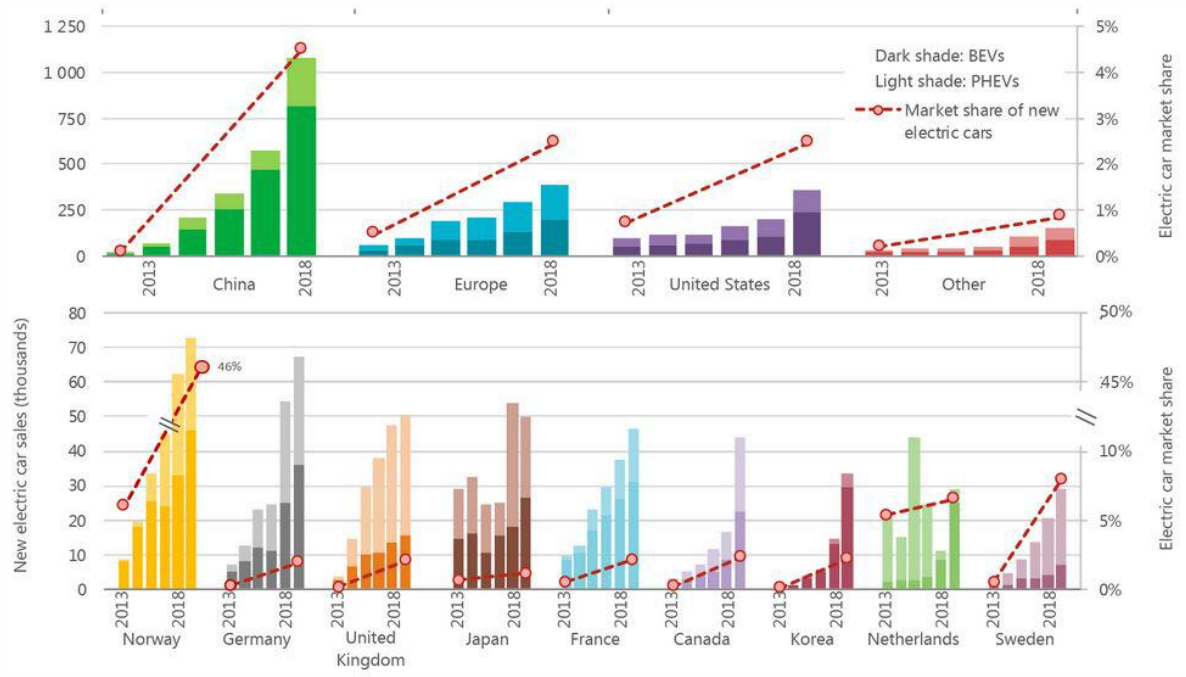

Figure 1.1: Electric cars sales and market share (Taken from IEA [5])

However, not only the electric car sales and fleet increased on the recent years, but also electric two/three-wheelers, exceeding 300 million units on the road worldwide (which China also leads the total number of units), where over 25% of the two-wheeler fleet around the globe is electric-powered. Besides that, the electric buses fleet increased too in 2018 (despite of the number of sales decreased around 12% when

compared to 2017), where more than 460,000 units were on the road (more than 100,000 units when compared to 2017) [5] [6].

The perspective for the electric cars' market is exciting, since it is expected to increase even more. As figure 1.2 shows, the projection of the electric powered car sales for the next two decades, could overcome gasoline-powered cars worldwide [7].

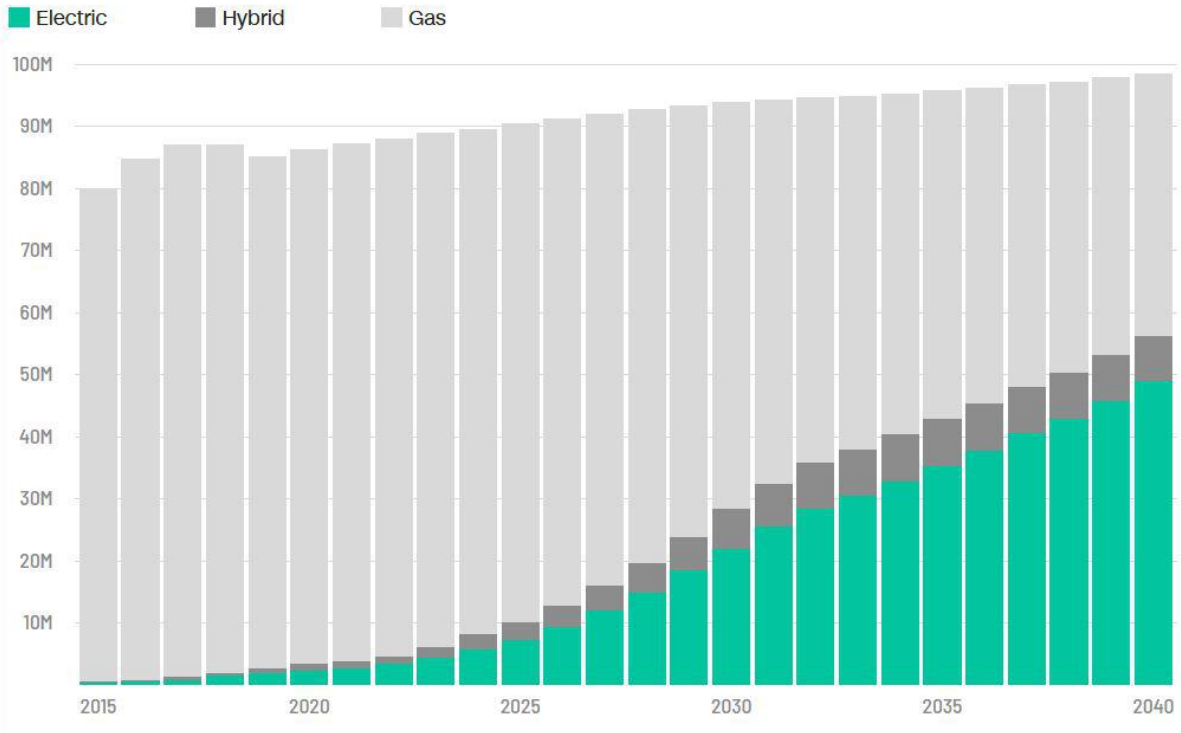

Figure 1.2: Projection of electric cars sales for the next two decades (Taken from CNN [7])

1.2 Incentives for the popularization of EV

The increase of the EV fleet worldwide has many reasons, as the Center Energy Regulator of Canada [8] shows for example:

- Subsides and incentives from the government:
  - The governments of Quebec and Ontario offer discounts over C$8,000 and between C$3,000 and C$14,000, respectively, for each sold electric vehicle;

    - Privileged parking lots in strategical locations for EV.

- Fuel price:

    - Due the higher efficiency of EV when compared to ICV, and taking into consideration regions where the price of electricity is low, the fuel price is a determinant factor.

The Germany government will give a special tax depreciation allowance of 50% in the year of purchase for delivering fully EV between 2020 and 2030. Another incentive is that charging an EV on an employer's premises is tax exempt until 2030 [9].

Norway became the country with the biggest market share for electric cars due the incentives that started in the 1990s, with the removal of the vehicles purchase tax for all the electric cars. Besides that, in 1997 drivers of EV did not have to pay on toll roads and in 1999 the free municipal parking was introduced. Also, as the Minister of Transport of Norway reported in [2], the infrastructure for charging EV is extremely important for encouraging the development and the increase of this technology. Moreover, Norway owns more than 11000 publicly charging points nowadays.

Another important factor of incentive for the increase of electric-powered vehicles fleet is the battery cost. According to [6] the average lithium battery price fell 18% on 2018 when compared with 2017. Aditionally, the battery production expectes to grow almost thirty times until 2030, significant cost reductions can be expected [6].

Besides the governments incentives for the expansion of EV, there are several programmes created by initiatives and organizations in order to reach that goal. For example, the Electric Vehicles Initiative (EVI), which on its own words is a: "multi-government policy forum created to accelerate the introduction and adoption of EV worlwide" which contains 16 countries, like the three other countries aforementioned (Canada, Germany and Norway), besides the United States, United Kingdom, Portugal, Sweden, and others [10].

One of the EVI programmes is the EV30@30, which aims to accelerate the deployment of EV with a target of 30% new electric sales by 2030. It supports the market for electric cars, buses, trucks. It also works on the infrastructure for delivering energy for the new deployed vehicles [10].

Another program from EVI is the Global EV pilot city, which aims to develop a global platform for supporting the communication among the leading global cities that are interested in increasing the electric mobility into their jurisdictions [10].

1.3 Interaction of EV with the grid

The interaction of EVs - Battery Electric Vehicles (BEVs) and Plug-in Hybrid Electric Vehicles (PHEVs) - with the grid is not limited to only charge the vehicle's battery. Besides that, as proposed by Kempton and Letendre [11] back in 1996, EVs can be used as power sources for electric utilities. As studies revealed that most of the vehicles are parked 95% of the time, they can remain connected to the grid and deliver the energy back when needed [11].

The EV charging and the active regulation are examples of interaction of EVs with the electric grid, where they act as loads. The active regulation is used for maintaining the grid's frequency at the specified value (50 Hz or 60 Hz) [12] [13]. The charging process has different levels according to the power capability and the charging duration. Those levels can be seen in table 1.1, where AC Level 1 is typically presented in residences, AC Level 2 is for public and commercial areas, like workplace, movie theaters and shopping malls. Finally, the DC fast charging (which comprises DC Level 1 to DC Level 3) is for public, private or commercial charging stations [14].

However, as mentioned by Mwasilu, Justo, Kim, *et al.* [14], the EV charging process is an additional burden for the grid, and if not appropriately controlled, it can bring drawbacks for the system, as the further aging of the equipments of the power system, the overload of the grid and an increased power demand which leads to a less efficient electricity supply. Alternatives for circumvent this situation are the coordinated

Power Level Type	Voltage Level (V)	Current Capacity (A)	Power Capacity (kW)	Charging Time
AC Level 1	120 VAC	12 16	1,4 1,9	PHEV: 7 h EV: 17 h
AC Level 2	240 VAC	Up to 80	19,2	PHEV: 3 h / 3,3 kW charger 1,5 h / 7 kW charger EV: 7h / 3,3 kW charger 3,5 h / 7 kW charger
AC Level 3	-	-	>20	Under development
DC Level 1	200-500 VDC	<80	Up to 40	20 kW charger PHEV: 22 min EV: 1,2 h
DC Level 2	200-500 VDC	<200	Up to 100	45 kW charger PHEV: 10 min EV: 20 min
DC Level 3	200-600 VDC	<400	Up to 240	Under development

Table 1.1: Charging levels characteristics according to the Society of Automotive Engineers J1772 standard (Extracted from [14])

charging (or smart charging), which consists on charging EVs at moments of low demand [12], minimizing the charging costs on the electricity market and finding other intelligent ways to avoid undesirable impacts on the electric grid [14].

A few examples of ancillary services that EVs can provide to the grid acting as a power supplier are demonstrated in Ehsani, Falahi and Lotfifard [12]. They are the peak shaving (which consists on injecting power into the grid for helping during peak demands of the power system), the spinning reserve (where the EVs act as a power supply which is already connected to the grid and it can rapidly increase their power output to supply the changes on the demand) and the injection of reactive power into the grid for reactive power regulation services, for motor starting services and for grid fault services on networks supplied by renewable energy sources [12].

1.4 Objectives

This thesis intends to develop a method of controlling a BDC, which in combination with a single-phase Bidirectional AC-DC Converter (BADC) compose a bidirectional interface, for connecting an EV with the grid.

The BDC control consists of two different methods, according to the power flow direction. If the power flow goes from V2G, the vehicle provides energy, therefore, it discharges. If the power flow goes on the opposite way (G2V), the battery of the electric vehicle stores energy, hence, it charges.

The development of this project includes the simulation and the validation of the controlling system for the proposed power structure, with the software MATLAB and Simulink. Also, it includes the validation on an experimental platform, with a Real-Time Interface (RTI) and Real-Time controller board from dSPACE.

For achieving the final objective (experimental validation), the target was:

- Observe the injection of current (power) into the grid, keeping a constant current;
- Observe the injection of current (power) into the battery pack and observe the battery voltage behaviour, during all the steps of the charging mode, ensuring the correct operation of each step of this mode, as:
  - Keep a constant current to charge the batteries in the first step;
  - Keep a constant voltage to charge the batteries in the second step;
  - Keep a constant voltage to charge the batteries, but restricting the charging current in a maximum of 600 mA in the third step;
- Observe and control the transition between the two operation modes, ensuring a smooth transition between them;

1.5 Document Structure

This thesis is divided into eight chapters, for describing the work applied during the development of this project.

- Chapter 1: Introduction

  - Gives a contextualization about the importance of EV at present and how they can be used not only as an energy storage element, but also as an energy source.

- Chapter 2: State of Art

  - Brings a literature review about the existing topologies of BDC, their control methods, and a brief review about some charge/discharge algorithms for batteries.

- Chapter 3: Theoretical Background

  - Brings a concise explanation about the theoretical concepts applied for the development of this thesis, such as batteries, the operation of the buck converter and the boost converter and about the Proportional-Integral-Derivative (PID) controller.

- Chapter 4: Power Structure and its operation

  - Shows the power structure used for the validation of this project, on the simulation software and on the real workplace with its components. Also, it explains the operation modes of the power structure and the control logic applied in the BDC.

- Chapter 5: Simulation validation

  - Presents the results obtained via simulation from the tests suggested.

- Chapter 6: Experimental validation

  - Presents the results obtained experimentally from the tests suggested.

- Chapter 7: Data analysis and discussion

  - Brings the analysis of the data obtained on the simulation and on the experimental tests.

- Chapter 8: Conclusion

  - Gives the final conclusions of the thesis and brings suggestions for future works related to this project.

Chapter 2

Topologies of Bidirectional DC-DC Converters and Control of Batteries Charge/Discharge

This chapter presents the current state of art of BDCs, introducing a brief explanation about the different topologies, in section 2.1. Section 2.2 lists and compares the used algorithms for the converters, and for controlling of battery: charge and discharge. Section 2.3 gives a brief introduction of some charging and discharging algorithms concerning the batteries features.

2.1 Bidirectional DC-DC Converters

According to Sharma and Sharma [15], the BDC can be categorized into:

- Isolated topologies;
- Non-isolated topologies;
- Resonant topologies.

2.1.1 Isolated topologies

Sharma and Sharma [15] describes that, in general, among the isolated converters, the most commonly used one is the Dual Active Bridge (DAB), whether with the voltage-fed, or the current-fed.

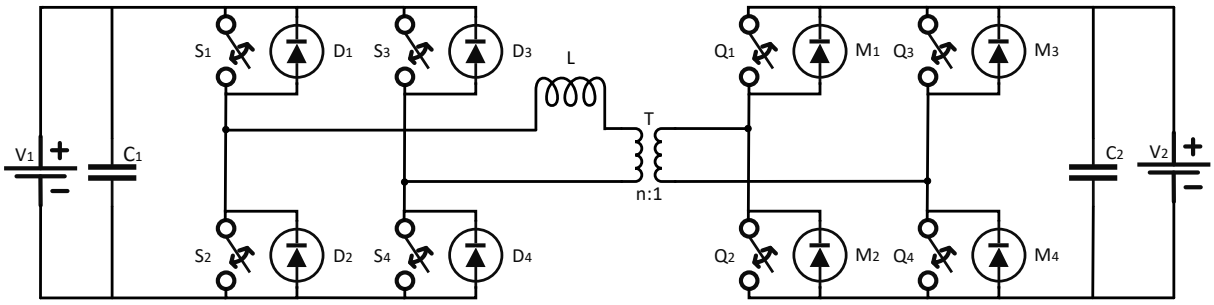

Figure 2.1: DAB converter proposed in [16]

A voltage-fed Dual Active Bridge (DAB) is proposed by [16], which comprises two full bridges with four switches each, and a high frequency transformer used to isolate the bridges, as showed in figure 2.1. Some of the advantages of those converters comprises the galvanic isolation, the control flexibility, the symmetric structure as presented in figure 2.1 and the low voltage stress. On the other hand, the disadvantages of the voltage-fed are the little range for the voltage conversion [17], the insertion of reactive power into the system [18], besides the high current which circulates through the components of the converter [19].

The advantages for the current-fed DAB consists of high voltage gain (on the contrary of the voltage-fed) [20], low input current [21], no duty cycle loss and low turns ratio for the transformers, while the disadvantage presented comprise the addition of components on the circuit (as the snubbers capacitors for absorbing the voltage surges) [15].

2.1.2 Non-Isolated topologies

According to Sharma and Sharma [15], the most used BDC consists in a non-isolated which uses buck-boost topology, comprising only two switches to perform the DC voltage conversion. Such topology was experimented by Leite, Ferreira and Batista [22], Pinto, Monteiro, Gonçalves, *et al.* [23], Sgarbossa, Turri, Putrus and Lacey [24], and by Thomas and Chacko [25].

Another buck-boost converter is proposed and validated by [26], which consists of

two switches which operate either on the boost mode either on the buck mode, cascaded with another two switches which operate on the previously mentioned modes as well. There is an intermediate staged which consists of a capacitor between the cascaded buck-boost converter, responsible for storing the energy and allowing an overlap between the battery voltage and the DC-bus voltage. Figure 2.2 shows the schematic of the cascaded buck-boost converter.

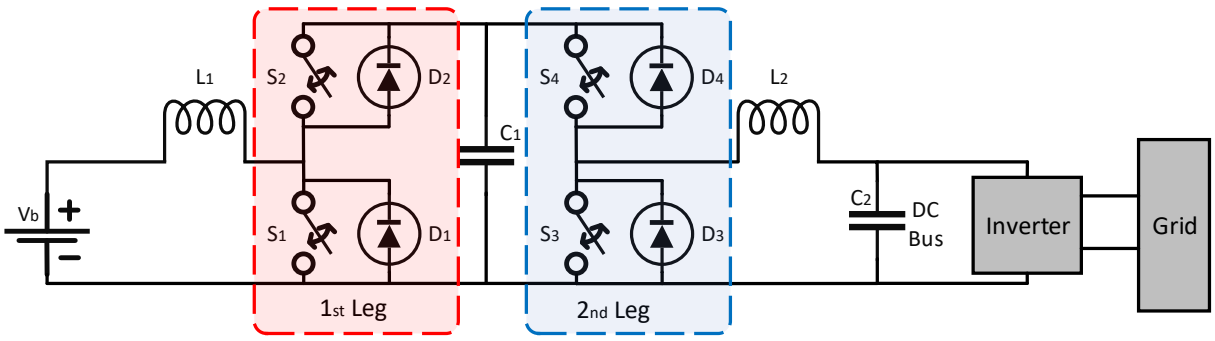

Figure 2.2: Cascaded Buck-Boost converter proposed in [26]

Compared to the isolated topology, the non-isolated one presents the benefits of fewer components, which leads to a lower cost [15], and high power-stage efficiency [18]. However, the drawbacks consists of the lack of safety standards when compared with the isolated topology, and the even smaller range for voltage conversion [15].

2.1.3 Resonant topologies

Usually, the resonant topology consists of isolated full-bridges with resonants circuitry, as showed in figure 2.3. Zahid, Dalala, Chen, *et al.* [18] lists some advantages and drawbacks of those converters, where the advantages are the high frequency operation, fewer components due the elimination of snubber circuits and low electromagnetic interference. The disadvantage is the surge caused in the start-up current due the capacitor of the output filter.

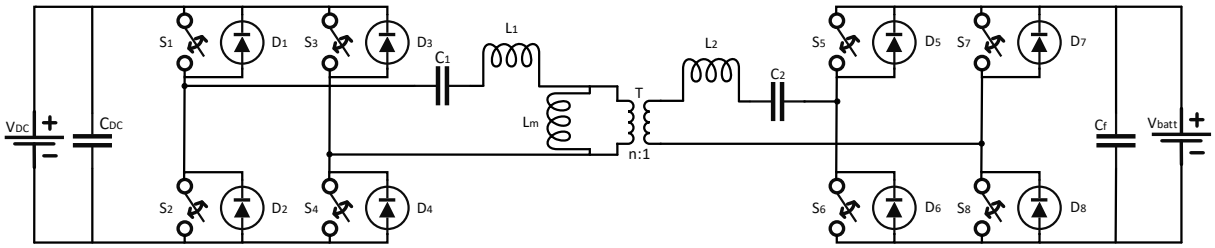

Figure 2.3: Resonant converter topology presented in [18]

A more detailed comparison between the BDC converters is presented in Sharma and Sharma [15] on pages 350 and 351, according to their topologies, number of devices, isolation, efficiency and other categories.

2.2 Charge and Discharge Control for the converters

Leite, Ferreira and Batista [22], Pinto, Monteiro, Gonçalves, *et al.* [23], and Thomas and Chacko [25] use the same discharge control for the BDC topology aforementioned in 2.1.2, and similar charge control, using Proportional-Integral (PI) controllers and Pulse-Width Modulation (PWM) technique.

The discharge (or V2G) control consists on delivering a constant current from the batteries. The value of the reference current is achieved dividing the power required from the battery by its voltage. The V2G control is experimentally validated in [22] and [23], while [25] only validates it computationally.

For the charge (or G2V) control [22] follows the charge curves defined by the battery manufacturer, while in [25], it uses a constant voltage charge. A two stage charging algorithm is used in [23], which consists firstly of a constant current charging, until the battery voltage reach its maximum recommended value, and after that, the battery is charged with a constant voltage until the current absorbed by it falls to a residual value. The G2V control is validated by Pinto, Monteiro, Gonçalves, *et al.* [23], while in Leite, Ferreira and Batista, and in Thomas and Chacko ([22], [25]), only the simulation results were achieved.

For Sgarbossa [24] the discharge control used is not clearly reported, while the

charge control consists of a PI controller which compares the set-point current added with the integral of the capacitor current with the measured current of the battery. The steady state of the system is reached only when the sum between the three signals aforementioned is null. An important point to emphasize is that in [24], the moment to stop the battery charge is not reported.

For the cascaded buck-boost converter of Khan, Husain and Sozer [26], on the discharge mode, the first leg of the converter from figure 2.2 acts as a boost converter and the second one, as a buck converter. On the charging mode, first leg acts as a buck converter, while the second one, as a boost converter. The capacitor between both legs is maintained at a voltage level set by the converter controller.

2.3 Charge and Discharge Algorithms for batteries

Many charge and discharge algorithms for batteries can be found on the literature. Linden and Reddy [1] demonstrate many different ways of charging and discharging secondary batteries (rechargeable batteries), taking in consideration its features (State-of-Charge (SOC), temperature, battery capacity, cells voltage). Taking the Lead-Acid batteries as example, [1] mentions over 10 different methods for charging those devices, as the constant current, constant potential, taper charge, pulse charging, trickle charging, float charging and rapid charging.

Inoa and Wang [27] propose a charging algorithm with a constant temperature followed by a temperature control. Xu, Gao, He, *et al.* [28] propose an algorithm for the SOC estimation of Lithium-ion batteries during the discharge mode. Eom, Shin, Kim, *et al.* [29] propose an algorithm which maintains the temperature of the battery between 25 °C and 35 °C during the constant current charging.

Chapter 3

Methodology Approached

This chapter presents a brief review about DC-DC converters, in section 3.1. It also gives a theoretical background used for developing the control of the BDC, in section 3.2. Section 3.3 brings an explanation about the concept of batteries, its main features and some aspects of the Valve Regulated Lead-Acid (VRLA) battery used in the development of this project.

3.1 DC-DC Converters

DC-DC converters consist on power electronic circuits that convert a dc voltage level into another dc voltage level, usually with a regulated output [30]. Bidirectional DC-DC converters consist of DC-DC circuits that are capable of inverting the direction of the power flow with the correct control command and maintaining the same voltage polarity on either sides of the converter [31].

In this section the boost and buck converters are explained in greater detail. These converters are used for extracting the amount of power from the batteries that will be injected into the grid, or injecting power from the grid into the batteries, respectively.

3.1.1 Boost Converter

The boost converter consists of a step-up voltage converter, in other words, it delivers a higher voltage in the output when compared to the voltage applied in the input. An schematic of the boost converter can be seen in figure 3.1. In general, S_1 is replaced by MOSFETs or IGBTs.

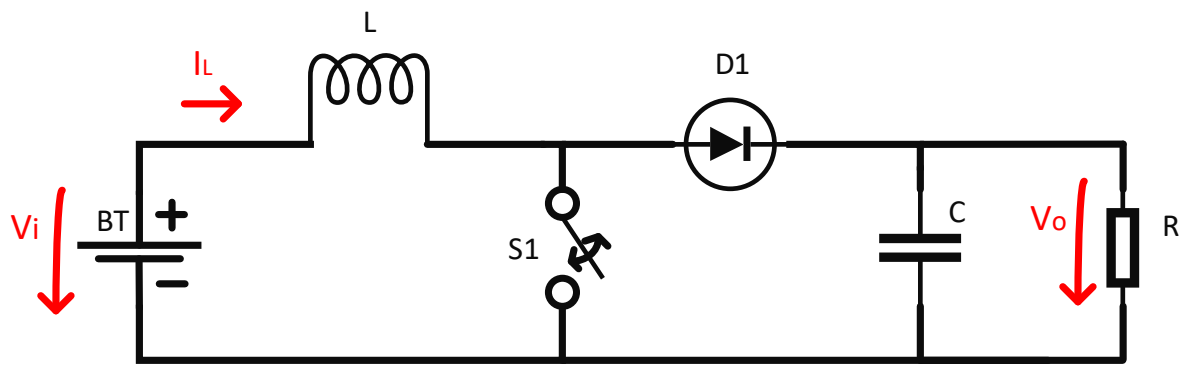

Figure 3.1: Boost converter

For achieving a higher voltage level in the output, the switch S_1 of the figure 3.1 must be turned on and off with a high frequency. When S_1 is on, the diode D_1 is reverse-biased and isolates the capacitor and the load from the rest of the circuit, as can be seen in figure 3.2. Therefore, the inductor L starts to charge until S_1 is turned off, then the current once stored in the inductor goes through the path indicated in figure 3.3, charging the capacitor C, which discharges on the load. A further explanation of the boost converter operation can be found in [30].

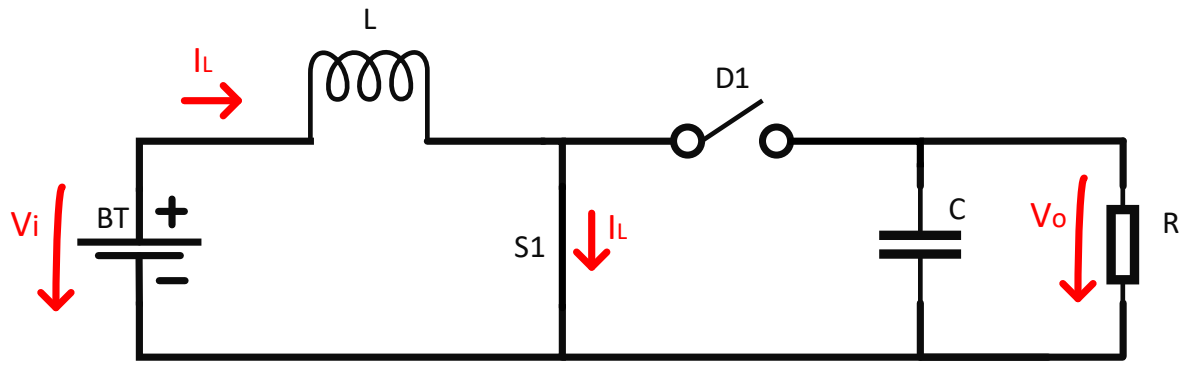

Figure 3.2: Boost converter equivalent with S_1 closed

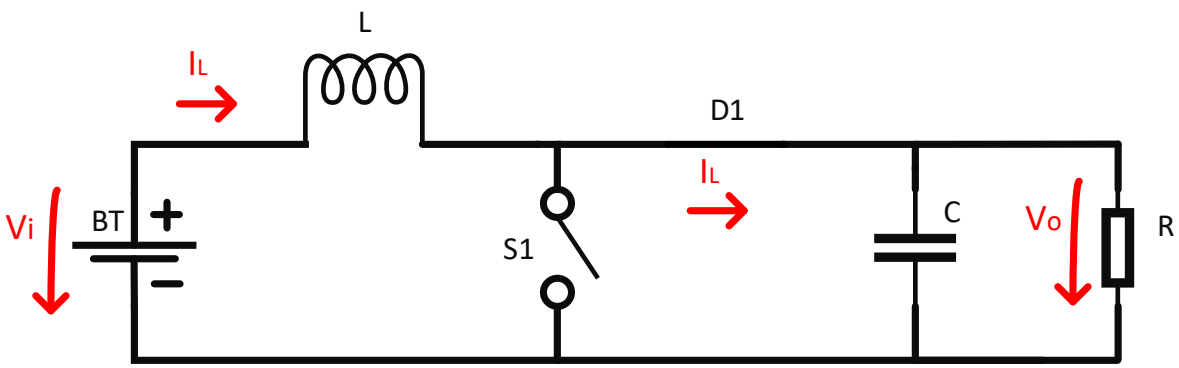

Figure 3.3: Boost converter equivalent with S_1 open

The relationship between the input voltage (V_i) and the output voltage (V_o) for the boost converter is given by,

$$V_o = \frac{V_i}{(1-D)}, \tag{3.1}$$

where D is the duty-cycle of switch S_1, which represents the ratio between time that S_1 is on during the period T (period of the signal applied to S_1 for controlling the switch), as showed in

$$D = \frac{t_{on}}{T} = t_{on} f = \frac{t_{on}}{(t_{on} + t_{off})}. \tag{3.2}$$

An important feature of the boost converter is the project of the inductor and capacitor size, responsible for determining the inductor current ripple and the output voltage ripple, respectively.

The minimum value attributed for inductor L for a boost converter designed for a continuous current operation [30] is described as,

$$L_{min} = \frac{D(1-D)^2 R}{2f} \tag{3.3}$$

where f is the frequency of the signal applied to S_1 and R is represented by

$$R = \frac{V_o^2}{P}. \tag{3.4}$$

Another way to express the inductor size is,

$$L = \frac{V_i D}{\Delta i_L f}, \tag{3.5}$$

which expresses the inductor size according to a desired Δi_L.

3.1.2 Buck Converter

The buck converter consists of a step-down voltage converter, in other words, it delivers a lower voltage in the output when compared to the voltage applied in the input. An schematic of the buck converter can be seen in figure 3.4. In general, as in the boost converter, S_1 is replaced by MOSFETs or IGBTs.

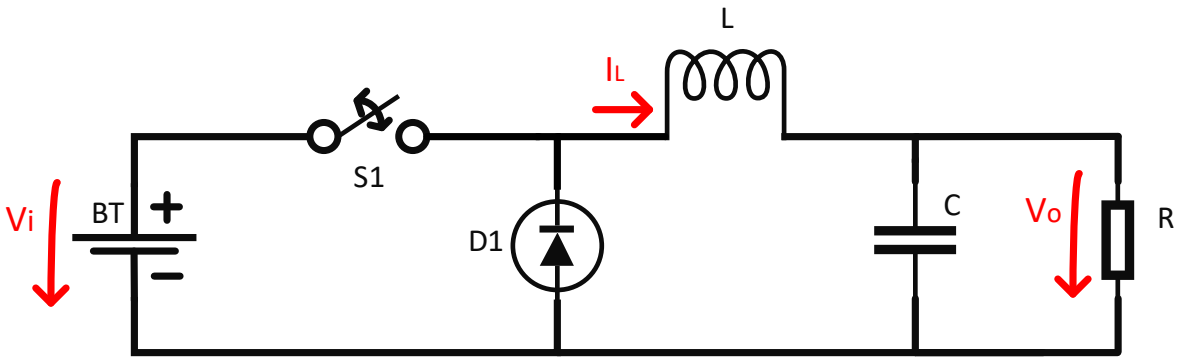

Figure 3.4: Buck converter

For achieving a lower voltage level in the output, the switch S_1 of the diagram above must be turned on and off with a high frequency. When S_1 is on, the diode D_1 is reverse-biased and the current provided by the batteries goes through the inductor, as indicated in figure 3.5. Therefore, the inductor L starts to charge until S_1 is turned off, when the current once stored in the inductor goes through the path indicated in figure 3.6. A further explanation of the buck converter operation can also be found in [30].

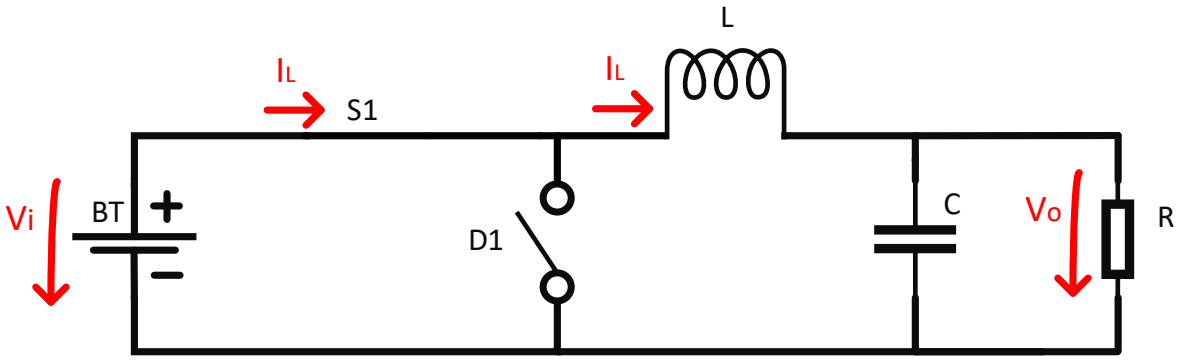

Figure 3.5: Buck converter equivalent with S_1 closed

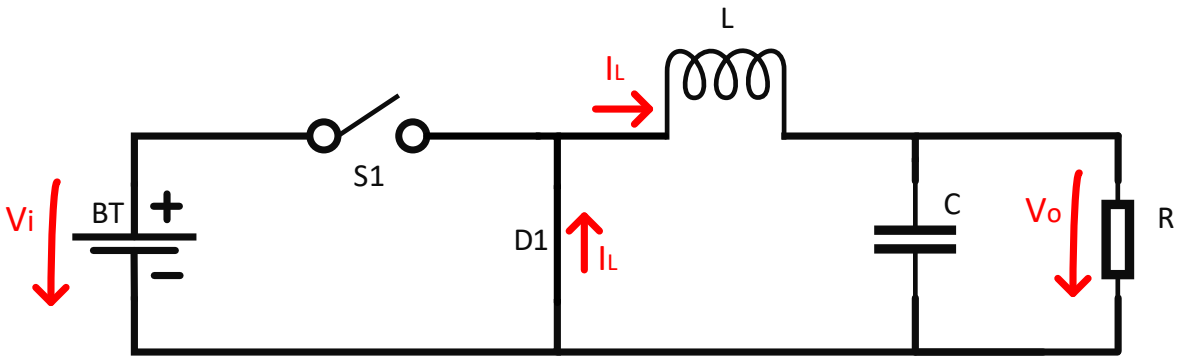

Figure 3.6: Buck converter equivalent with S_1 open

The relationship between the input voltage (V_i) and the output voltage (V_o) for the buck converter is given by

$$V_o = V_i D, \tag{3.6}$$

where D is the duty-cycle of switch S_1, as explained in subsection 3.1.1 and shown in equation 3.2.

As in the boost converter, an important feature of the buck converter is the project of the inductor and capacitor size, responsible for determining the inductor current ripple and the output voltage ripple, respectively.

The minimum value attributed for inductor L for a buck converter designed for a continuous current operation [30] is

$$L_{min} = \frac{(1-D)R}{2f}, \tag{3.7}$$

where *f* is the frequency of the signal applied to S_1 and *R* is represented in equation 3.4.

Another way to express the inductor size is

$$L = \frac{V_o(1-D)}{\Delta i_L f}, \tag{3.8}$$

which expresses the inductor size according to a desired Δi_L.

3.2 Proportional-Integral-Derivative Control

The PID control consists of a control method that offers the simplest and the most efficient solution to considerable real world control problems for general applicability [32] [33]. The controller is named after its three components, the proportional, integral and derivative. Each component acts on its own way to eliminate the error between the measured value and the reference/desired value. Although in many situations the PID control does not provide an optimal control, it is applied for most control systems (actually the big majority of industrial controllers are based around PID algorithms [33]), specially for those where the mathematical model of the plant is unknown and analytic design methods cannot be applied [32].

Although it can be used in series, as explained in [33], generally the PID controller has a parallel structure, as in figure 3.7, where *Kp* is the proportional gain, *Ki* is the integral gain, *Kd* is the derivative gain, *e(t)* is the error between the desired value and the output and *u(t)* is the PID controller output.

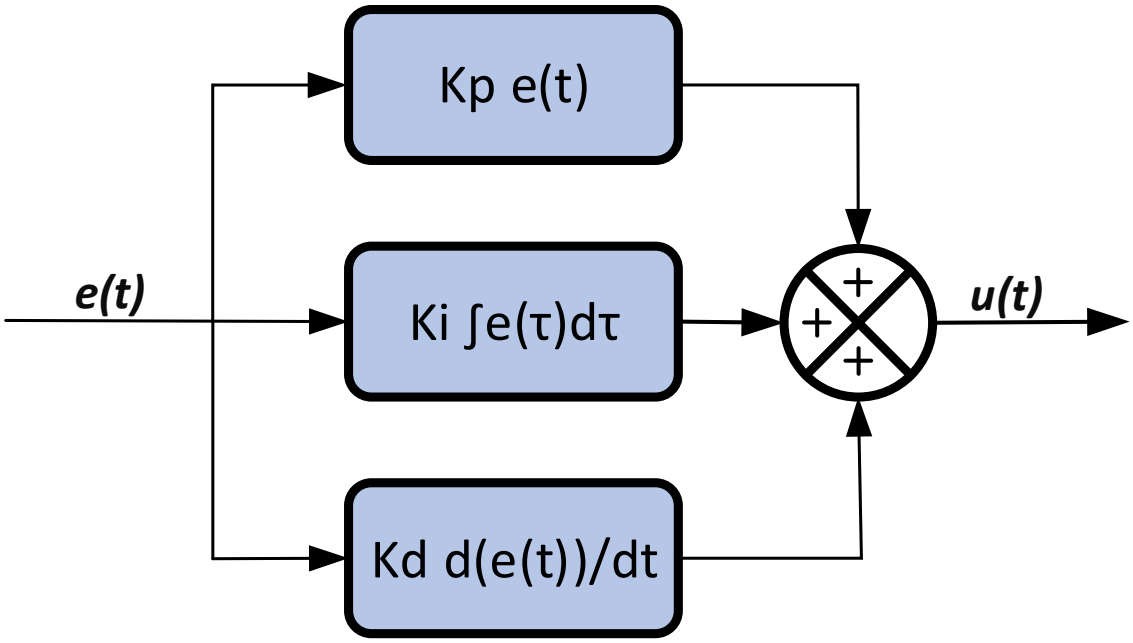

Figure 3.7: Structure of a PID controller

Usually, the controller is applied in series with the plant that must be controlled, as in figure 3.8, where *r(t)* represents the reference value, or the desired value, *e(t)* represents the error between the desired value and the output, and *y(t)* the measured value, or output.

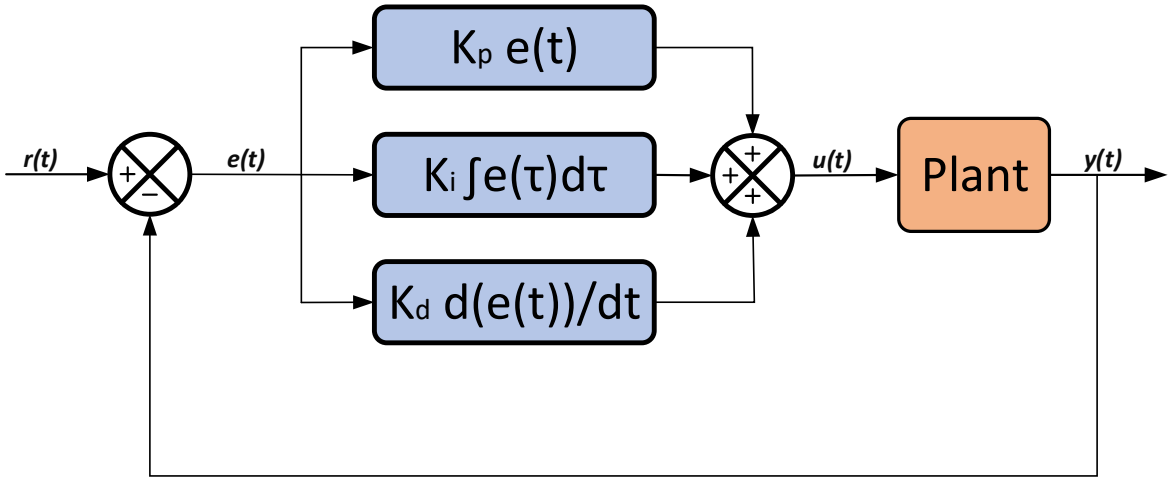

Figure 3.8: PID controller in series with a plant

The PID components act on the error reducing the distance between the set-point

(desired value) and the measured value. The output of the controller (*u(t)*) is the output of each component summed, and is the control signal that acts on the plant. The feedback displayed in figure 3.8 usually is a system variable that is compared to the set-point and generates the error signal.

The proportional component basically multiplies the error signal by a constant, generating an output that is proportional to the error signal (as the name suggests). It determines how fast the response of the controller will be. The proportional component cannot eliminate the error between the set-point and the output by itself, for that, the integral component must be used.

The integral component gives an output which is proportional to the integral of the error over time. It is responsible for eliminating the steady-state error, although it increases the system overshoot and degrades the system stability [33]. The integral component of the controller can present a problem if the controller has a range limit, it saturates and starts to diverge from the set-point due the accumulated error, which can lead to instability, until the saturation is offset [33]. A solution for that problem is presented in [33] and is called anti-windup, which consists basically on a reset function for the integrator, removing its accumulated error.

The derivative term gives an output which is proportional to the rate change of the error. Hence, the bigger the rate change, bigger is the output of the derivative controller, which means that will alter the output aggressively. For high frequency signals the derivative component is useless, due the harsh variation of those signals. However, this controller is useful for preventing overshoot, once it improves the transient response [33].

The mathematical model of the PID controller in continuous time is represented by

$$u(t) = K_p e(t) + \int_0^t K_i e(\tau) d\tau + K_d, \frac{de(t)}{dt} \tag{3.9}$$

where,

– *u(t)* - PID controller output;

– K_p - Proportional gain;

– K_i - Integral gain;

– K_d - Derivative gain;

– *e(t)* - Error between the reference value and the measured value which is the input of the PID controller;

– *t* - Instantaneous time;

– τ - Integration variable.

For using the PID logic control into microcontrollers, equation 3.9 must be converted from the continuous time domain to the discrete time domain, and it can be done by many ways.

For achieving the discrete time domain, firstly the Laplace transform of equation 3.9 must be taken, and then, using the bilinear transform, the PID mathematical model goes for the discrete time, but on the Z domain, to get the final equation in the discrete time domain, the inverse Z-transform must be taken [34].

The mathematical model for the PID controller is

$$u[n] = (K_p - \frac{K_i T_s}{2} - \frac{2K_d}{T_s})e[n] + (\frac{2K_d}{T_s} - K_i T_s)e[n-1] - (K_p + \frac{KiT_s}{2} + \frac{2K_d}{T_s})e[n-2] + u[n-2], \tag{3.10}$$

where,

– *u[n]* - PID controller output;

– *u[n-2]* - PID controller output delayed by two samples;

– K_p - Proportional gain;

– K_i - Integral gain;

– K_d - Derivative gain;

– *e[n]* - Actual error between the reference value and the measured value which is the input of the PID controller;

– *e[n-1]* - One sample delayed error between the reference value and the measured value which is the input of the PID controller;

– *e[n-2]* - Two samples delayed error between the reference value and the measured value which is the input of the PID controller;

– T_s - Sample period.

More information about the transformation process from the continuous time domain for the discrete time domain can be found in Discrete-Time Signal Processing [34].

The PID controllers integrated with the BDC are presented in chapter 4, where they are used for controlling the dynamic of the operation modes of the system (discharging mode, charging mode).

3.3 Batteries

Batteries are devices which supply electric energy generated from chemical energy stored inside of them, achieving this process through electrochemical reactions. For rechargeable batteries, the reversal process is done, which electric energy is converted into chemical energy [1].

The battery's components are known as cells, which are the basic electrochemical units and are connected either in series, or parallel, or both, inside of the batteries, depending on the desired output voltage and the battery capacity, as explained in [1].

Batteries can be classified into four main categories:

– Primary batteries;

– Secondary batteries;

– Reserve batteries;

– Fuel-Cells.

Primary batteries consist of batteries that are not capable of being effectively recharged, therefore, the most of them are used once and then are discarded. Those batteries can be found on applications such as electronic devices (calculators, remote control), toys, watches, memory backup, lighting, and many others.

Secondary batteries are known as rechargeable batteries, which after a discharge, allows that the energy available can be restored to its original condition by injecting a charging current into them. Those components are widely spread around the world and can be found in numerous applications, as on electronic devices (cellphones, laptops, *etc.*), Uninterruptible Power Supplys (UPSs), EVs, and many others.

Reserve batteries consist of batteries that do not self-discharge over time, and are capable of delivering a high power when activated. They can be found on missiles, torpedoes, radiosondes, and other weapon systems.

Fuel-Cells converts chemical energy directly into electric energy and are not subject to Carnot cycle limitations of heat engines. A famous application of Fuel-Cells is its use on space vehicles through hydrogen/oxygen fuel-cell.

All information concerning about batteries classification and its applications were extracted from Linden's Handbook of batteries, of David Linden and Thomas Reddy [1].

3.3.1 Main Features

The two main features of the batteries are the provided output voltage, and the battery capacity. The output voltage information is essential to determine which battery will be used for a determined objective, depending on the voltage level required for that

application. The battery capacity consists of the amount of time that a battery can supply a determined power for a certain application. The current provided for a battery, based on its capacity, where

- I - Discharging/Charging current (A);
- C - Rated capacity of the battery (Ah);
- n - Time which the rated capacity is declared (h);
- M - Multiple of C.

$$I = M \times C_n. \tag{3.11}$$

Equation 3.11 shows the amount of current that a battery can supply for a determined amount of time. It is known on literature as the *C Rate* [1].

For example, considering a battery with a rated capacity of 20 Ah at the 20 h rate, and considering a $1C_{20}$ discharge rate, the battery will provide a 20 A current during 1 h for this application. Considering now a $0,1C_{20}$ discharge rate, the same battery will provide a 2 A current during 10 hours for this application. For the total amount of power that the battery can supply, it's only multiply the output voltage of the battery by its provided current.

Another important feature of batteries is the SOC, which basically consists of the percentage of energy remaining in the battery. However, to obtain the battery SOC, many other variables must be inspected, as the battery self-discharge, its temperature, its voltage, the discharge rate and the charge rate [1]. As the battery discharges, the SOC decreases, and it increases when the battery is being charged.

3.3.2 VRLA Batteries

A VRLA battery is a secondary battery (rechargeable battery) that only differs from the conventional Lead-Acid batteries for its arrangement feature, on which the electrolyte

of the VRLA batteries is immobilized and that those batteries are closed with a pressure regulating valve [35]. Although the Lead-Acid batteries have a vast application (as in energy storage, emergency power, EV, telephone systems, power tools, communication devices), the VRLA batteries' major application consists of the standby power market, from low-power applications (as UPS for a computer, or feeding a fire alarm panel) to high-power (UPS for communication facilities) [1].

Effect of temperature and discharge rates

For VRLA batteries, the capacity is related with the temperature and the discharge rate, on which the capacity decreases if the temperature decreases and then the discharge rate increases. For higher temperatures, the discharge rate lasts longer, as explained and showed in [1].

Charging characteristics

Charging a battery consists of returning the energy supplied during the discharge, however, it is an inefficient process, and the battery must be recharged more than 100%. The amount of energy that must be provided for the battery charge depends on how deeply it was discharged, on its temperature, the method of charging and its time.

The most popular method for charging a VRLA battery is the constant voltage charging, although constant current charging, float charging, taper current charging and other methods related to those can also be implemented [1].

For the VRLA batteries used for the development of this project, the three methods used for recharging them were the constant current charging, constant voltage charging and the float charging.

Chapter 4

Power Topology and Control Methods

This chapter presents the implemented control algorithms and the power topology. It describes each used component, like the batteries, the BDC, the BADC, the output filter, and also, the control algorithms of the DC-DC and AC-DC converters. Moreover, this chapter describes the simulation model and the used experimental platform for the validation of this experiment.

4.1 Power Module

The schematic of the power structure is displayed in figure 4.1.

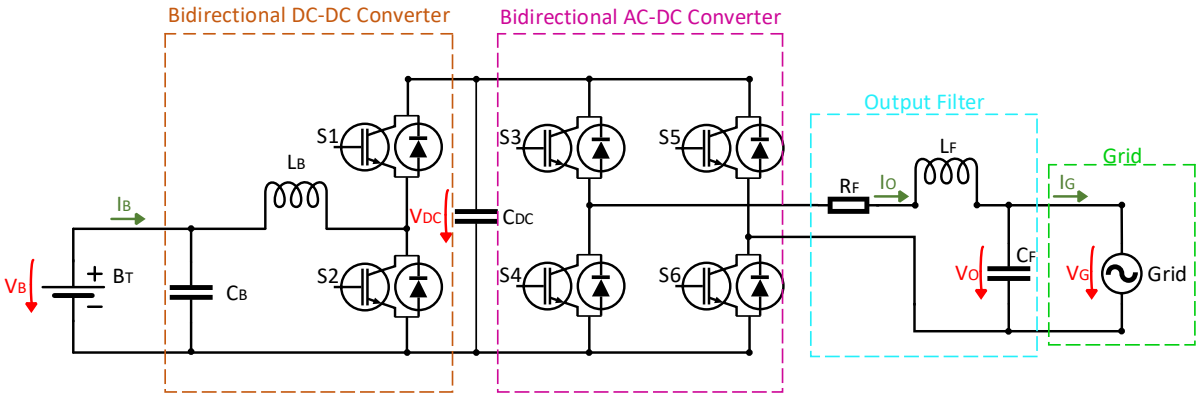

Figure 4.1: Power Structure

The power structure can be separated in five parts:

- Electric vehicle, replaced by 8 VRLA batteries (96 V);
- Bidirectional DC-DC converter (BDC);
- Bidirectional DC-AC converter (BADC);

– Output filter;

– Grid.

The following subsections describes each part of the power structure.

4.1.1 Battery (96 V)

The VRLA battery pack is used for emulating the EVs Battery. As mentioned in [36], there are three main types of batteries used for EVs, the Lead-Acid, Nickel-Metal Hydride and the Lithium-Ion. However, due the high cost of those two last mentioned batteries, it is non viable using any of those for this thesis purpose. Therefore, the VRLA batteries are used as an alternative for a cheaper system and due the fact of being available in the real workplace.

4.1.2 Bidirectional DC-DC Converter

The BDC links the batteries to the bidirectional AC-DC converter. The converter is represented in figure 4.1, inside the first box from left to right, by the first leg of the three-phase voltage source inverter, the switches S_1 and S_2, which are Insulated-Gate Bipolar Transistors (IGBTs) and the free-wheel diodes. It acts as a Boost converter when the power flow goes from the vehicle to the grid, and acts as a Buck converter when the power flow goes in the opposite way. The control algorithm of the BDC is explained in section 4.2.

The capacitor displayed between the BDC and the BADC is used to store the energy. It acts as a energy buffer between the DC-DC and the DC-AC converters. In the real workplace, the capacitor assumes a value of 1 mF, achieved by connecting two capacitors of 1 mF and 400 V rating in parallel, in series with another two capacitors of the same value in parallel. Thus, the resulting capacitance of the DC-link is 1 mF with a maximum rated voltage of 800 V, although the nominal voltage is around 400 V.

4.1.3 Bidirectional DC-AC converter

The bidirectional DC-AC converter links the capacitor of the DC-link to the grid. It is represented by the other four switches displayed in figure 4.1, S_3, S_4, S_5 and S_6. The BADC is responsible for converting the voltage and current waveform from direct current to alternate current, and contrariwise, depending if the system is injecting/extracting power into/from the grid. Also, the BADC is responsible for controlling the DC Link voltage. The control algorithm is also briefly explained in section 4.2.

4.1.4 Output Filter

The output filter used is a low-pass LC filter, designed for previous works associated with the power module, and its main purpose is to reduce the harmonics in the current that will be injected into the grid. The values designed for the filter were achieved by trial and error observing the current waveform, and after extensive simulation tests and experience from previous works.

4.1.5 Grid

The grid is the electric network, with 230 Vrms and 50 Hz, where the power will be injected when the system is working in the V2G mode, and from where the power will be extracted when the system is working in the G2V mode.

4.2 Control Algorithms

The power structure must be controlled separately, it means that there are two different control algorithms, one for the BDC and another one for the BADC.

The BDC control is responsible to decide between the two different modes of operation. If the power must be injected into the grid, the DC-DC converter assumes the V2G mode and acts as a step-up converter. If the battery must be charged, the converter assumes the G2V mode and acts as a step-down converter, as explained in [22].

The following subsection gives a detailed explanation of the control algorithm of the BDC.

The BADC control is complex and out of the scope of this project, but a concise explanation is given in section 4.2.2.

4.2.1 Control of the DC-DC Converter

The main objective of the BDC is to control the battery current in both modes (V2G and G2V). To accomplish that, PI controllers are used, as illustrated in figure 4.2, which displays the control diagram of the DC-DC converter. The derivative gain is not used in the controllers' application due the high frequency of the signals that must be controlled. In the following subsections a further explanation about the BDC control algorithm is given.

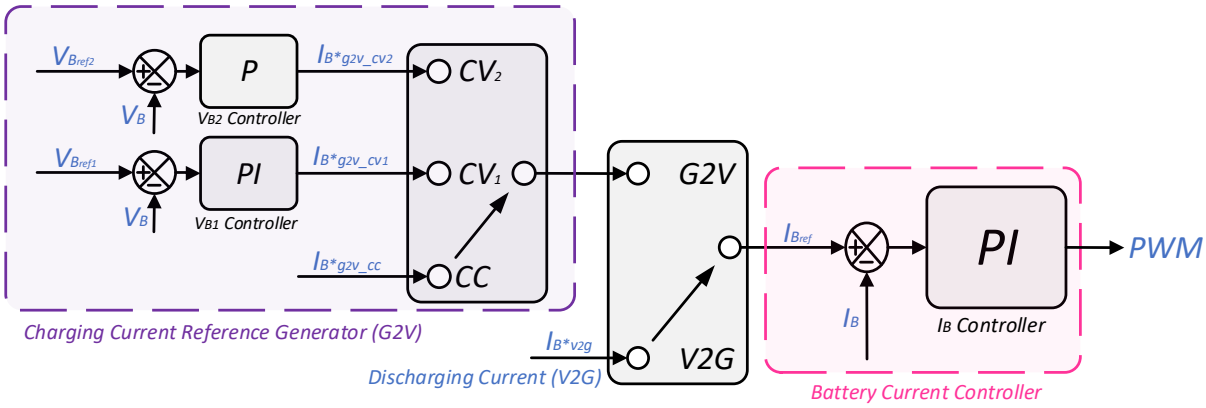

Figure 4.2: Bidirectional DC-DC converter control diagram

The measurements and set-points required for the BDC control are:

- Measurement:
  - I_B - Battery current;
  - V_B - Battery voltage;
- Set Point:

- $I_{B_{ref}}$ - Battery current reference;
- $I_{B*_{v2g}}$ - Discharging current reference;
- $I_{B*_{g2v\_cc}}$ - Charging current reference for constant current charging;
- $I_{B*_{g2v\_cv1}}$ - Charging current reference for constant voltage charging (generated by the first constant voltage controller);
- $I_{B*_{g2v\_cv2}}$ - Charging current reference for constant voltage charging (generated by the second constant voltage controller);
- $V_{B_{ref1}}$ - Reference voltage of the first constant voltage controller (used for the second stage of the charging mode);
- $V_{B_{ref2}}$ - Reference voltage of the second constant voltage controller (used for the third stage of the charging mode).

Discharging Mode

In the discharging mode, or V2G mode, the BDC works as a boost converter, therefore, switch S_2 is turned on and off in the switching frequency, while S_1 is always off. The control signal for S_2 is generated by a PI constant current controller, which the reference current is defined by the power desired to inject into the grid (P_B), divided by the battery voltage (V_B), as

$$I_{B*_{v2g}} = \frac{P_B}{V_B}. \tag{4.1}$$

The controller compares the reference current with the actual battery current and generates the signals that will be applied to a PWM with a 10 kHZ sawtooth wave to obtain the IGBTs gate pulse pattern.

On this project, the discharging current is adopted as positive, and consequently, the power supplied by the battery pack is considered positive, and the charging current is adopted as negative, therefore, the power absorbed by the batteries is considered negative.

Charging Mode

If in the discharging mode S_1 is always OFF, in charging mode it is always turned ON and OFF, while S_2 is always OFF. For the G2V mode, three steps are adopted to charge the batteries on this project:

– Constant current charging;

– Constant voltage charging;

– Float charging;

Firstly, the battery is charged with a constant current, therefore, the same PI constant current controller used in the V2G step is employed in this mode, as shown in figure 4.2. However, the reference current is negative and is defined by the battery manufacturer maximum charging current [37].

This step consists of charging the battery with a constant current until the battery voltage reach a pre-determined value. This procedure was suggested and validated by Pinto, Monteiro, Gonçalves, *et al.* [23].

Secondly, when the battery voltage reach the pre-determined value, the battery starts to charge with a constant voltage. To accomplish that, is used a PI controller that compares the reference battery voltage with the actual battery voltage, and the output of this controller is the reference current for the PI current controller. In this way, it generates the signals that will be applied to the PWM to obtain the pulses for S_1, as showed in figure 4.2.

This step consists of charging the battery with a constant voltage until the current consumed by the batteries falls to a pre-determined value. The current starts decreasing because the battery voltage gets closer to the reference voltage, and while the measured voltage increases, the battery pack needs less current to reach the set-point.

This procedure was also suggested by Pinto, Monteiro, Gonçalves, *et al.* [23], but instead of reaching a pre-determined value, the current consumed by the batteries decreases until reach a residual value and then finishing the charging process.

For a better comprehension of those two methods, a simple analogy can be made with a water tank (battery pack) which is filled with a constant flux of water (constant current) up to a certain height (pre-determined voltage). Hence, it starts to fill with a water flow controlled by a valve, in which this valve is responsible to fill the tank until it reaches the maximum height (the valve is the voltage controller, which generates the reference current for charging the batteries in the constant voltage charging mode). So, while the tank is filling and it gets closer to the maximum height, the water flow decreases (the valve is being closed) cause the water is almost reaching the set-point (the charging current decreases until it reaches a pre-determined value).

The last stage starts when the battery current declines to a pre-determined value too. Then, the battery is also charged with a constant voltage (as in the second stage, but with a different reference voltage), but now the charging current assumes a slight value (around a few mA). This charging process is known as float charging.

Basically, float charging consists of a low-rate constant voltage charge that is used to maintain the battery in a fully charged condition (once the batteries self discharge with time), as explained in [1][38]. Float charge is also used for maximizing the life of the battery by reducing unavoidable aging effects to minimum levels [38]. Although this procedure is used when the batteries are fully charged, on this thesis, the tests performed did not consider the battery pack full charge.

4.2.2 Control of the DC-AC Converter

The BADC control is responsible for keeping the DC bus voltage constant in both modes of operation. In the V2G mode, it detects the DC link voltage and if the voltage in the capacitor is higher than the reference voltage, the BADC increases the current magnitude (power) injected into the grid. If the voltage measured is lower than the reference, it decreases the current magnitude (power) injected into the grid to keep the DC bus voltage constant.

In the G2V mode, the opposite occurs. If the capacitor's voltage is higher than the

reference voltage, the BADC decreases the current magnitude (power) extracted from the grid. If the measured voltage is lower than the reference, it increases the current magnitude (power) extracted from the grid to keep the DC bus voltage constant.

Additionally, the BADC controls the active and reactive power that will be injected or extracted from the grid. It is responsible for synchronizing the output current with the grid's voltage phasor.

The BADC control is a Voltage Oriented Control, that usually is used for three-phase voltage inverters. As the voltage source inverter used is single-phase, it is necessary to emulate a two axis reference frame. For this purpose, an additional orthogonal component is proposed in [39] to introduce the imaginary orthogonal circuit concept, as explained in [22]. With the two orthogonal axes, the Voltage Oriented Control can be applied to the BADC.

A further comprehension of the BADC can be seen in the previous work developed by Matheus Montanini [40], which was essential for the development of this thesis.

4.3 Simulation Model

This section concerns about the power structure and the control algorithms discussed in sections 4.1 and 4.2 that were implemented in the computational environment. Also, it details the subsystems used to perform the simulation in the following subsections.

Simulation is extremely important to assess the behavior of the control algorithms with the power structure, and after data analysis, modify what is needed.

The simulation was accomplished with the software MATLAB and Simulink by MathWorks, as well as the Specialized Power Systems library under Simscape. The simulation was performed using a sampling time of 2 μs to ensure the closeness with the experimental setup. Nevertheless, the control algorithm in simulation was performed using a sampling rate of 10 kHz, due the limitation of the experimental platform, which is explained in detail in section 4.4.

4.3.1 Model Overview

Figure B.1 displays the overview of the simulation model. It shows the control structure and the power structure, with the BDC, the single-phase inverter, and the battery. The BDC comprises the two capacitors, the inductor and the two IGBTs switches. The control structure is explained further.

4.3.2 Battery Model

This block implements a generic dynamic model parameterized to represent most popular types of rechargeable batteries [41]. To ensure the closeness of the simulation with the experimental setup, the battery model used is a lead-acid battery, with a capacity of 20 Ah, with a fully charged voltage of 104.52 V, with a maximum charging current limited to 4 A and with a internal resistance of 120 mΩ.

4.3.3 Control Structure

The control structure comprises two subsystems, the controllers which are the Proportional-Integral controllers used for the discharging and for the charging mode, as the selection structure of the operation mode, and the PWM model, as displayed in figure B.2.

4.3.4 Controllers

As explained in the previous subsection, the controllers subsystem comprises the controllers used for the BDC control, and the selection structure of the operation mode. The control method was explained previously in subsection 4.2.1. The diagram of the controllers structure can be seen in figure B.3, and the schematic of each controller can be seen in figures B.4, B.5 and B.6.

4.3.5 Pulse-Width Modulation model

The PWM model can be seen in figure B.7. It compares the pulses generated by the PI controllers with the sawtooth wave, and generates the control pulses used in the IGBTs switches.

As can be noticed in figure B.7, the pulse-width modulation is the same for the discharging mode and for the charging mode, however, the signals generated for each operation mode are different. Using the power structure of figure 4.1 as reference, figure B.8 displays how are generated the pulses for controlling switches S_1 and S_2 in the V2G mode, and figure B.9 displays the pulses generation for the G2V mode. On both images, the pulses generated by the upper block controls switch S_1, and the pulses generated by the nether block controls switch S_2.

4.3.6 Parameters

A few essential parameters for the simulation are:

- Sample time for simulation: *step_time* = 2e-6 s;
- Sample time for the control system: *real_ts* = 1e-4 s;
- Switching frequency: *f_switching* = 10e+3 Hz;
- BDC converter inductance: *L* = 5.6e-3 H;
- DC bus reference voltage: *v_DCBus_ref* = 400 V;
- DC bus capacitance: *C_DC* = 1e-3 F;
- DC bus initial voltage: *C_DC_init_voltage* = 400 V;
- Nominal battery voltage: *V_bat* = 96 V;
- Nominal battery rated capacity: *Ah_bat* = 20;
- Battery initial state of charge: *SOCi_bat* = 90 %

- Proportional gain for the current controller of the BDC: *kp_bb* = 0.1;
- Integral gain for the current controller of the BDC: *ki_bb* = 10;
- Proportional gain for the first voltage controller of the BDC: *kp_cv_controller1_buck* = 20;
- Integral gain for the first voltage controller of the BDC: *ki_cv_controller1_buck* = 2;
- Proportional gain for the second voltage controller of the BDC: *kp_cv_controller2_buck* = 2;

The remainder parameters used are listed in table B.1.

4.3.7 Tests

Five simulation tests are proposed and listed below:

- *V2G mode control*;
- *G2V mode control:*
  - First stage (constant current charging);
  - Second stage (constant voltage charging);
  - Third stage (float charging).
- *Transition between V2G and G2V modes:* to evaluate the battery current and voltage peaks;

The simulation results will be discussed further, in chapter 7.

4.4 Experimental Platform

The experimental validation was achieved using a real-time development system from dSPACE. The experimental platform is composed by the dSPACE 1103 real-time controller board, dSPACE Control Desk 3.7.1, a signal conditioning module, 8 UCG 20-12 batteries, the power electronics module and the Real-time simulation model in

Simulink. Each one of these components of the experimental platform are described in the following subsections. Figure 4.3 displays the schematic of the experimental platform used for validation of the experimental results. The real workplace can be seen in figure 4.4.

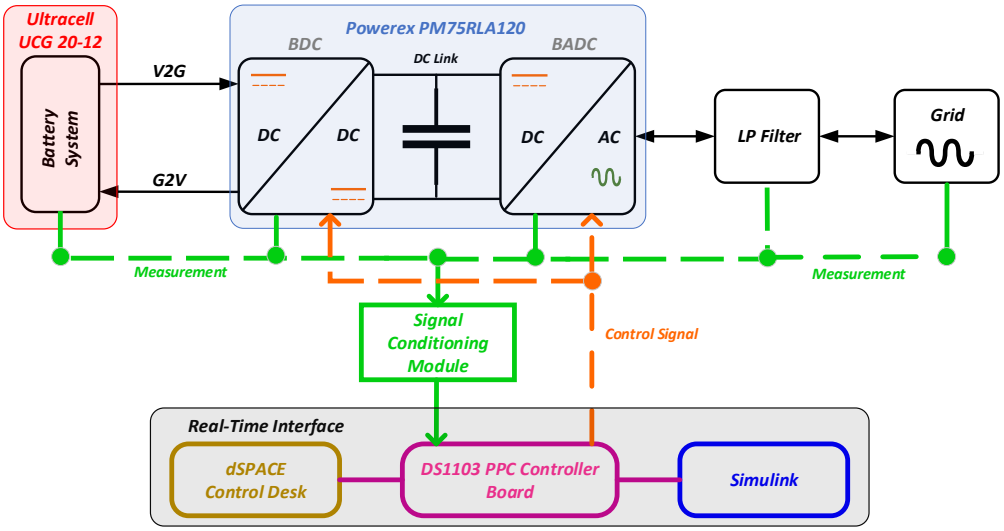

Figure 4.3: Experimental Platform Diagram

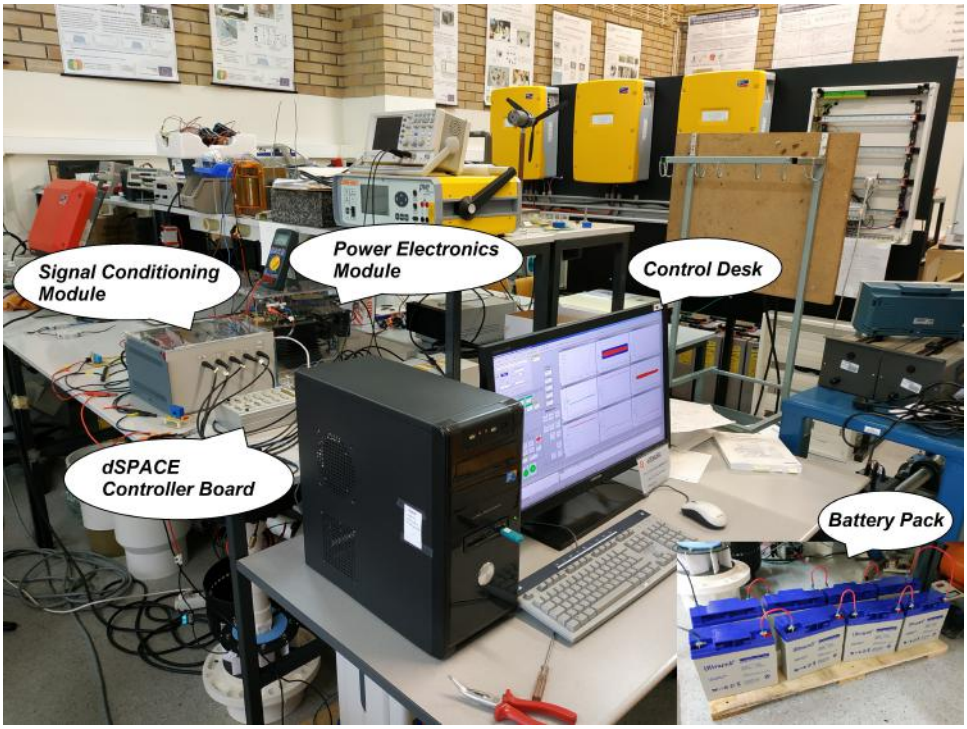

Figure 4.4: Real Workplace

Besides it, the experimental platform contains the inductor and the capacitor (used for implementing the boost converter and the buck converter), which limits the current variation as the output voltage ripple.

Considering the project of the passive elements for the boost converter, as explained in 3.1.1, and isolating Δi_L in equation 3.5, and replacing V_i (input voltage of the boost converter), D (duty-cycle), L (inductor value) and f (IGBTs' frequency operation) by the values showed in table 4.1, we reach the value displayed in equation 4.2

$$\Delta i_L = 625mA, \tag{4.2}$$

which indicates that the maximum variation of the inductor current is 312.5 mA up, and 312.5 mA down, for 250 W of power extracted from the batteries.

Parameters	**Values**
V_i	100 V
V_o	400 V
P_B	250 W
D	0.75
L	12 mH
C	1 mF
f	10 kHz

Table 4.1: Values of the parameters in the real workplace for calculating the current and voltage ripple in the discharging mode

The output voltage ripple is defined by

$$\frac{\Delta V_o}{V_o} = \frac{D}{RCf} = 0,012\%, \tag{4.3}$$

for the parameters values indicated in table 4.1.

Considering now the project of the passive elements for the buck converter, as explained in 3.1.2, and isolating Δi_L in equation 3.8, and replacing V_o, D, L and f by the

values showed in table 4.2, we reach the value displayed in

$$\Delta i_L = 625mA, \tag{4.4}$$

which indicates that the maximum variation of the inductor current is 312,5 mA up, and 312,5 mA down, as in the boost converter.

Parameters	Values
V_i	400 V
V_o	100 V
D	0.25
L	12 mH
C	1 mF
f	10 kHz

Table 4.2: Values of the parameters in the real workplace for calculating the current and voltage ripple in the charging mode

The output voltage ripple is defined by .

$$\frac{\Delta V_o}{V_o} = \frac{1-D}{8LCf^2} = 0,008\%, \tag{4.5}$$

for the parameters values indicated in table 4.2.

4.4.1 dSPACE controller board

The dSPACE real-time controller board used is the DS1103 PPC. It is specifically designed for the development of high-speed multivariable digital controllers and real-time simulations [42]. The module captures the signals measured by the signal conditioning module, interprets those signs and sends the control signals to the power module. The used module can be seen in the figure 4.5

Figure 4.5: DS1103 Controller Board box and connections'panel

4.4.2 Control Desk 3.7.1

The dSPACE Control Desk 3.7.1 is a software for seamless Electronic Control Unit (ECU) development. It is used for rapid control prototyping, hardware-in-the-loop simulation, ECU measurement, diagnostics and calibration, as explained in [43]. For this project, the software was used for monitoring the crucial variables (battery voltage, battery current, battery power, power injected/extracted into/from the grid and the DC bus voltage), to assess the controllers' performance, and also for controlling the system dynamics.

The layout of Control Desk is displayed in figure 4.6, which was modified from previous works, for the purpose of this project. For example, the DC-DC Converter

window, which contains the buttons for turning the BDC on or off, the buttons to select the charging method (constant current or constant voltage), the windows to modify the controllers' gains and assess the controllers' performance.

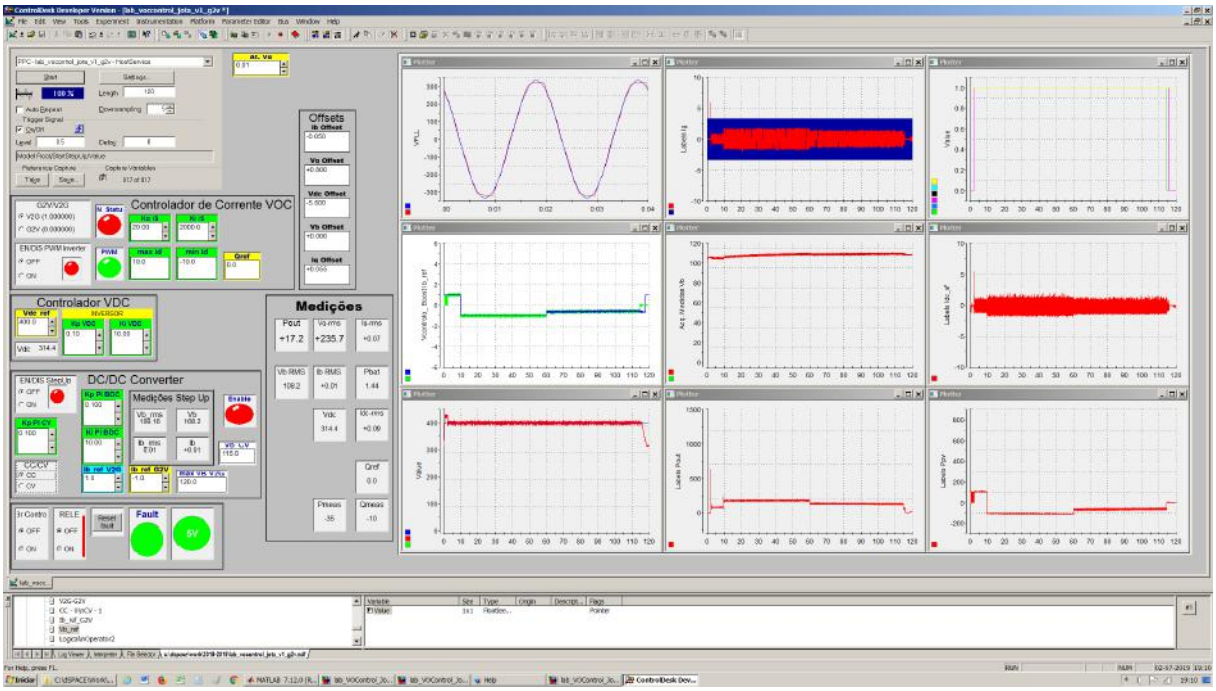

Figure 4.6: Control Desk 3.7.1 Layout showing the measurement windows and the controlling interface

4.4.3 Signal Conditioning

The signal conditioning module is used for measuring the battery current and voltage, the grid current and voltage, and the DC bus voltage.

It is composed of three TRACO Power power supplies, TML 10205 with an output of $\pm$ 5 V, TML 30215 with an output of $\pm$ 15 V, and TML 10124 with an output of 24 V. It contains five measurement channels for measuring the previously mentioned variables. Each measurement channel contains a 5^{th} order lowpass filter (performed by a LTC1065) in series with an operational amplifier (OP270), which converts the measured values to a range of $\pm$ 10 V, allowing the dSPACE controller board to read the measured signals.

An overview of the signal conditioning module is displayed in figure 4.7, and the

electric scheme for a better comprehension of the module is illustrated in figures 4.8 and 4.9.

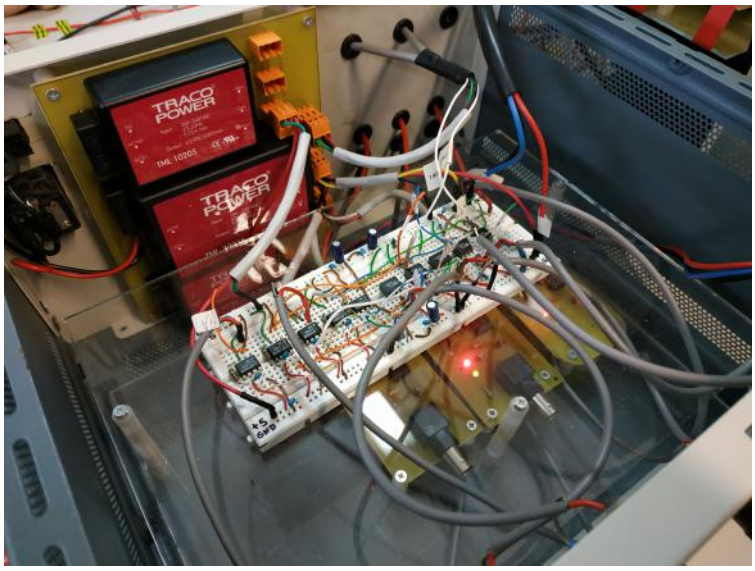

Figure 4.7: Signal Conditioning Module

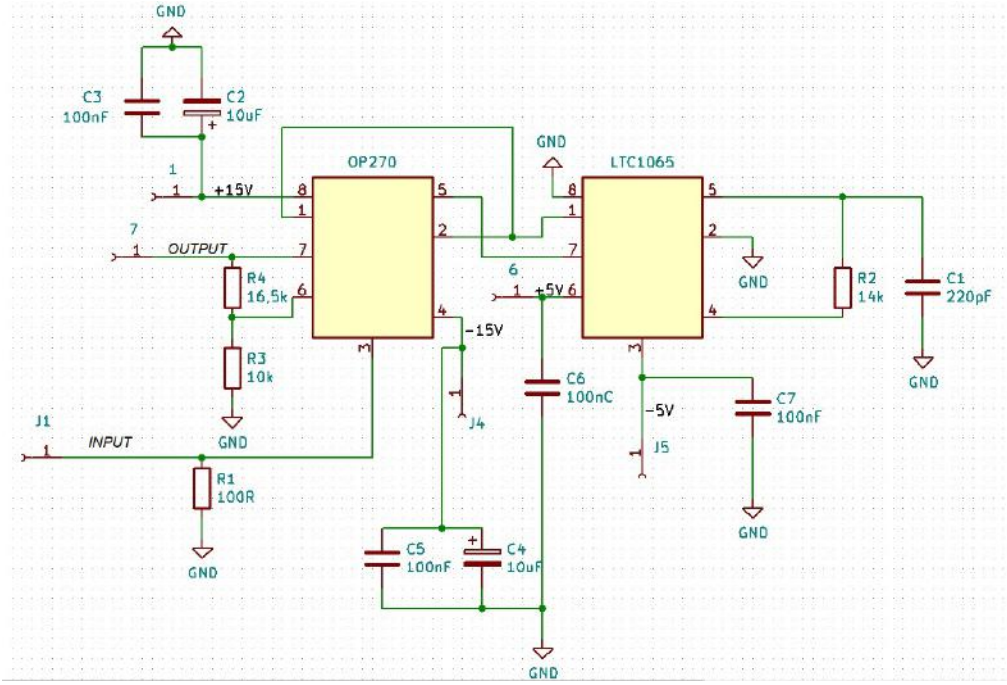

Figure 4.8: Electric scheme for current measuring in the signal conditioning module

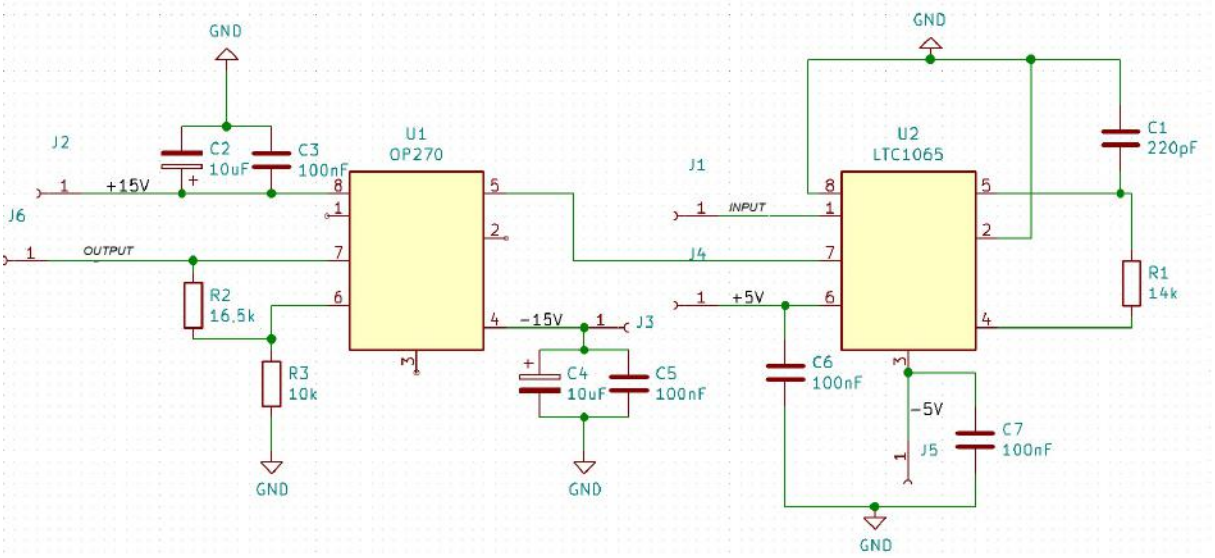

Figure 4.9: Electric scheme for voltage measuring in the signal conditioning module

4.4.4 Batteries

The batteries used for the experimental validation are 8 UCG 20-12 connected in series, as showed in figure 4.10, delivering 96 V of nominal voltage, with a capacity of 20 Ah.

Figure 4.10: Bank of batteries

4.4.5 Power Electronics Module

The physical IGBTs are located in the three phase inverter from Powerex, the integrated power module PM75RLA120, with a nominal collector current of 75 A. They are active low (with a voltage smaller than 0,8 V), they need a supply voltage around 15 V (supplied by the signal conditioning module), and the PWM input frequency must be smaller than 20 kHz. The IGBTs are isolated from the control signals by the BP7B circuit, also from Powerex, supplied by the 24 V power supply also provided by the signal conditioning module. The figure 4.11 shows the power electronics module and the location of the three phase inverter and the isolation circuit.

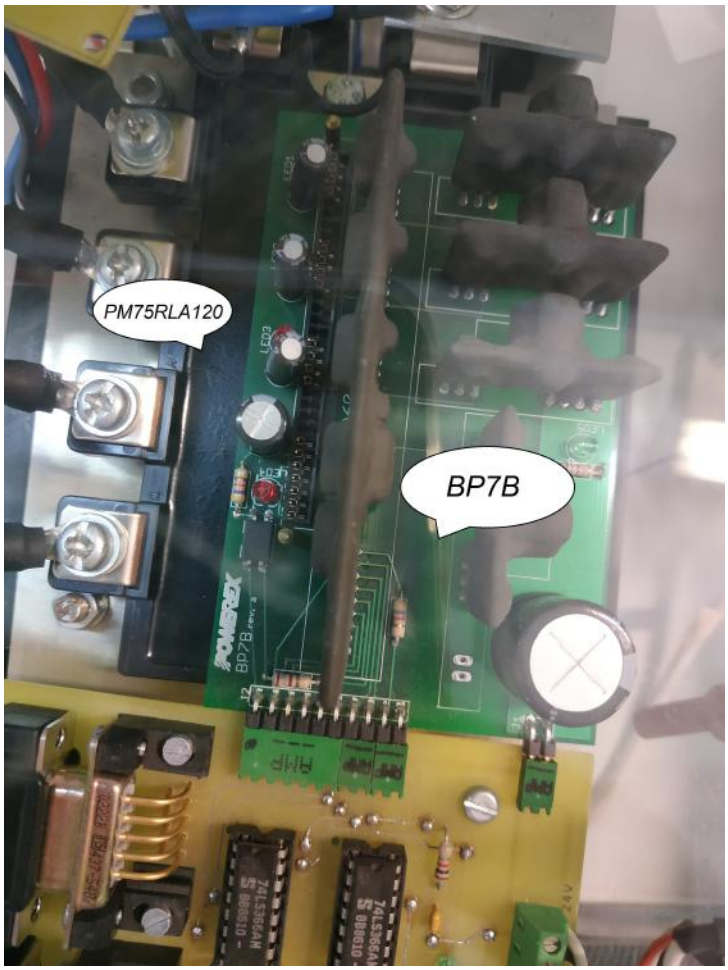

Figure 4.11: Power Electronics Module

4.4.6 Real-time simulation model in Simulink

For implementing the control logic for the power structure the MATLAB Simulink software which acts in real time was used. In the simulation, input and output blocks are provided by RTI library, from dSPACE. The model built by MATLAB can be controlled within Control Desk, allowing the real-time interfacing between the Simulink and the power module.

Chapter 5

Simulation Results

This chapter contains the results acquired via simulation of 5 tests previously explained in subsection 4.3.7. Additionally, a final test was performed, which consists of the other 5 tests performed in sequence. The PI parameters used for the validation of those tests are listed in table B.1

The simulation was performed in the discrete-time domain to ensure the direct use in the real system.

This chapter is specifically for showing the obtained simulation results. The data analysis and discussion is further, in chapter 7

5.1 Vehicle-to-Grid mode control

This section displays the results by simulating the V2G control.

Figure 5.1 shows the battery current during V2G mode, in which the reference current is generated by dividing the power required from the batteries, by the actual battery voltage, as showed in equation 4.1.

Figure 5.2 shows the current ripple during the discharging mode for a brief range of time. In chapter 7, this current variation in simulation is compared with the expected variation for the real system.

Figure 5.3 displays the battery voltage during the discharging mode.

Figure 5.4 is figure 5.3 zoomed in for showing the voltage variation during the discharging mode, where can be observed that the battery voltage is decreasing, as expected. This variation is compared with the expected voltage ripple for the real system, in chapter 7.

Figure 5.5 shows the battery SOC behaviour during the V2G mode. It slowly declines due the fact that the power required by the batteries assumes a slight value and the time range is only 5 s. However, it shows that the system is working as expected during this step.

Figure 5.6 displays the battery power during the discharging stage. As explained in subsection 4.2.1, the battery power assumes a positive value in the discharging mode, since the battery current is positive.

The brief range of time used was just for presenting the behavior of the monitored variables, where with this short space of time, it is possible to observe those variables tendencies.

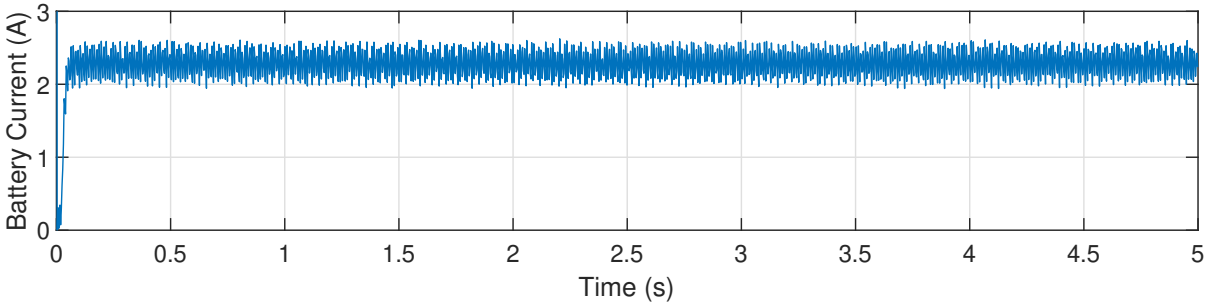

Figure 5.1: Battery current as a function of time, for the Vehicle-to-Grid mode control

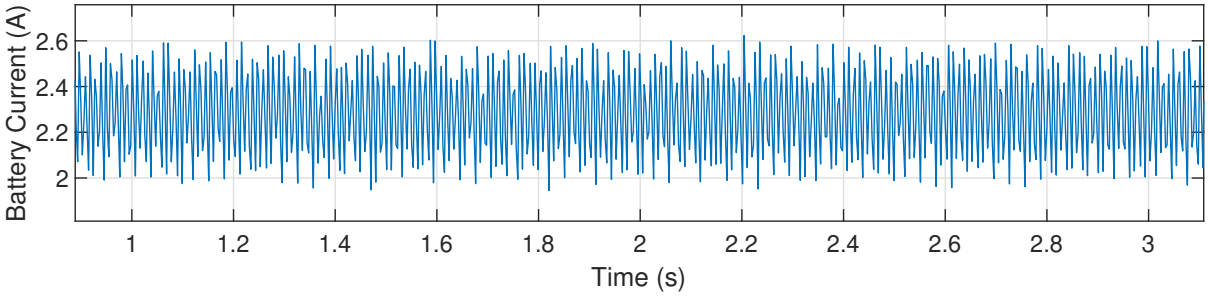

Figure 5.2: Battery current as a function of time, for the Vehicle-to-Grid mode control, zoomed in

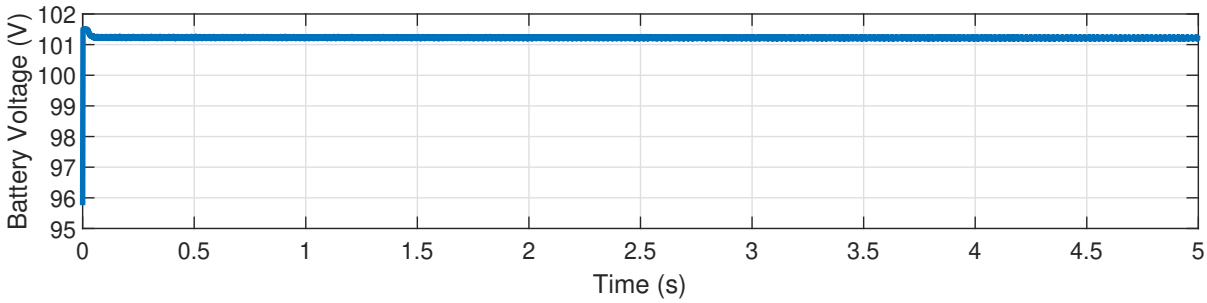

Figure 5.3: Battery voltage as a function of time, for the Vehicle-to-Grid mode control

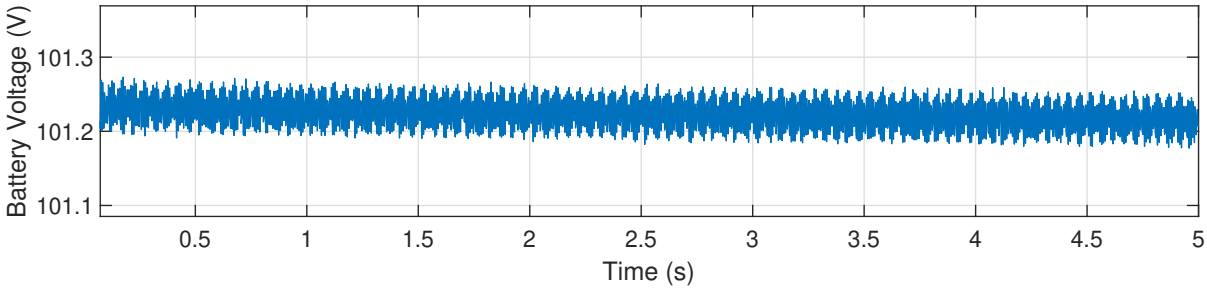

Figure 5.4: Battery voltage as a function of time, for the Vehicle-to-Grid mode control, zoomed in

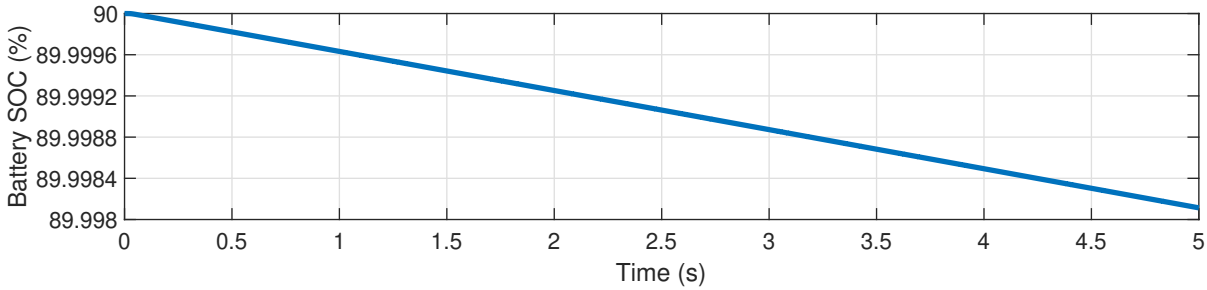

Figure 5.5: Battery State-of-Charge as a function of time, for the Vehicle-to-Grid mode control

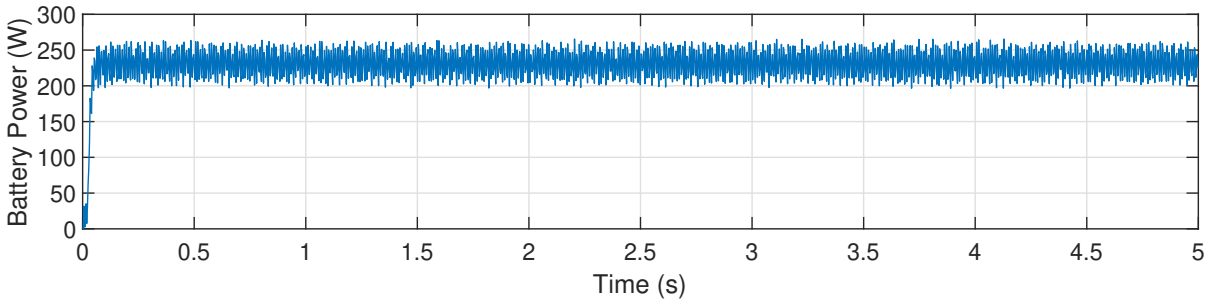

Figure 5.6: Battery power as a function of time, for the Vehicle-to-Grid mode control

5.2 Grid-to-Vehicle mode control

This section displays the results by simulating the G2V control. This test is divided in three stages, each one is displayed in the following subsections. The first one consists of constant current charging, the second consists of constant voltage charging, and the third consists of the float charging.

In the same way as explained in section 5.1, the range of time used for the G2V simulation mode was just for presenting the behavior of the monitored variables, where with this short space of time, it is possible to observe those variables tendencies.

5.2.1 Constant Current Charging

Figure 5.7 displays the battery current during constant current charging. The reference current is defined manually (4 A), and is smaller than the maximum current specified by the manufacturer [37].

Figure 5.8 shows the current ripple during the constant current charging mode for a brief range of time. This variation is compared with the expected current variation for the real system, in chapter 7.

Figure 5.9 shows the battery voltage during constant current charging.

Figure 5.10 is figure 5.9 zoomed in for showing the voltage variation during the constant current charging mode, where can be observed that the battery voltage is increasing, as expected. In chapter 7, this voltage ripple in simulation is compared with the expected variation for the real system.

Figure 5.11 displays the battery SOC during constant current charging. As can be noticed due the low variation, a significant amount of time is required for reaching the battery full charge.

Figure 5.12 shows the battery power during constant current charging. Due the low variation on the battery voltage, the battery power can be considered a mirror of the battery current, only multiplied by the voltage.

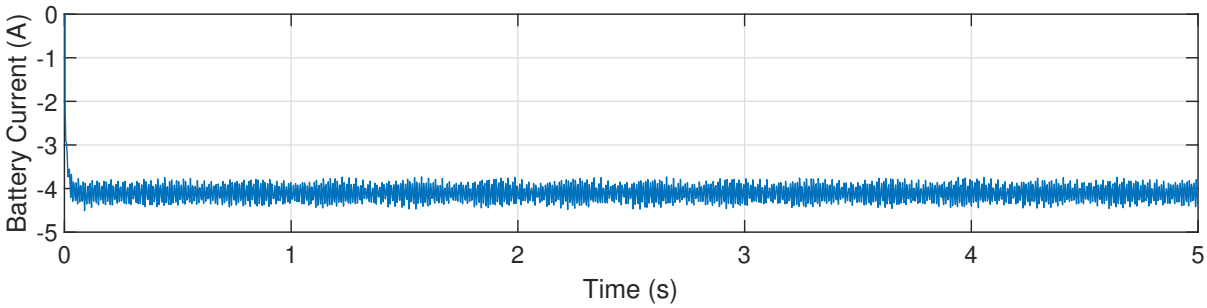

Figure 5.7: Battery current as a function of time, for the Grid-to-Vehicle mode control: constant current changing

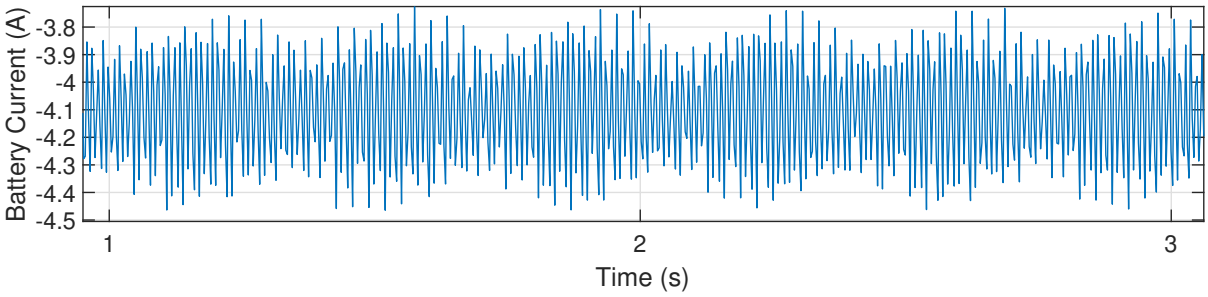

Figure 5.8: Battery current as a function of time, for the Grid-to-Vehicle mode control: constant current changing, zoomed in

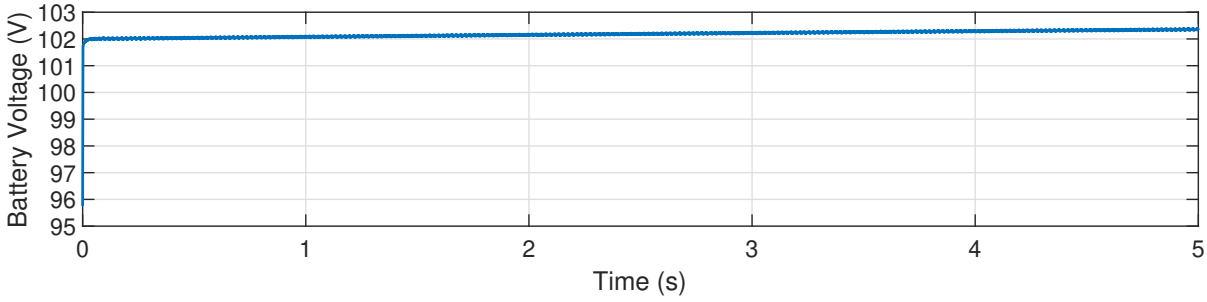

Figure 5.9: Battery voltage as a function of time, for the Grid-to-Vehicle mode control: constant current changing

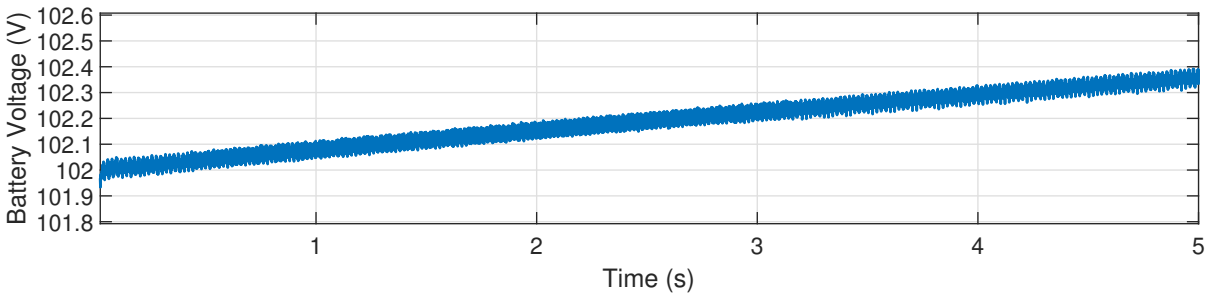

Figure 5.10: Battery voltage as a function of time, for the Grid-to-Vehicle mode control: constant current changing, zoomed in

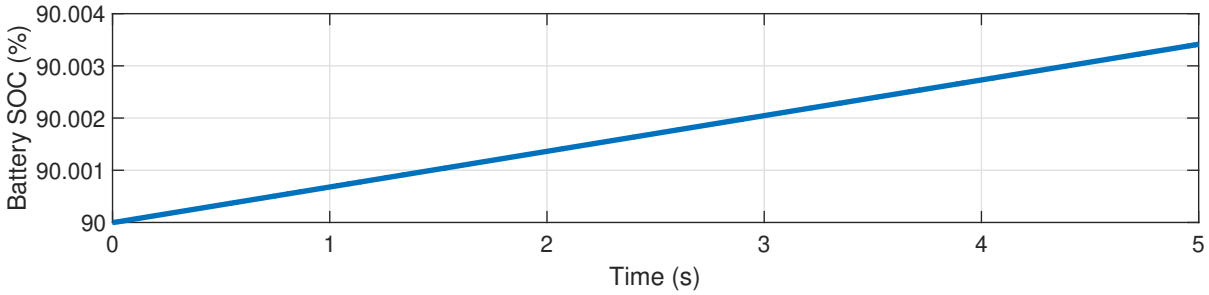

Figure 5.11: Battery State-of-Charge as a function of time, for the Grid-to-Vehicle mode control: constant current changing

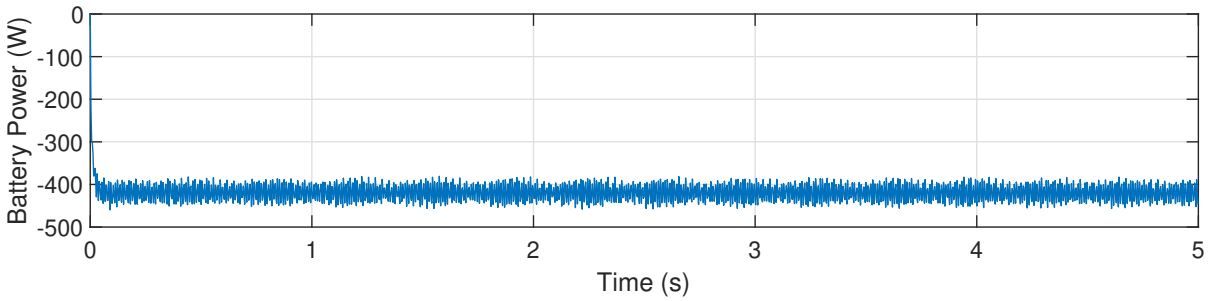

Figure 5.12: Battery power as a function of time, for the Grid-to-Vehicle mode control: constant current changing

5.2.2 Constant Voltage Charging

For the validation of the constant voltage charging test, the parameters of the first voltage controller were different from the values of table B.1, where K_p = 8 and K_i = 0.5.

Figure 5.13 displays the battery current during the second stage of the charging mode (first stage of constant voltage charging). The reference current is generated by the constant voltage controller of second step. While the battery voltage approaches the reference value (102.5 V for this stage), the charging current decreases (in absolute value).

Figure 5.14 displays the battery voltage during the first stage of constant voltage charging. Due to the brief simulation time range, it is difficult to notice the slight increase in voltage.

Figure 5.15 is figure 5.14 zoomed in for showing the voltage variation during the constant voltage charging mode, where can be observed that the battery voltage is increasing, as expected.

Figure 5.16 displays the battery SOC during the second stage of the charging mode (first stage of constant voltage charging). On the other hand, in figure 5.14, it is unequivocally that the battery is charging. And as in the constant current charging, it shows that a significant amount of time is required to completely charge the battery pack.

Figure 5.17 displays the battery power during the first stage of constant voltage charging. As explained on subsection 4.2.1, while the battery approaches the reference voltage, the current requested for charging the batteries decreases, since the battery power is a mirror of the battery current, the delivered power to the battery pack follows the same trend.

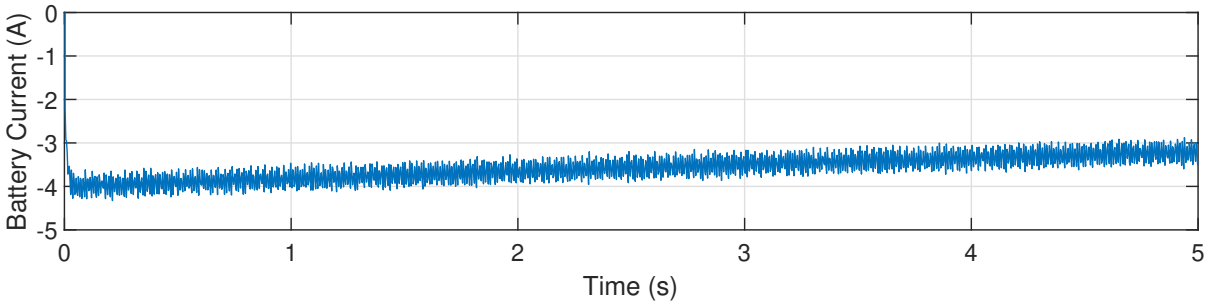

Figure 5.13: Battery current as a function of time, for the Grid-to-Vehicle mode control: constant voltage changing

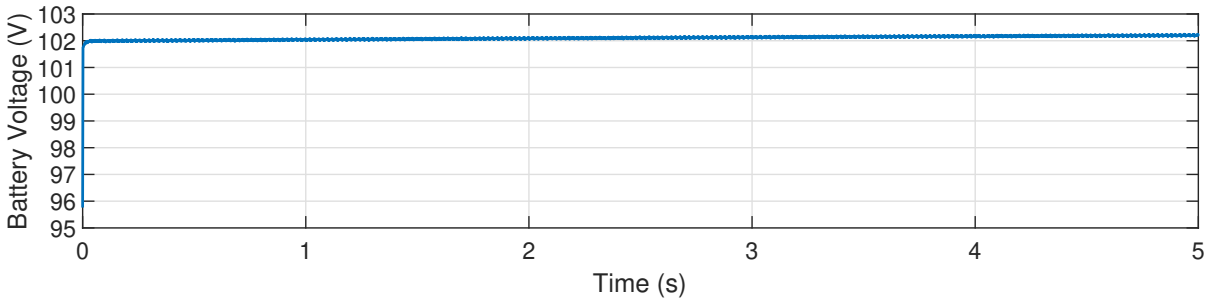

Figure 5.14: Battery voltage as a function of time, for the Grid-to-Vehicle mode control: constant voltage changing

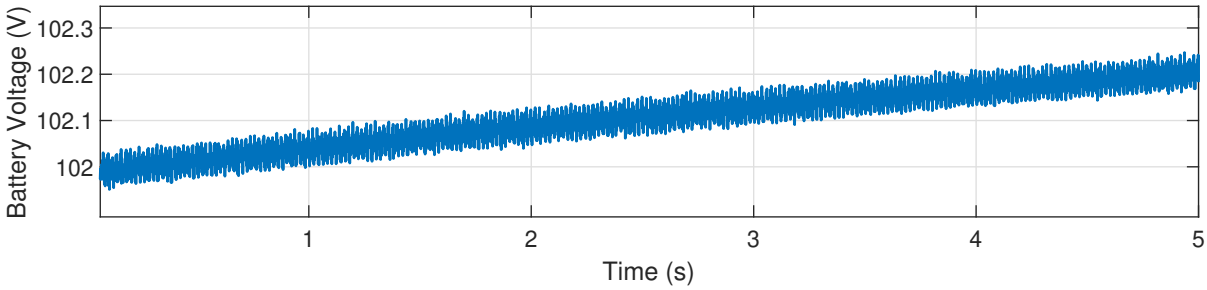

Figure 5.15: Battery voltage as a function of time, for the Grid-to-Vehicle mode control: constant voltage changing, zoomed in

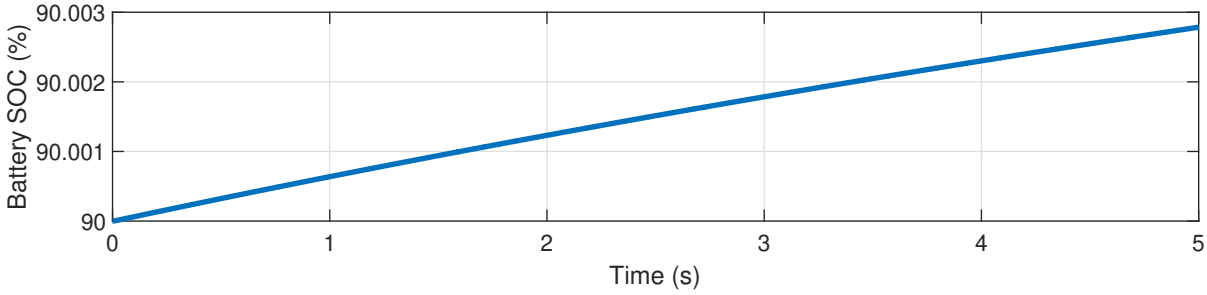

Figure 5.16: Battery State-of-Charge as a function of time, for the Grid-to-Vehicle mode control: constant voltage changing

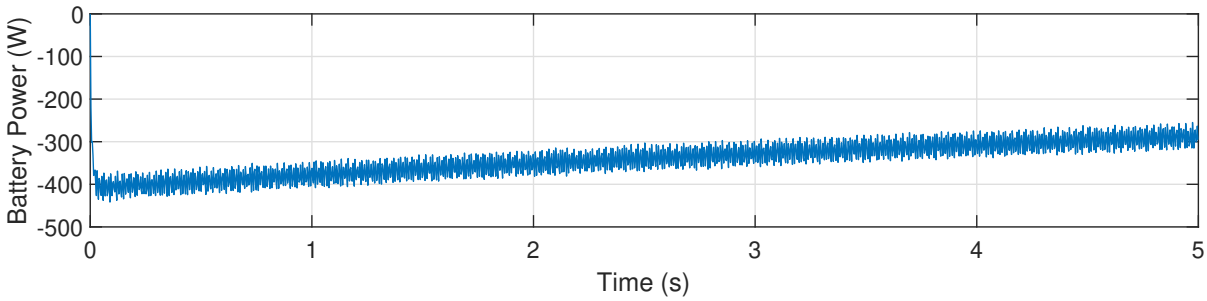

Figure 5.17: Battery power as a function of time, for the Grid-to-Vehicle mode control: constant voltage changing

5.2.3 Float Charging

For the validation of the constant voltage charging test, the parameter of the second voltage controller was different from the value presented on table B.1, where for this test $K_p = 1$.

To obtain the images presented on this test, the structure used for the second voltage controller was different than the structure presented on figure B.6. An unitary negative gain was necessary for inverting the signal of the error, once the measured voltage on this specific test is smaller than the reference voltage, and to generate a negative reference current the error signal must be inverted.

Figure 5.18 displays the battery current during float charging. As the current assumes a slight value, and the simulation time range is limited in 5 s, the battery current mitigation is imperceptible.

Figure 5.19 displays the battery voltage during the third stage of the charging mode. The reference current is generated by the constant voltage controller of third step (which the reference value is 102.1 V for this situation).

Figure 5.20 is figure 5.19 zoomed in for showing the voltage variation during the float charging mode, where can be observed that the battery voltage is increasing, as expected. As the battery charging current is very small, the battery voltage increases slowly.

Figure 5.21 displays the battery SOC during float charging. As the battery charging

current is very small, the increase of the State-of-Charge is much slower when compared with the other two stages of the Grid-to-Vehicle mode (figures 5.11 and 5.16).

Figure 5.22 displays the battery power during the third stage of the charging mode. The power required for charging the batteries is pitiful. It is only used when the batteries are almost fully charged.

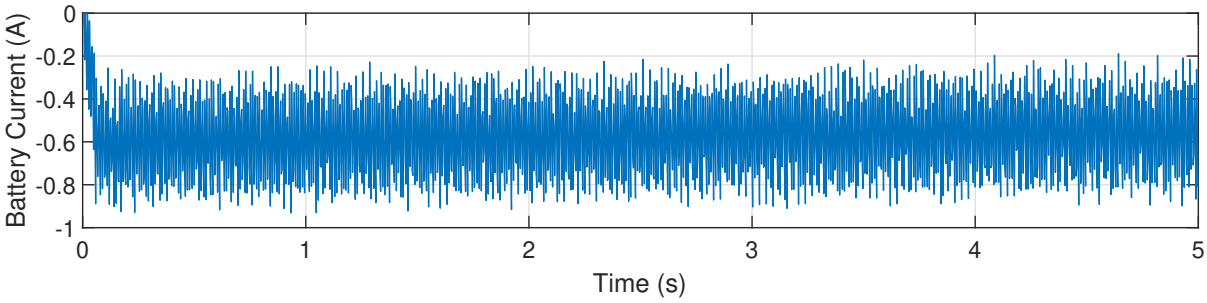

Figure 5.18: Battery current as a function of time, for the Grid-to-Vehicle mode control: float changing

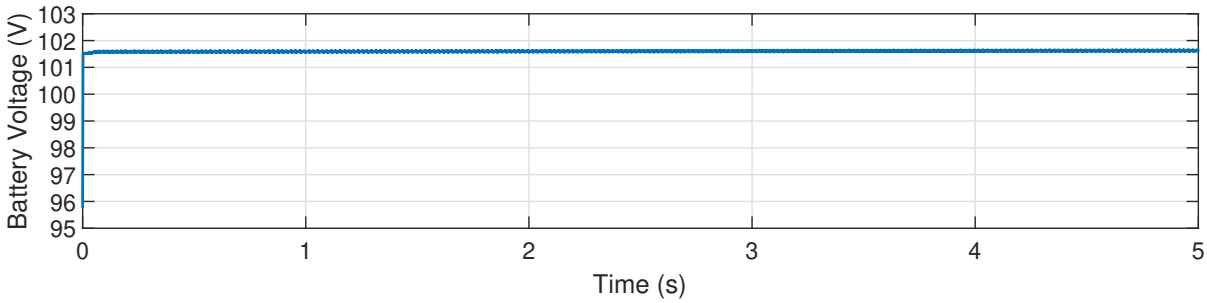

Figure 5.19: Battery voltage as a function of time, for the Grid-to-Vehicle mode control: float changing

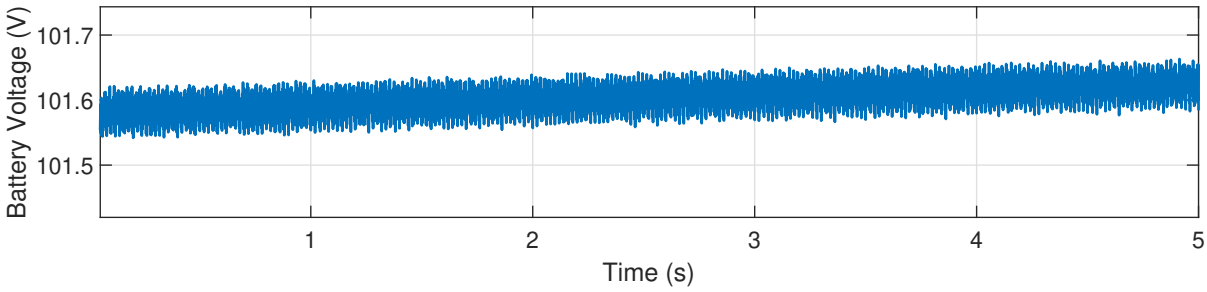

Figure 5.20: Battery voltage as a function of time, for the Grid-to-Vehicle mode control: float changing, zoomed in

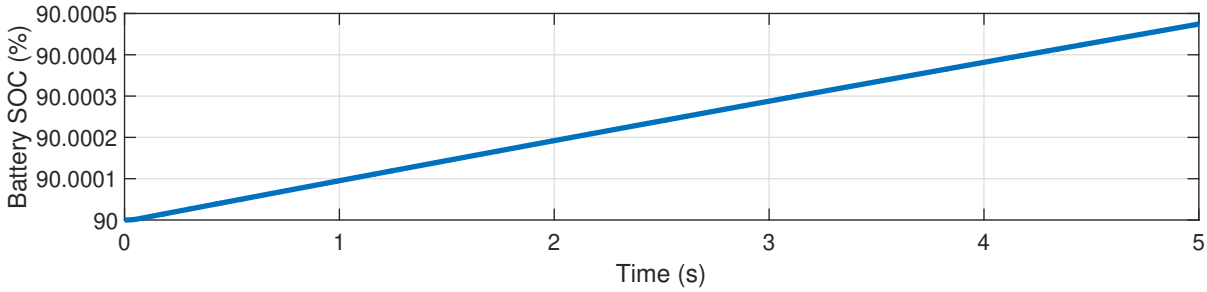

Figure 5.21: Battery State-of-Charge as a function of time, for the Grid-to-Vehicle mode control: float changing

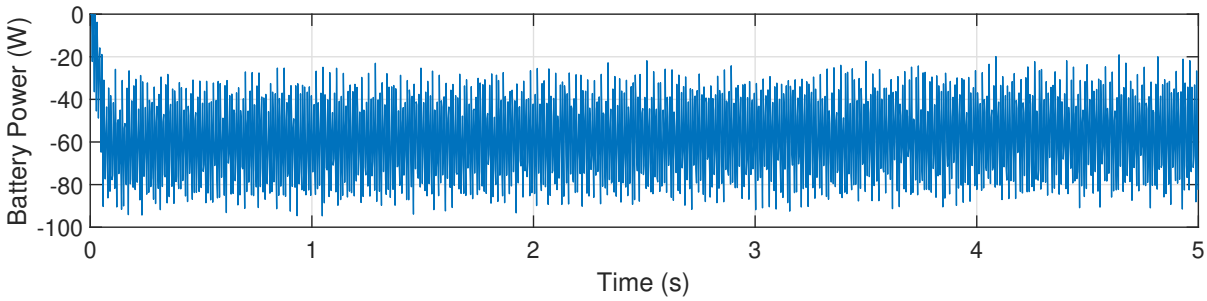

Figure 5.22: Battery power as a function of time, for the Grid-to-Vehicle mode control: float changing

5.3 Transition between operation modes

This section displays the results by simulating the transition between the V2G and the G2V operation modes.

For the validation of the transition between operation modes test, the parameters of the first voltage controller were the same values of table B.1.

Figure 5.23 displays the battery current during transition between modes (V2G, G2V). On this test, the battery current in the Grid-to-Vehicle mode is controlled by the constant current controller, which is the first stage of the charging step. It is notable by the chart that transition between both stages happens smoothly.

Figure 5.24 shows the battery voltage during transition between both stages (V2G, G2V).

Figure 5.25 is figure 5.24 zoomed in for showing that in the Vehicle-to-Grid mode,

the battery is discharging, and in the Grid-to-Vehicle mode, the battery is charging.

Figure 5.26 shows the battery SOC during transition between both modes (V2G, G2V). It declines during the discharging mode, and increases during the charging mode.

Figure 5.27 displays the battery power during transition between stages (V2G, G2V). As the battery voltage shows almost no variation during both modes, the battery power chart is similar to the battery current.

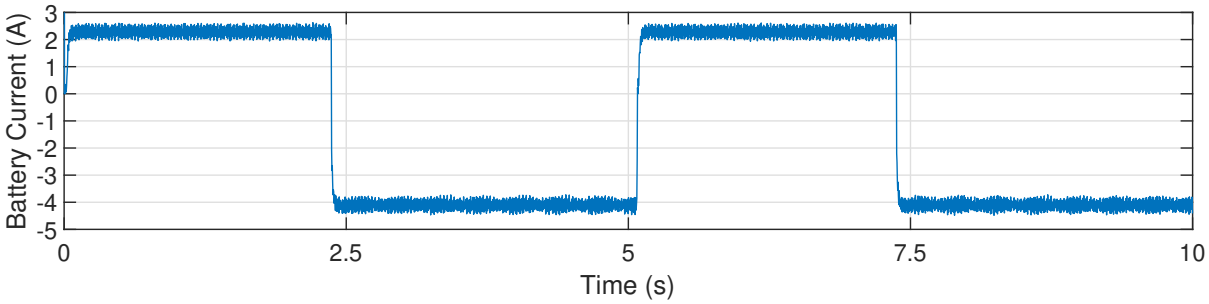

Figure 5.23: Battery current as a function of time, for the transition between V2G and G2V modes

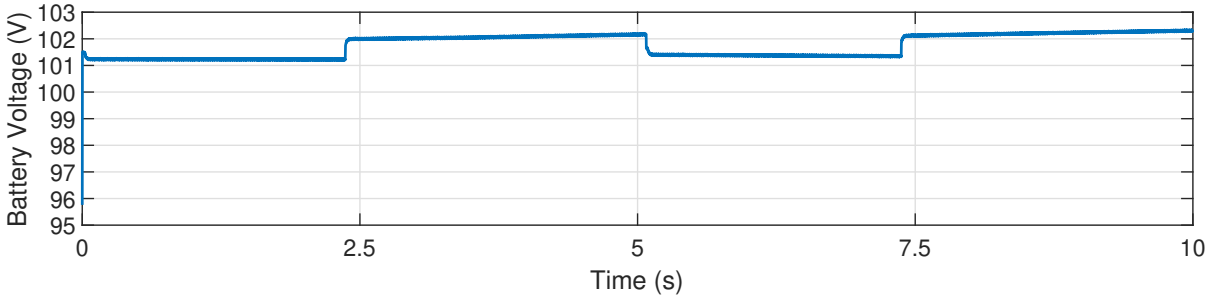

Figure 5.24: Battery voltage as a function of time, for the transition between V2G and G2V modes

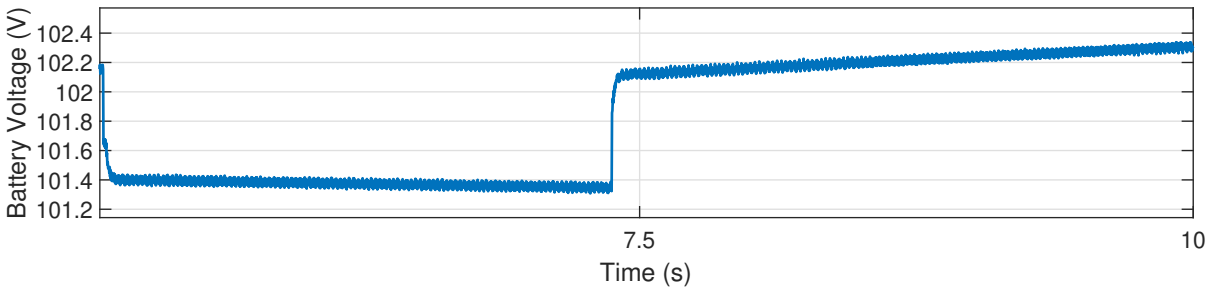

Figure 5.25: Battery voltage as a function of time, for the transition between V2G and G2V modes

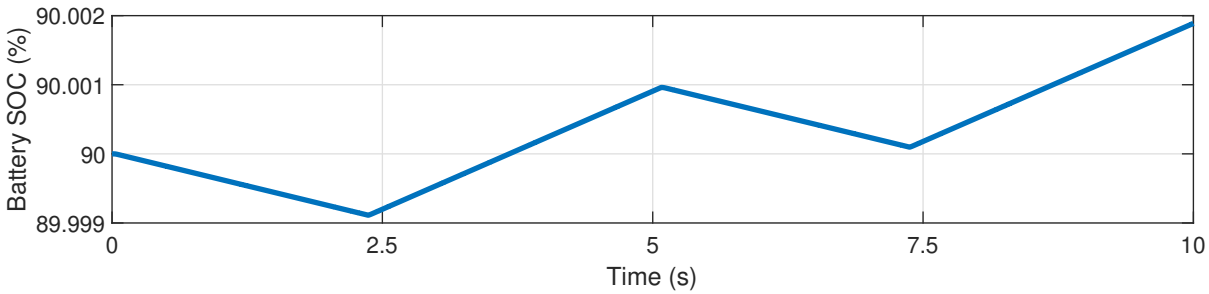

Figure 5.26: Battery State-of-Charge as a function of time, for the transition between V2G and G2V modes

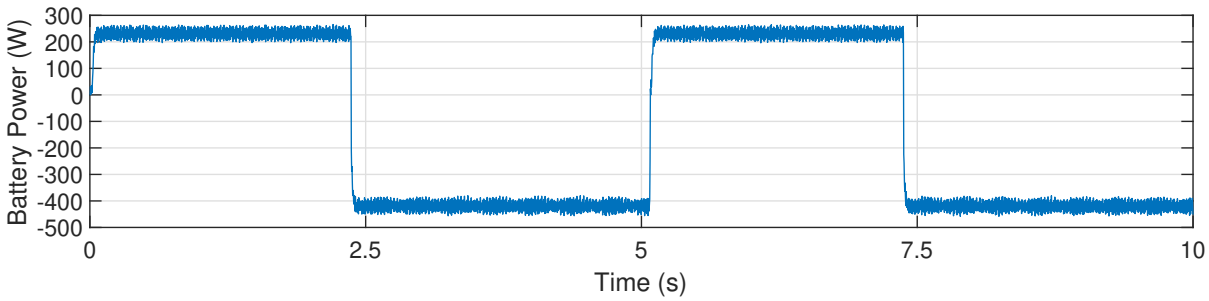

Figure 5.27: Battery power as a function of time, for the transition between V2G and G2V modes

5.4 Embedded Tests

This section contains the results by simulating all the other 5 tests displayed before in sections 5.1, 5.2 and 5.3, on sequence. However, this test limits the two first steps of the charging mode, due the limitations of computational hardware. It means that in the constant current charging the battery voltage does not reach its maximum value, and in the constant voltage charging, the battery current does not fall to a residual value, because a huge amount of time and consequently RAM memory would be necessary to completely perform those tests. On both stages, battery voltage and current reach a pre-determined value and, then, it starts the next step of charging.

For the validation of the transition between operation modes test, the parameters of the first voltage controller were the same values of table B.1.

The test starts with the V2G mode, and when it reaches a pre-determined time (on

this case, 1 s), it changes the operation mode (transition test). On the G2V mode, the battery is charged with a constant current, around 4 A (negative since the battery is absorbing power). When the battery voltage reaches 102.5 V, the charging stage changes for the constant voltage charging, and it starts charging the battery with a reference voltage of 102.5 V, while the charging current gradually decreases (in absolute value). Finally, when the battery current hits 1.5 A, the last charging stage begins. Then, the battery is charged with a reference voltage of 102.1 V, and an slight current is limited around 400 mA.

Figures 5.28, 5.29, 5.30 and 5.31 show the behaviour of the battery current, voltage, SOC and the battery power, respectively.

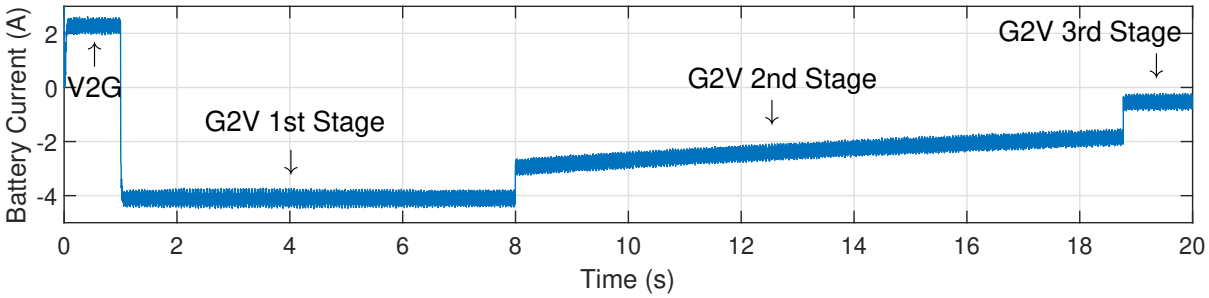

Figure 5.28: Battery current during a complete test

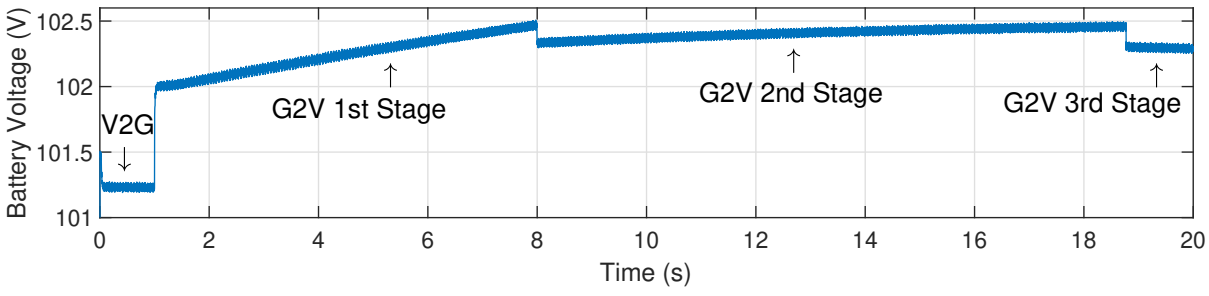

Figure 5.29: Battery voltage during a complete test

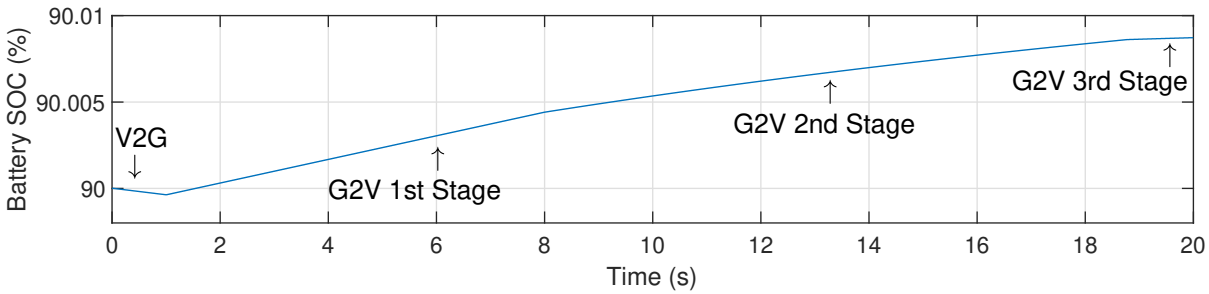

Figure 5.30: Battery State-of-Charge during a complete test

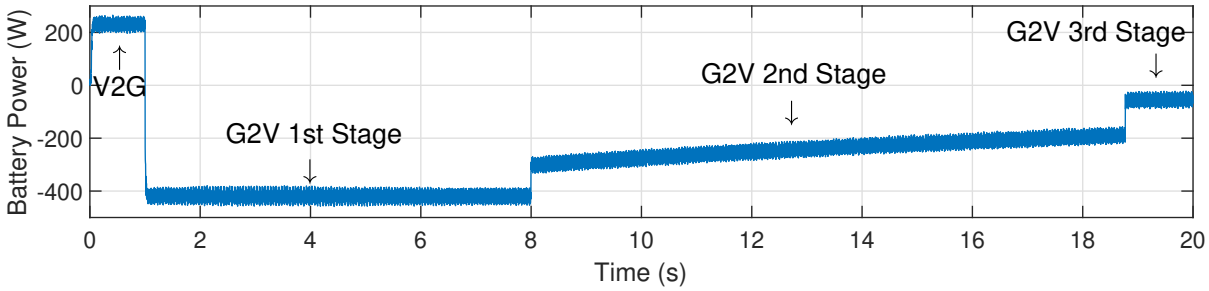

Figure 5.31: Battery power during a complete test

Chapter 6

Experimental Results

This chapter contains the experimental tests results with the platform described in 4.4.

The same tests performed in simulation (chapter 5) were performed experimentally, with an exception for the third stage of the Grid-to-Vehicle mode, due to the physical limitation of the real workplace. As explained before in 4.2.1, the float charging test requires a slight charging current, and with a slight current a longer time to observe a variation in the battery voltage, and, as consequence, a lot of data to store. Besides it, this voltage variation would be pitiful. Therefore, this test was not performed.

The tests performed are listed as it follows:

- *V2G control*;
- *G2V control*;
  - *Constant current charging*;
  - *Constant voltage charging*;
- *Transition between V2G and G2V modes*.

The PI parameters used for the experimental validation are different from the PI parameters used for simulation. The proportional and integral constants for the experimental tests were changed for optimizing the system behaviour. And these parameters are listed in table 6.1. During the experimental tests, those values were changed to improve the system's behaviour.

Parameters	Experimental Values
Current Controller	
kp_cc	0.1
ki_cc	10
Constant Voltage Controller	
kp_cv	0.1

Table 6.1: Parameters for experimental validation

The tests performed experimentally were controlled by the user, in order to avoid risks, as an algorithm failure that could damage any component of the experimental platform. Also, the tests were performed gradually, initiating by the V2G control. Once this one was validated, the transition and the G2V control were tested along with the discharging control.

The following sections give further explanations about the tests performed.

6.1 Vehicle-to-Grid control

The V2G test displays the battery current, battery voltage, battery power and the output power of the system during the discharging mode, by figures 6.1 and 6.2, respectively. Also, the DC link voltage is displayed in figure 6.4 for demonstrating the operation stability (if the system is stable, the DC link voltage assumes a value around 400 V).

During the initial 3 s, the DC-DC converter is off, and then, it is turned on with a reference current of 1 A, then, the current is gradually increased by 1 A, until it reaches 4 A. After that, the experiment is concluded as can be seen in figure 6.1. While the current increases, the battery voltage decreases, indicating that the battery pack is discharging. The purpose of the current variation is to analyze the performance of the PI parameters used during this mode. For this test, the used PI values were the same

from table 6.1.

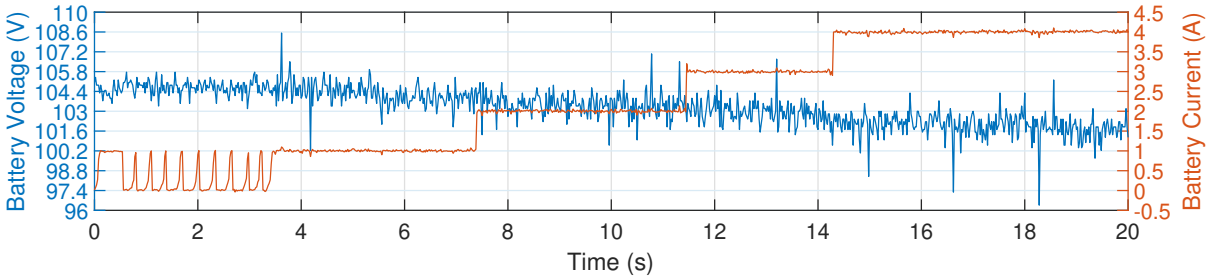

Figure 6.1: Battery voltage and current during Vehicle-to-Grid operation mode.

Figure 6.2 displays the battery power behaviour and the output power during the discharging mode. Figure 6.3 displays the system's efficiency, considering the power delivered by the batteries and the power injected into the grid.

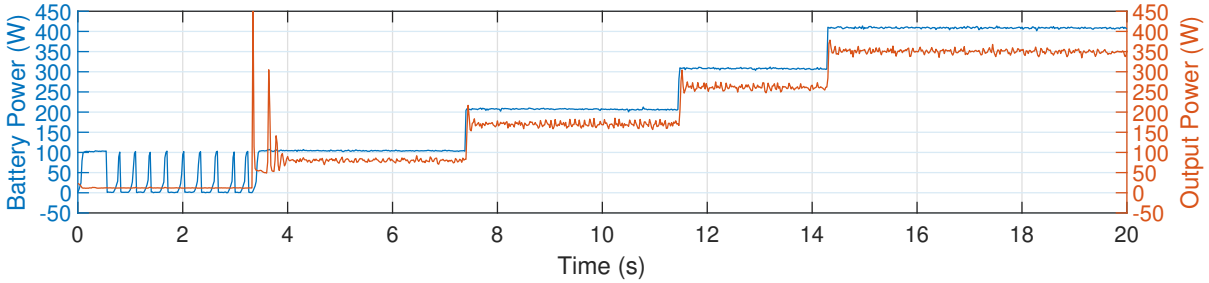

Figure 6.2: Battery power and Output Power during Vehicle-to-Grid operation mode.

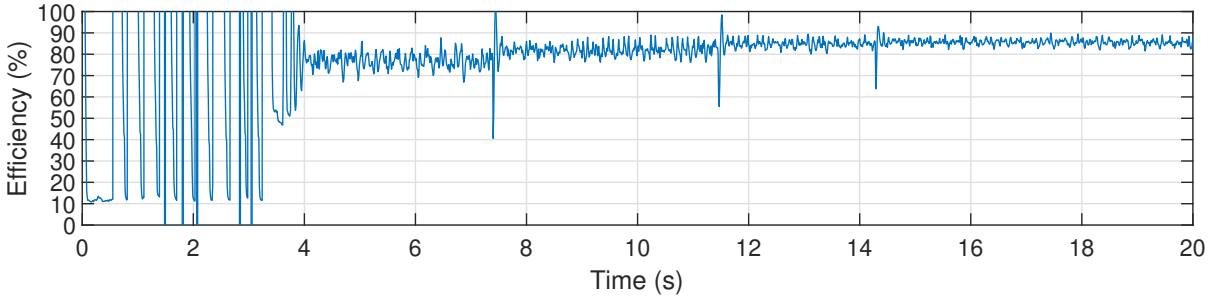

Figure 6.3: System's efficiency during Vehicle-to-Grid operation mode.

During the first 4 s of the experiment, the overvoltage protection is acting, avoiding the DC link voltage to exceed the maximum value (420 V, as can be seen in figure 6.4), generating the surges presented. Considering the remainder 16 s, it is possible to

observe that the higher the power extracted from the batteries, the higher is the system efficiency.

The DC Link voltage is displayed in figure 6.4 for showing the system's stability.

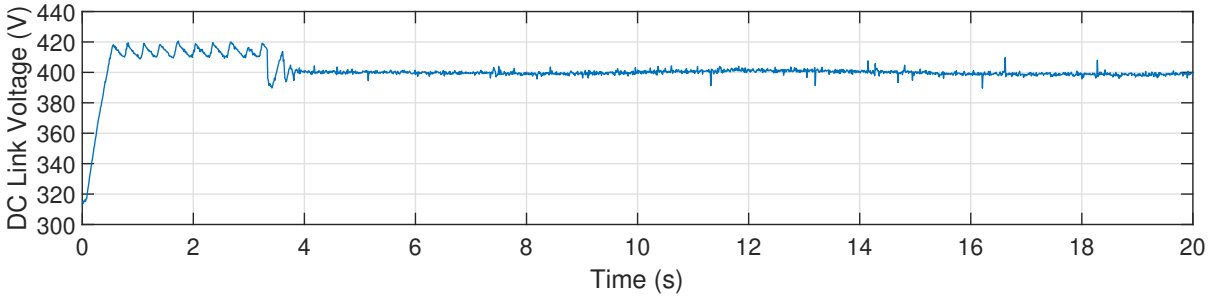

Figure 6.4: DC Link voltage during Vehicle-to-Grid operation mode.

6.2 Discharging/transition/Charging modes

Once validated the V2G control, the next step is to validate the transition between the V2G and G2V operation modes.

Figure 6.5 displays the dynamic of the test. During the initial 7 s, the BDC is off, and then it is turned on and initiates the V2G control. Around 12 s, the power flow changes the direction: it flows from the grid to the vehicle, inverting the current direction.

By analysing figure 6.5 it is possible to observe that transition of the modes occurs without any surges, which validates the transition test. It is also noticeable that, the battery voltage decreases in the V2G mode, indicating that the batteries are discharging. On the other hand, the battery voltage increases in the G2V, indicating that the batteries are charging.

The G2V control displayed consists of the first stage of the charging mode (constant current charging).

The PI parameters used for the discharging/transition/charging test were also the same from table 6.1.

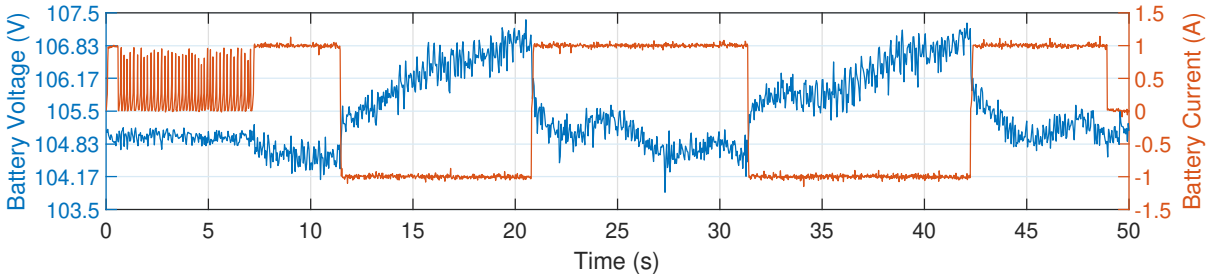

Figure 6.5: Battery voltage and current during the discharging, transition and the charging modes

Figure 6.6 displays the battery power and the output power, and figure 6.7 shows the DC Link voltage during the test. During the initial 7 s, it is possible to observe the overvoltage protection acting, and figure 6.7 shows the current voltage in the DC link during this protection.

The system's efficiency in the transition test is not displayed because it is not the main objective of this specific test.

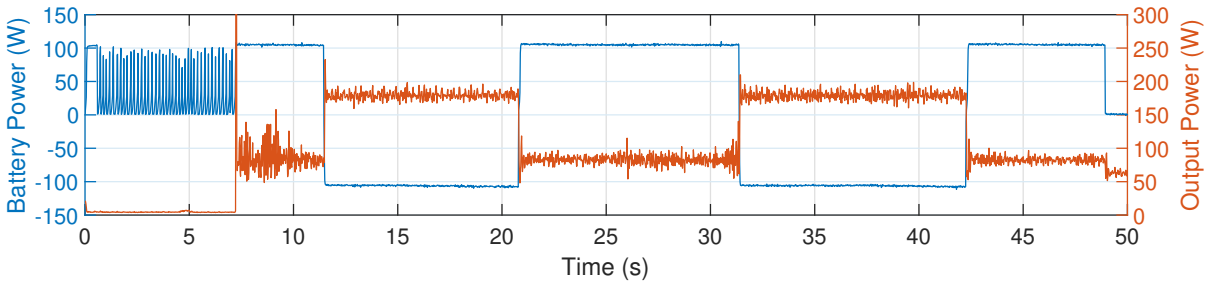

Figure 6.6: Battery power and output power during the discharging mode, transition and the charging mode

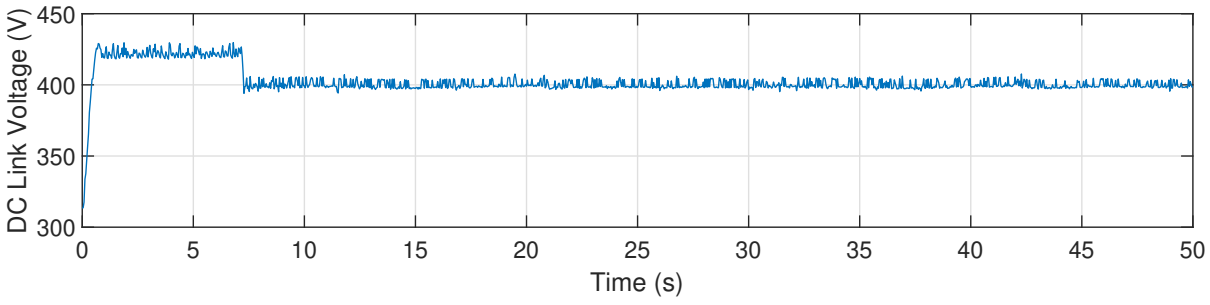

Figure 6.7: DC Link voltage during the discharging mode, transition and the charging mode

6.3 Grid-to-Vehicle control

This section presents the main results of the battery current, battery voltage, battery power and the output power. Moreover, the DC Link voltage is evaluated for two stages in the charging mode.

Firstly, the constant current charging was validated, thereafter, the constant voltage charging was validated.

6.3.1 Constant Current Charging

Figure 6.8 show the validation of the constant current charging, despite the fact of it was demonstrated in section 6.2. The reference current was modified during the experiment to assess the current controller performance.

Figure 6.8 displays the dynamic of battery current and voltage during the constant current charging test. It shows that the larger current, the faster the battery pack charges. It is possible to conclude that the SOC is increasing during the charging process due the increase in the voltage curve.

Figure 6.9 shows the power delivered from the batteries to the grid during the 3 s until 10 s, and the real power injected into the grid. After that, from the 10 s until the end of the test, the chart shows the power returned from grid to the batteries, and the real power absorbed by the batteries.

Once the system's efficiency during the V2G mode is displayed in figure 6.3, figure 6.10 displays the system's efficiency during the constant current charging mode, which occurs from 10 s until the end of the test. In other words, figure 6.10 shows the real power absorbed by the battery pack during the constant current charging mode.

Figure 6.11 illustrate the voltage in the capacitor of the DC Link, indicating that the system is stable.

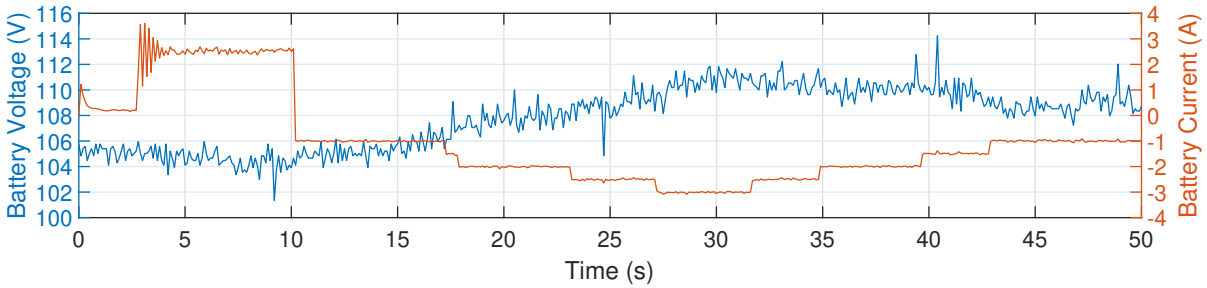

Figure 6.8: Charging current and battery voltage during constant current charging.

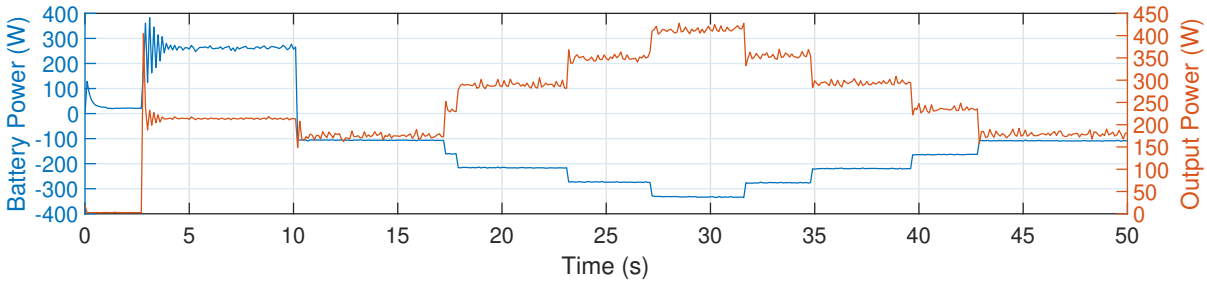

Figure 6.9: Battery power and output power during constant current charging.

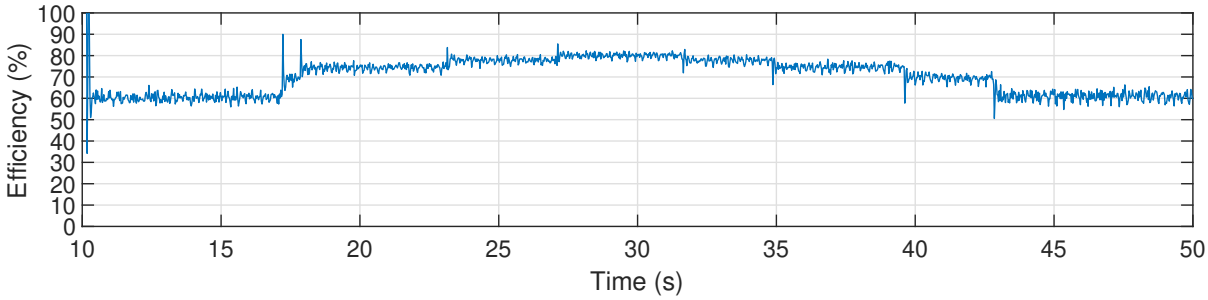

Figure 6.10: System's efficiency during constant current charging.

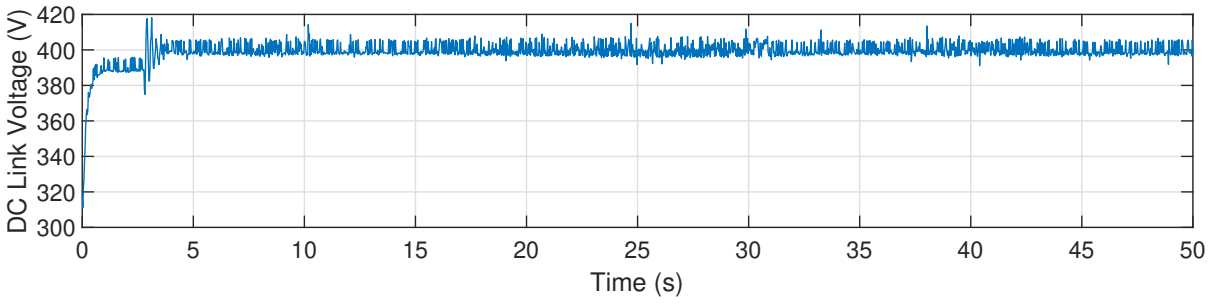

Figure 6.11: DC Link voltage during constant current charging.

The presented surges showed in figures 6.8, 6.9 and 6.11 around 3s, occur due to the PI parameters of the current controller when the BDC is turned on. For the constant current charging experiment, the parameters were changed to observe the controller performance. Although in the stationary regime the controller response is suitable, the transient must be improved.

6.3.2 Constant Voltage Charging

Figure 6.12 shows a quick performed test for the constant voltage charging validation. The experiment begins with the V2G mode, then it changes to the G2V mode, with constant current charging after around 10 s. Then, the constant voltage charging initiates around 40 s. It is possible to observe that while the battery voltage increases, the charging current decreases in absolute value, indicating that the battery is charging.

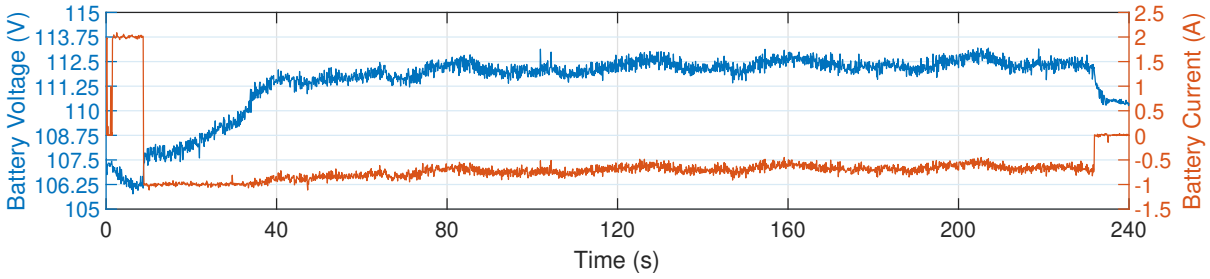

Figure 6.12: Battery current and voltage during constant voltage charging.

A final test was performed for 12 minutes to observe the constant voltage charging mode and also the previously tests, detailed in sections 6.1 and 6.2, and subsection 6.3.1. Figures 6.13, 6.14 and 6.15 show the battery voltage and current during the whole experiment. During the first minute, the V2G mode is selected and the battery is discharged, as showed in figure 6.13. For the next 60 seconds, the BDC starts to operate in G2V mode with constant current charging. Around 120 s of the experiment the constant voltage charging starts to operate. For this test (constant voltage charging), the used reference voltage for the voltage controller was 115 V, with a K_p equals to 0.1.

While the measured voltage gets close to the reference voltage, the charging current

decreases (in absolute value), and the charging process becomes slower. It happens because the used reference current for the current controller is generated from the voltage controller, as displayed in figure 4.2. Therefore, when the battery voltage becomes closer to the reference voltage, the battery needs less current to reach the set-point.

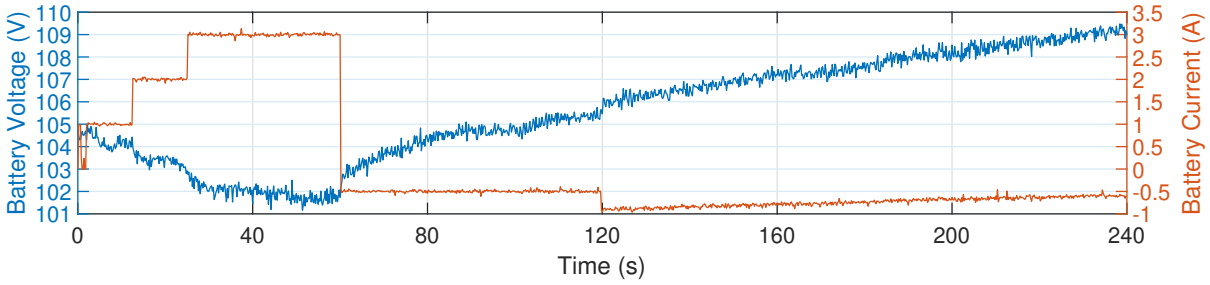

Figure 6.13: Battery current and voltage during constant voltage charging (0 - 4 minutes).

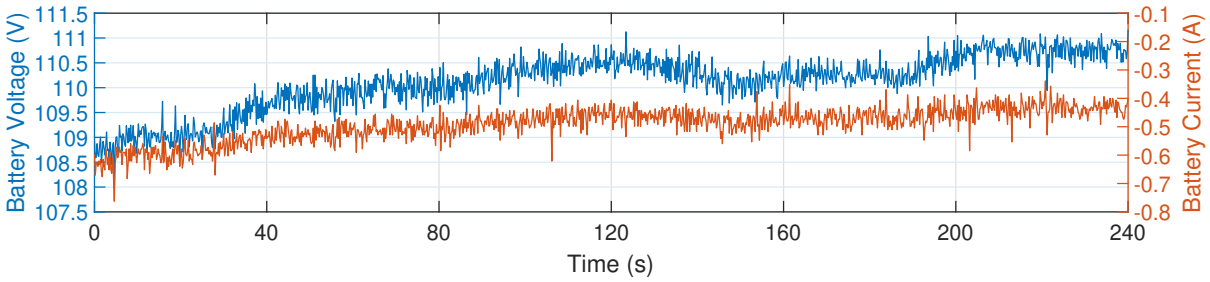

Figure 6.14: Battery current and voltage during constant voltage charging (4 - 8 minutes).

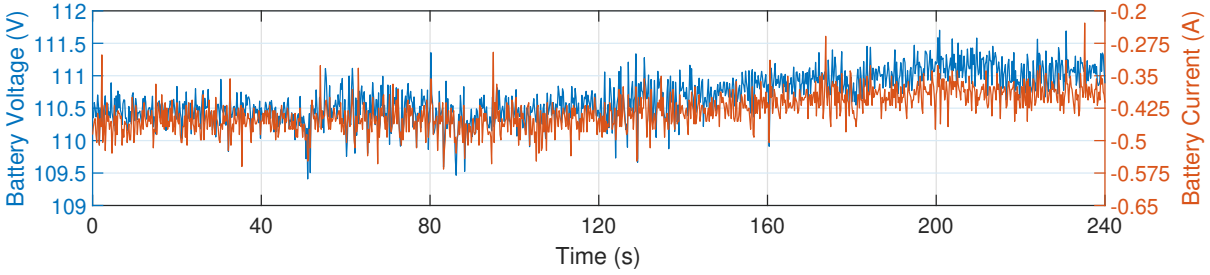

Figure 6.15: Battery current and voltage during constant voltage charging (8 - 12 minutes).

Figures 6.16, 6.17 and 6.18 illustrate the battery power and the output power behaviour in the constant voltage charging mode.

In the discharging mode, the batteries deliver more than 300 W for the grid. During the G2V mode, while the measured voltage gets closer to the reference voltage, the extracted power from the grid for charging the batteries becomes smaller.

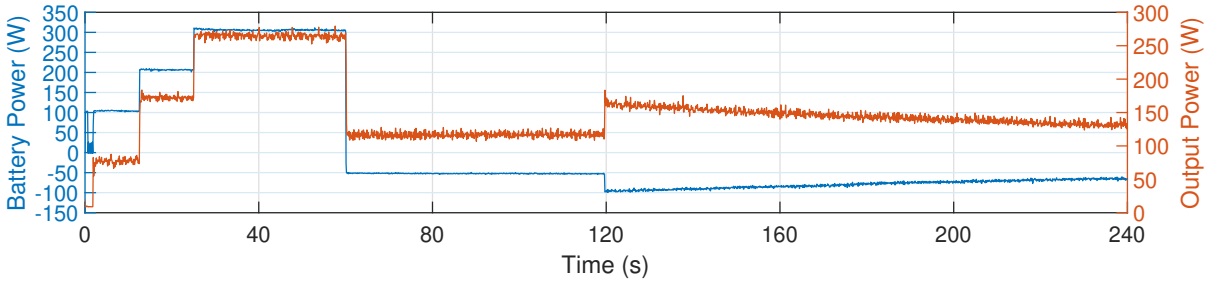

Figure 6.16: Battery power and output power during constant voltage charging (0 - 4 minutes).

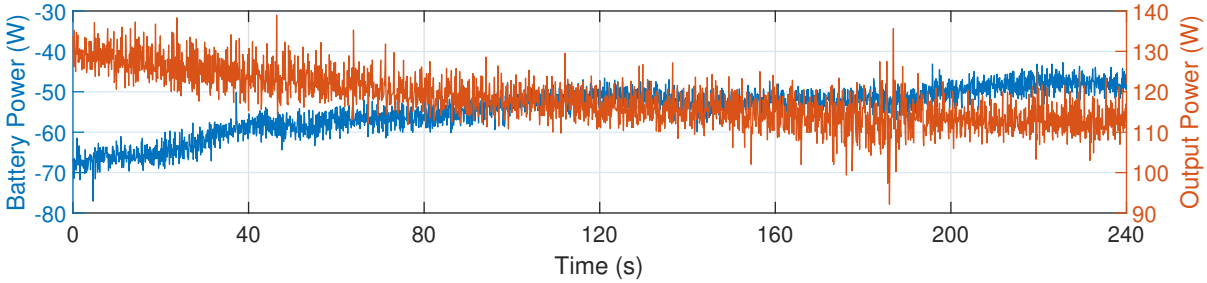

Figure 6.17: Battery power and output power during constant voltage charging (4 - 8 minutes).

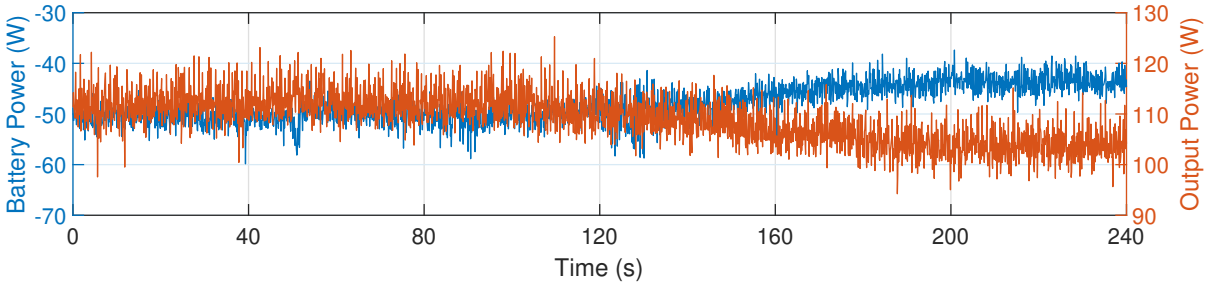

Figure 6.18: Battery power and output power during constant voltage charging (8 - 12 minutes).

Figures 6.19, 6.20 and 6.21 display the system's efficiency during the constant voltage charging mode. It is possible to notice that while the required power from the grid to charge the batteries decreases, the efficiency also decreases.

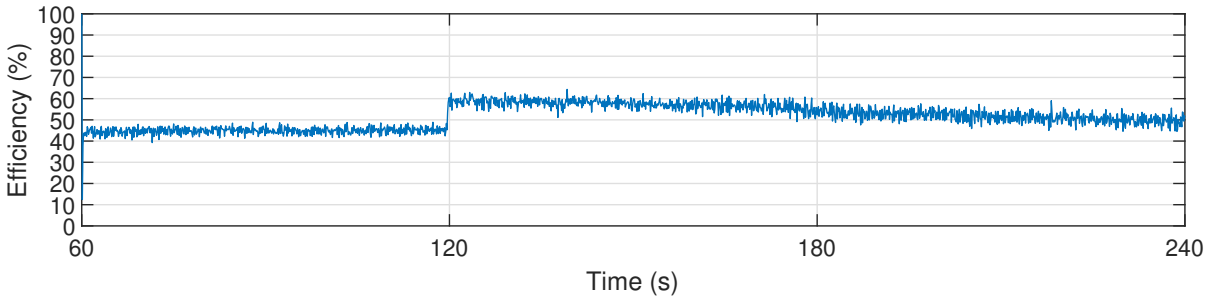

Figure 6.19: System's efficiency during constant voltage charging (2 - 4 minutes).

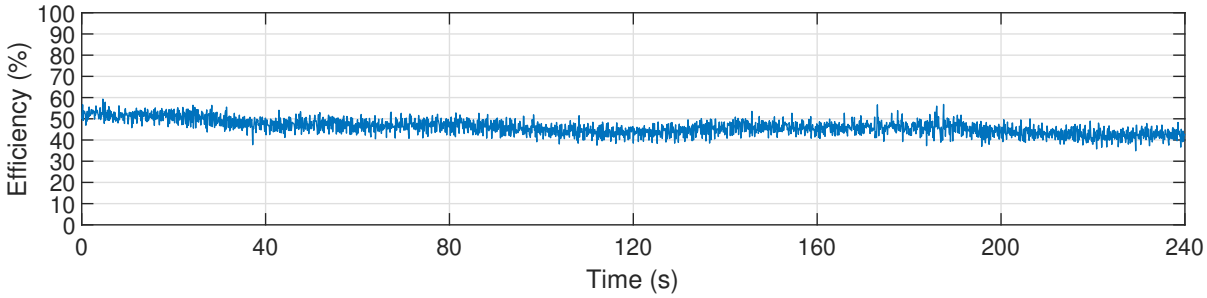

Figure 6.20: System's efficiency during constant voltage charging (4 - 8 minutes).

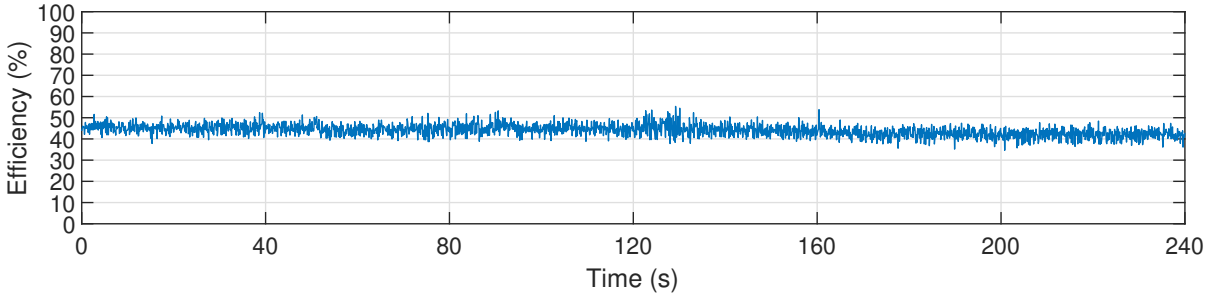

Figure 6.21: System's efficiency during constant voltage charging (8 - 12 minutes).

Figures 6.22, 6.23 and 6.24 display the DC Link voltage behaviour during the constant voltage charging mode. It is possible to assert that the operation is stable.

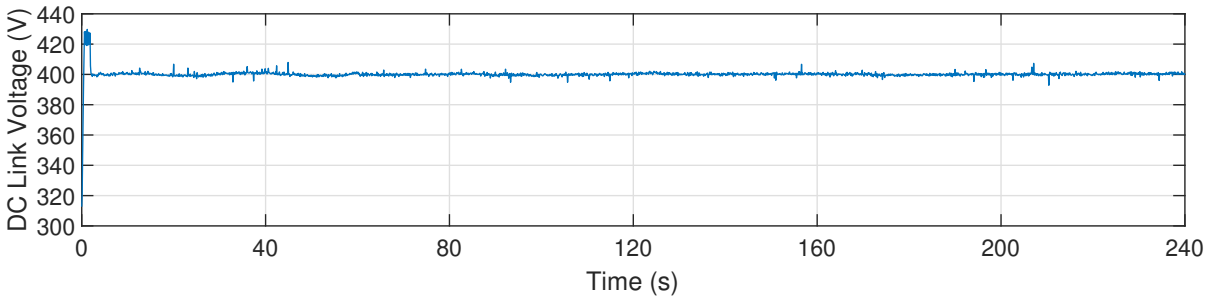

Figure 6.22: DC Link voltage during constant voltage charging (0 - 4 minutes).

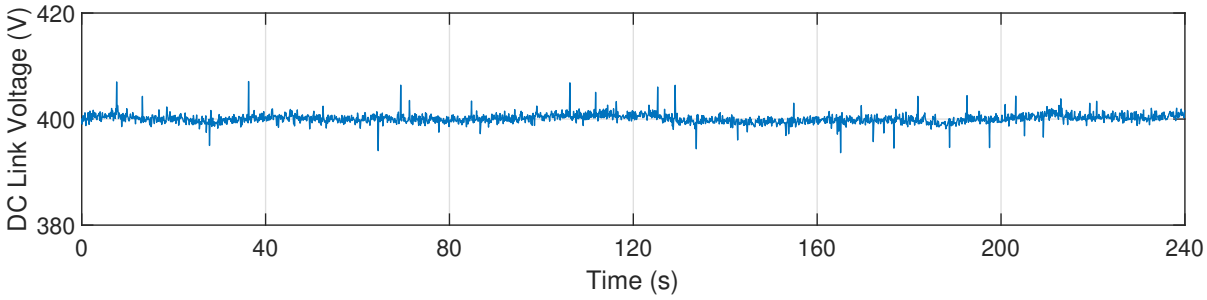

Figure 6.23: DC Link voltage during constant voltage charging (4 - 8 minutes).

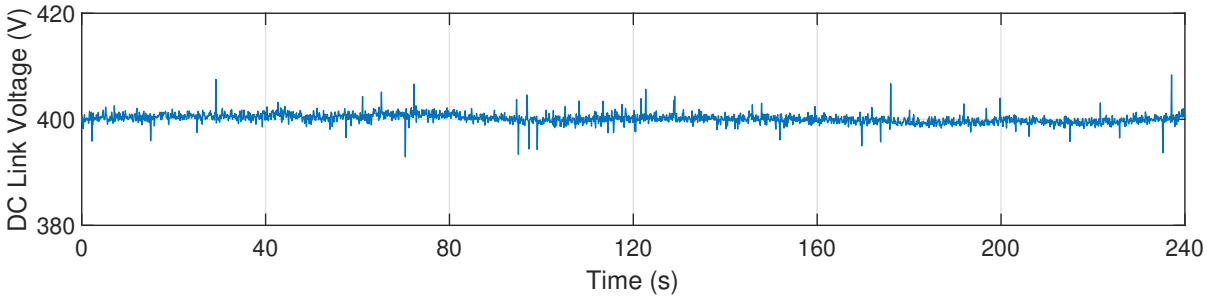

Figure 6.24: DC Link voltage during constant voltage charging (8 - 12 minutes).

Chapter 7

Data Analysis and Discussion

A few advantages of the implemented system can be mentioned, as the smooth transition between modes (detailed in section 7.2). The validation of the whole power structure (BDC and BADC), and the validation of the two different operation modes (V2G and G2V, both proposed by Leite, Ferreira, and Batista, lacking however the validation of the G2V mode [22]).

However, there are some improvements that could be made, for example the development of a SOC meter for developing new algorithms for charging the battery pack.

It is important to emphasize that the system's low efficiency displayed in each test (85% maximum for the V2G test in section 6.1, 80% maximum for the constant current charging in subsection 6.3.1 and 60% maximum for the constant voltage charging 6.3.2) might be explained by the low power ratings during the tests. It happens because the power module has a nominal current value of 75 A and a nominal voltage around 1200 V [44], and the maximum current reached during the tests was around 4 A, also, the maximum power extracted from the batteries was around 400 W, and the maximum injected power into the battery pack was around 300 W. Moreover, the high values of the duty cycle of the DC-DC converter contribute to the low efficiency level of the system.

In this chapter, both simulated and experimental results will be compared and discussed in the following sections, according to each test presented in chapters 5 and 6.

7.1 Vehicle-to-Grid test discussion

During the V2G operation mode, as can be shown in figure 5.5 in simulation, the battery SOC decreases. Although experimentally the battery SOC has not been measured, figure 6.1 shows that when the extracted current from the batteries increases, the voltage declines even more, and as the battery voltage is one of the SOC indicators, it is possible to conclude that the battery is discharging, as it should be in the discharging mode.

About the simulation performed tests, it is worthy to emphasize the inductor current variation as the output voltage ripple, and compare the results of those variations obtained by MATLAB with the values displayed in equations 4.2 and 4.3, respectively, which are the expected values of current variation and voltage ripple for the real application. Table 7.1 gives the obtained values via simulation. Those results are close enough from the results presented on section 4.4, and diverge a little from the results of equations 4.2 and 4.3 due to the change of the parameters on simulation. For example, the input voltage that in the simulation assumes the value displayed in table 7.1, instead of 100 V as presented on table 4.1. The experimental results for those variations were not observed.

Type	Inductor Current	Output Voltage
Peak to Peak	696 mA	91.9 mV
Mean	2.284 A	101.2 V
PtP/Mean	30.5 %	0.091 %

Table 7.1: Inductor current and output voltage variation for the V2G mode

Another interesting feature from figure 6.1 is the closeness of the battery current when compared to the reference current. As mentioned in section 6.1, one of the purposes of the V2G test is to evaluate the performance of the PI controller for a constant current mode. According to its results, it is notable that the controller performs pretty well, supplying the desired current for the BADC for injecting it into the grid.

Moreover, figure 6.3 shows the system's efficiency during this operation mode, which is noticeable according to figure 6.2 that the bigger the extracted power from the batteries, the bigger is the power injected into the grid and also is the system's efficiency. It happens because the higher the output power, higher is the current injected into the grid and smaller is the harmonic distortion of this current, avoiding more power loss in the system and increasing its efficiency [40].

7.2 Transition test discussion

The transition between the operation modes should occur as fast as possible and without any surges, because in a real system, as the experimental platform described in 4.4, those surges could damage any component, even the battery pack. As showed in figures 5.23 and 5.24 from simulation, and on figure 6.5 from the experimental tests, the properly transition was achieved due to the right attributed values for the proportional and integral constants of the PI controllers. Although figure 6.8 shows a surge in the battery current when the BDC turns on and starts to operate on V2G mode, this specific test was performed with different values from the presented ones in table 6.1, which are the final attributed values for the proportional and integral gains of the PI controllers. Additionally, the final performed tests in simulation can be seen in figures 5.28 and 5.29, and experimentally on figures 6.13, 6.14 and 6.15, which during the transition between the operation modes no surges occurs, as expected.

7.3 Grid-to-Vehicle test discussion

On this project, the battery charging process is very slow when compared with the DC fast charging levels of table 1.1. It happens because the battery is charged with a maximum current of 4 A. As explained in equation 3.11, with a charging current of 4 A, the battery would be fully charged only in 5 h (considering that it was fully discharged and the charging current of 4 A would be constant).

Therefore, as the charging process in this project has three stages in simulation (experimentally there are two charging stages), where the maximum charging current among the stages are 4 A, and it lasts for a few seconds (around 7 s), naturally the battery charges slowly. Furthermore, the simulation time range is restricted to 20 seconds due to the physical limitations of the used computer for the simulation. A bigger time range would provided a huge amount of data, demanding a higher processing capacity.

From the explanation about the slowness of the charging process, and all the battery power charts from chapters 5 and 6, it is possible to assert that the delivered power or absorbed by the batteries, it is a mirror of the delivered current or absorbed by the batteries, respectively. It happens because the battery voltage variation is very slow, that the voltage can be considered constant, and then, the power depends only of the current variation.

In the same way as in the V2G mode, it is important to compare the variations of the inductor current and the output voltage obtained via simulation with the displayed values in table 4.2. The results from simulation are also close enough to the results of equations 4.4 and 4.5, and diverge a little due to the change of the parameters on simulation.

Type	Inductor Current	Output Voltage
Peak to Peak	770 mA	94.3 mV
Mean	- 4.1 A	102.1 V
PtP/Mean	19 %	0.092 %

Table 7.2: Inductor current and output voltage variation for the G2V mode

7.3.1 Constant Current Charging test discussion

The G2V mode with constant current charging is the fastest approached charging method during the development of this thesis, because of the charging current assumes its maximum value and is constantly injected into the battery pack. In figure 5.7 (simulation),

the reference current value of the controller is smaller than the maximum specified one by the batteries manufacturer (4,25 A) [37], because of the simulation tests were performed aiming to be as close as the real system. However, as displayed on figure 6.8, the maximum used value for the controller reference current on the experimental tests was 3 A, and as in the V2G mode, the PI controller also performs properly for the constant current mode.

Figure 6.10 shows the system efficiency during the constant current charging operation mode, that was achieved by dividing the injected power into the batteries for the extracted power from the grid ("battery power" divided by "output power" on figure 6.9, considering the time range between the 10 s and the end of the experiment). The maximum efficiency is achieved when the batteries require the maximum power from the grid. In contrast, the maximum efficiency was achieved when the batteries were providing the maximum power, for the V2G mode.

7.3.2 Constant Voltage Charging test discussion

The G2V mode with constant voltage charging is the last step of the experimental tests, and the second to last of the simulation tests. Compared with the constant current charging, this is a slower method, as explained before in section 6.3.2.

For this specific test, the voltage controller only uses the proportional controller to generate the reference current for the current controller. The main reason is that initially the simulation tests were performed only with the proportional controller too, and for avoiding risks during the experimental tests, only the proportional controller was used. However, the simulation tests displayed in subsections 5.2.2, 5.2.3 and in section 5.4 shows the results with a PI controller. The experimental validation of the constant voltage charge with a PI controller is missing.

The slowness for the battery voltage to achieve the reference voltage, which can be seen on figures 6.12, 6.13, 6.14 and 6.15 is due the low attributed value for the proportional gain of the constant voltage controller, which is specified in table 6.1.

Figures 6.19, 6.20 and 6.21 show that the lower the charging current, the lower the efficiency. Consequently, while the real voltage value of the batteries approaches the reference one, the charging efficiency of the system decreases, and as a result, the majority of the power requested from the grid is dissipated in the BDC and in the BADC.

7.3.3 Float Charging test discussion

The third stage of the G2V mode comprises the last test of the simulation environment. And as displayed in figure 5.21, when it is compared to the other two stages of the charging mode, it is much slower than the both other cases.

For this test only a proportional controller was used in the voltage controller for generating the reference current of the current controller. The reason is due to the integral portion of the PI controller used initially, that was increasing the current value instead of decreasing it.

According to [1], the current should assume an even smaller value (between 8 mA and 12 mA), not the 600 mA as displayed on figure 5.18. However, due to the available inductor and capacitor values in the work station, which were the same values used for the simulation, the minimum value that the battery current can assume is around 400 mA while the buck converter works on continuous mode. For smaller values of current, the converter operates in discontinuous mode.

Although it has not been experimentally validated, the third step of the charging stage is similar to the second one, it only changes the reference voltage value and limits the charging current on a maximum of 600 mA. Consequently, the experimental validation of the second stage of the charging mode proves the feasibility of the third stage.

Chapter 8

Conclusion

Taking in consideration the wide dissemination of EV around the world, and considering them not only as loads, but also as distributed energy storage systems, which can provide services to the electric grid, the development of a control method for a bidirectional DC-DC converter (BDC) used for connecting those vehicles with the electric network was essential.

Using a non-isolated topology with only two switches for the BDC, the validation of the control method was successful, computationally and experimentally. The system dynamics was tested with the real-time controller board from dSPACE aforementioned in 4.4.1. However, for a real implementation of the system with commercial purposes, a Digital Signal Processor (DSP) should be used for controlling the power structure.

Although the charging/discharging algorithms were proposed by [22] and [23], the third stage of the G2V mode is not found in any of the literature cited in this thesis (although the float charging is not presented). However, all tests were validated via simulation, and as aforementioned on subsection 7.3.3, the validation of the constant voltage charging proves the feasibility of the float charging, because of the only differences between the methods are the reference voltage and the gains of the controllers.

Therefore, the power structure used and the proposed control algorithms for the BDC are capable of controlling the power flow between the battery pack and the electric grid, achieving the objective of this project.

8.1 Future Work

This section presents suggestions for future works related to the research approached during this project, with the objective of improving the bidirectional DC-DC converter performance for reaching better results.

- Experimental validation of the float charging mode;
- Improve the system's efficiency by increasing the operation frequency of the IGBTs and decreasing the inductor value;
- Development of a SOC indicator for developing more efficient charging and discharging algorithms.

Bibliography

[1] T. B. R. David Linden, *Linden's Handbook of Batteries*, 4th. New York: McGraw-Hill, 2011, ISBN: 978-0-07-162421-3.

[2] M. of Transport Jon Georg Dale. (). Norway and electric vehicles – a successful combination, [Online]. Available: https://www.regjeringen.no/en/aktuelt/norway-and-electric-vehicles--a-successful-combination/id2644216/. (accessed: 13.09.2019).

[3] M. Dundas. (). Can paris go 100% electric?, [Online]. Available: https://www.france24.com/en/20190412-down-earth-paris-electric-cars-scooters-pollution-france-transport-carbon-neutral. (accessed: 10.09.2019).

[4] S. Biswas. (). India turns to electric vehicles to beat pollution, [Online]. Available: https://www.bbc.com/news/world-asia-india-48961525. (accessed: 10.09.2019).

[5] IEA. (). Global ev outlook 2019, [Online]. Available: https://www.iea.org/publications/reports/globalevoutlook2019/. (accessed: 11.09.2019).

[6] ——, (). Electric vehicles - tracking clean energy progress, [Online]. Available: https://www.iea.org/tcep/transport/electricvehicles/. (accessed: 13.09.2019).

[7] P. Valdes-Dapena. (). The electric car revolution is coming. this is what has to happen first, [Online]. Available: https://edition.cnn.com/2019/07/18/cars/electric-car-market-sales/index.html. (accessed: 10.09.2019).

[8] C. E. Regulator. (). Market snapshot: Growing electric vehicle incentives in canada, [Online]. Available: https://www.cer-rec.gc.ca/nrg/ntgrtd/mrkt/snpsht/2018/01-03lctrcvhclncntvs-eng.html. (accessed: 13.09.2019).

[9] F. government of Germany. (). Tax incentives for electric cars, [Online]. Available: https://www.bundesregierung.de/breg-en/search/steuerliche-anreize-e-autos-1653722. (accessed: 13.09.2019).

[10] IEA. (). Electric vehicles initiative, [Online]. Available: https://www.iea.org/topics/transport/evi/. (accessed: 13.09.2019).

[11] W. Kempton and S. E. Letendre, "Electric vehicles as a new power source for electric utilities", *Transportation Research Part D: Transport and Environment*, vol. 2, no. 3, pp. 157–175, 1997, ISSN: 1361-9209. DOI: https://doi.org/10.1016/S1361-9209(97)00001-1. [Online]. Available: http://www.sciencedirect.com/science/article/pii/S1361920997000011.

[12] M. Ehsani, M. Falahi, and S. Lotfifard, "Vehicle to grid services: Potential and applications", *Energies*, vol. 5, no. 10, pp. 4076–4090, 2012, ISSN: 1996-1073. DOI: 10.3390/en5104076. [Online]. Available: https://www.mdpi.com/1996-1073/5/10/4076.

[13] J. Tomić and W. Kempton, "Using fleets of electric-drive vehicles for grid support", *Journal of Power Sources*, vol. 168, no. 2, pp. 459–468, 2007, ISSN: 0378-7753. DOI: https://doi.org/10.1016/j.jpowsour.2007.03.010. [Online]. Available: http://www.sciencedirect.com/science/article/pii/S0378775307005575.

[14] F. Mwasilu, J. J. Justo, E.-K. Kim, T. D. Do, and J.-W. Jung, "Electric vehicles and smart grid interaction: A review on vehicle to grid and renewable energy sources integration", *Renewable and Sustainable Energy Reviews*, vol. 34, pp. 501–516, 2014, ISSN: 1364-0321. DOI: https://doi.org/10.1016/j.rser.2014.03.031. [Online]. Available: http://www.sciencedirect.com/science/article/pii/S1364032114001920.

[15] A. Sharma and S. Sharma, "Review of power electronics in vehicle-to-grid systems", *The Journal of Energy Storage*, vol. 21, Nov. 2018. DOI: 10.1016/j.est.2018.11.022.

[16] B. Zhao, Q. Song, W. Liu, and Y. Sun, "Overview of dual-active-bridge isolated bidirectional dc–dc converter for high-frequency-link power-conversion system", *IEEE Transactions on Power Electronics*, vol. 29, no. 8, pp. 4091–4106, Aug. 2014, ISSN: 0885-8993. DOI: 10.1109/TPEL.2013.2289913.

[17] Y. Du, S. Lukic, B. Jacobson, and A. Huang, "Review of high power isolated bi-directional dc-dc converters for phev/ev dc charging infrastructure", in *2011 IEEE Energy Conversion Congress and Exposition*, Sep. 2011, pp. 553–560. DOI: 10.1109/ECCE.2011.6063818.

[18] Z. U. Zahid, Z. M. Dalala, R. Chen, B. Chen, and J. Lai, "Design of bidirectional dc–dc resonant converter for vehicle-to-grid (v2g) applications", *IEEE Transactions on Transportation Electrification*, vol. 1, no. 3, pp. 232–244, Oct. 2015, ISSN: 2332-7782. DOI: 10.1109/TTE.2015.2476035.

[19] P. Xuewei and A. K. Rathore, "Novel bidirectional snubberless naturally commutated soft-switching current-fed full-bridge isolated dc/dc converter for fuel cell vehicles", *IEEE Transactions on Industrial Electronics*, vol. 61, no. 5, pp. 2307–2315, May 2014, ISSN: 0278-0046. DOI: 10.1109/TIE.2013.2271599.

[20] S. Salehi Dobakhshari, J. Milimonfared, M. Taheri, and H. Moradisizkoohi, "A quasi-resonant current-fed converter with minimum switching losses", *IEEE Transactions on Power Electronics*, vol. 32, no. 1, pp. 353–362, Jan. 2017, ISSN: 0885-8993. DOI: 10.1109/TPEL.2016.2528893.

[21] Sang-Kyoo Han, Hyun-Ki Yoon, Gun-Woo Moon, Myung-Joong Youn, Yoon-Ho Kim, and Kang-Hee Lee, "A new active clamping zero-voltage switching pwm current-fed half-bridge converter", *IEEE Transactions on Power Electronics*, vol. 20, no. 6, pp. 1271–1279, Nov. 2005, ISSN: 0885-8993. DOI: 10.1109/TPEL.2005.857525.

[22] V. Leite, Â. Ferreira, and J. Batista, "Bidirectional vehicle-to-grid interface under a microgrid project", in *2014 IEEE 15th Workshop on Control and Modeling for*

Power Electronics (COMPEL), Jun. 2014, pp. 1–7. DOI: 10.1109/COMPEL.2014.6877175.

[23] J. G. Pinto, V. Monteiro, H. Gonçalves, B. Exposto, D. Pedrosa, C. Couto, and J. L. Afonso, "Bidirectional battery charger with grid-to-vehicle, vehicle-to-grid and vehicle-to-home technologies", in *IECON 2013 - 39th Annual Conference of the IEEE Industrial Electronics Society*, Nov. 2013, pp. 5934–5939. DOI: 10.1109/IECON.2013.6700108.

[24] A. Sgarbossa, R. Turri, G. Putrus, and G. Lacey, "A bidirectional power flow controller for evs to support the grid", in *2015 50th International Universities Power Engineering Conference (UPEC)*, Sep. 2015, pp. 1–6. DOI: 10.1109/UPEC.2015.7339939.

[25] P. Thomas and F. M. Chacko, "Electric vehicle integration to distribution grid ensuring quality power exchange", in *2014 International Conference on Power Signals Control and Computations (EPSCICON)*, Jan. 2014, pp. 1–6. DOI: 10.1109/EPSCICON.2014.6887512.

[26] M. A. Khan, I. Husain, and Y. Sozer, "A bidirectional dc–dc converter with overlapping input and output voltage ranges and vehicle to grid energy transfer capability", *IEEE Journal of Emerging and Selected Topics in Power Electronics*, vol. 2, no. 3, pp. 507–516, Sep. 2014, ISSN: 2168-6777. DOI: 10.1109/JESTPE.2014.2305157.

[27] E. Inoa and J. Wang, "Phev charging strategies for maximized energy saving", *IEEE Transactions on Vehicular Technology*, vol. 60, no. 7, pp. 2978–2986, Sep. 2011, ISSN: 0018-9545. DOI: 10.1109/TVT.2011.2162085.

[28] J. Xu, M. Gao, Z. He, J. Yao, and H. Xu, "Design and study on the state of charge estimation for lithium-ion battery pack in electric vehicle", in *2009 International Conference on Artificial Intelligence and Computational Intelligence*, vol. 3, Nov. 2009, pp. 316–320. DOI: 10.1109/AICI.2009.289.

[29] Tae-Ho Eom, Min-Ho Shin, Jun-Mo Kim, J. Lee, and Chung-Yuen Won, "Improved charge control algorithm considering temperature of li-ion battery", in *2017 IEEE 3rd International Future Energy Electronics Conference and ECCE Asia (IFEEC 2017 - ECCE Asia)*, Jun. 2017, pp. 1971–1975. DOI: 10.1109/IFEEC.2017.7992352.

[30] D. W. Hart, *Power Electronics*, 1st. New York: McGraw-Hill, 2010, ISBN: 978-0-07-338067-4.

[31] M. Jain, "Bi-directional dc -dc converter for low power applications", Master's thesis, Concordia University - Montreal, Québec, Canada, 395 Wellington St., Ottawa, Canada, Feb. 1998.

[32] K. Ogata, *Modern Control Engineering*, 5th. New Jersey: Prentice Hall, 2010, ISBN: 978-0-13-615673-4.

[33] Kiam Heong Ang, G. Chong, and Yun Li, "Pid control system analysis, design, and technology", *IEEE Transactions on Control Systems Technology*, vol. 13, no. 4, pp. 559–576, Jul. 2005, ISSN: 1063-6536. DOI: 10.1109/TCST.2005.847331.

[34] R. W. S. Alan V. Oppenheim, *Discrete-time Signal Processing*, 3rd. London: Pearson, 2014, ISBN: 978-1-292-02572-8.

[35] K. Divya and J. Østergaard, "Battery energy storage technology for power systems-an overview", *Electric Power Systems Research*, vol. 79, pp. 511–520, Apr. 2009. DOI: 10.1016/j.epsr.2008.09.017.

[36] C. Liu, K. T. Chau, D. Wu, and S. Gao, "Opportunities and challenges of vehicle-to-home, vehicle-to-vehicle, and vehicle-to-grid technologies", *Proceedings of the IEEE*, vol. 101, no. 11, pp. 2409–2427, Nov. 2013, ISSN: 0018-9219. DOI: 10.1109/JPROC.2013.2271951.

[37] Ultracell, *Battery ucg 20-12 ultracell datasheet*. [Online]. Available: http://www.ultracell.co.uk/products/ucg-batteries/12v (visited on 07/15/2019).

[38] P. M. Hunter and A. H. Anbuky, "Vrla battery virtual reference electrode: Battery float charge analysis", *IEEE Transactions on Energy Conversion*, vol. 23, no. 3, pp. 879–886, Sep. 2008. DOI: 10.1109/TEC.2008.926041.

[39] R. Zhang, M. Cardinal, P. Szczesny, and M. Dame, "A grid simulator with control of single-phase power converters in d-q rotating frame", in *2002 IEEE 33rd Annual IEEE Power Electronics Specialists Conference. Proceedings (Cat. No.02CH37289)*, vol. 3, Jun. 2002, 1431–1436 vol.3. DOI: 10.1109/PSEC.2002.1022377.

[40] M. M. Breve, "Implementation of a bidirectional grid interface for an electric vehicle", Jul. 2019.

[41] MathWorks, *Implement generic battery model*, https://www.mathworks.com/help/physmod/sps/powersys/ref/battery.html. (visited on 07/15/2019).

[42] dSPACE, *Ds1103 ppc controller board - hardware installation and configuration*, dSPACE GmbH, Technologiepark 25, 33100 Paderborn, Germany, Jun. 2009.

[43] ——, *Controldesk*, https://www.dspace.com/de/gmb/home/medien/product_info/controldesk_next_generation.cfm. (visited on 07/19/2019).

[44] Powerex, *Pm75rla120 intellimod l-series*. [Online]. Available: https://manualzz.com/doc/11267224/datasheet-for-pm75cl1b060-by-powerex (visited on 08/19/2019).

Appendix A

Original Project Draft

Proposta de tema para
Dissertação/Estágio/Projeto - Trabalho de Conclusão de Curso

Orientador da Instituição onde se realiza o trabalho:

Vicente Leite e Ângela Ferreira	avtl@ipb.pt e apf@ipb.pt

Instituição do orientador:

Instituto Politécnico de Bragança	Escola Superior de Tecnologia e Gestão

Co-orientador da Instituição parceira:

Alberto Oliveira	avdo@utfpr.edu.br

Instituição do co-orientador:

Universidade Tecnológica Federal do Paraná	Campus de Toledo

Curso ou cursos da Instituição do orientador onde se propõe que o trabalho seja realizado:

Mestrado em Engenharia Industrial - Ramo Engenharia Eletrotécnica

Aluno: João Jorge Teodoro Coelho

Título do trabalho:

Controlo de uma interface bidirecional para ligação à rede elétrica de veículos elétricos

Palavras chave:

Controlo de potência, conversores de energia, inversor bidirecional, V2G e G2V, microrredes

Objetivos:

Continuação de trabalhos anteriores relacionados com o controlo de uma interface bidirecional para ligação à rede elétrica de baterias de veículos elétricos, no contexto de microrredes, como elementos adicionais de acumulação de energia.

1/2

Descrição adicional:

O trabalho consiste, numa primeira fase, no estudo e análise do controlo de um inversor de tensão monofásico, para injeção da energia proveniente de uma determinada fonte na rede elétrica. Nesta fase, a análise será feita em Simulink (toda a estrutura) e experimentalmente (o inversor de tensão). Numa segunda fase, será implementado, no laboratório, o controlo do conversor DC/DC bidirecional. Por fim, deverá ser implementada, experimentalmente, toda a estrutura de potência.
O projeto deve basear-se na configuração apresentada na figura anexa, isto é, com um conversor DC/DC bidirecional, para ligação à bateria, seguido de um inversor de tensão monofásico para a ligação à rede de distribuição de energia elétrica.
O desenvolvimento do projeto inclui a simulação e validação do controlo da estrutura de potência da figura, em MATLAB/Simulink, bem como a sua implementação em laboratório utilizando o sistema de desenvolvimento da dSPACE, baseado numa carta de controlo em tempo real 1103.
O focus do trabalho deverá ser no controlo do inversor de tensão de interface com a rede elétrica, mas poderá vir a ser diferente, e a configuração poderá ser alvo de modificações. Estas eventuais alterações decorrerão da motivação específica e "skills" dos estudantes envolvidos, da evolução dos trabalhos, de constrangimentos laboratoriais e da análise dos resultados que forem sendo obtidos.

Metodologia/Plano de trabalhos:

O projeto incluirá as seguintes fase:
1. Estudo de algoritmos de conversão eletrónica de energia, para ligação à rede elétrica de energia proveniente de baterias;
2. Estudo de alguns algoritmos de carga de baterias;
3. Implementação e validação, em Simulink, de algoritmos de controlo, designadamente do inversor de tensão de interface com a rede;
4. Familiarização com o conversor eletrónico de potência baseado num kit da POWEREX com uma carta de interface e um módulo de potência;
5. Familiarização com o sistema de desenvolvimento da dSPACE baseado em Simulink e numa carta de controlo em tempo real;
6. Implementação e realização de testes experimentais;
7. Elaboração de relatório, devidamente estruturado, formatado e redigido.

Recursos necessários:

- Computador MATLAB/Simulink e sistema de desenvolvimento da dSPACE com carta de controlo em tempo real;
- Kit da POWEREX com uma carta de interface e um módulo de potência, que inclui o inversor de tensão;
- Bateria de veículos elétricos.

Appendix B

Other Appendix(es)

B.1 Simulink Model

B.1.1 Model Overview

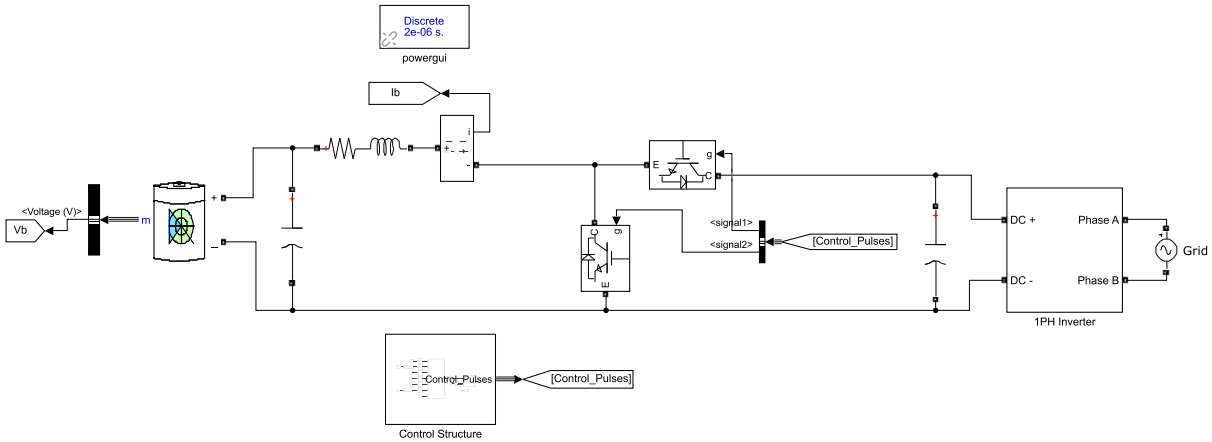

Figure B.1: Simulation Model Overview

B.1.2 Control Structure

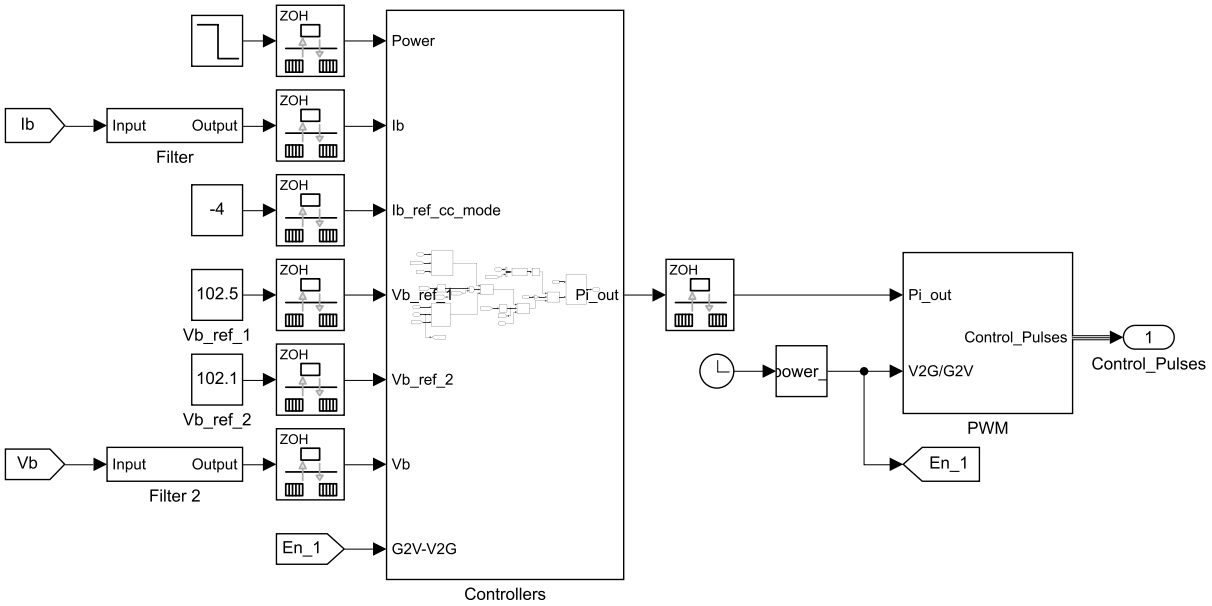

Figure B.2: Control Structure showing the PWM generator, and the variables used to control the BDC, likewise the variable used to determine the BDC operation mode

B.1.3 Controllers

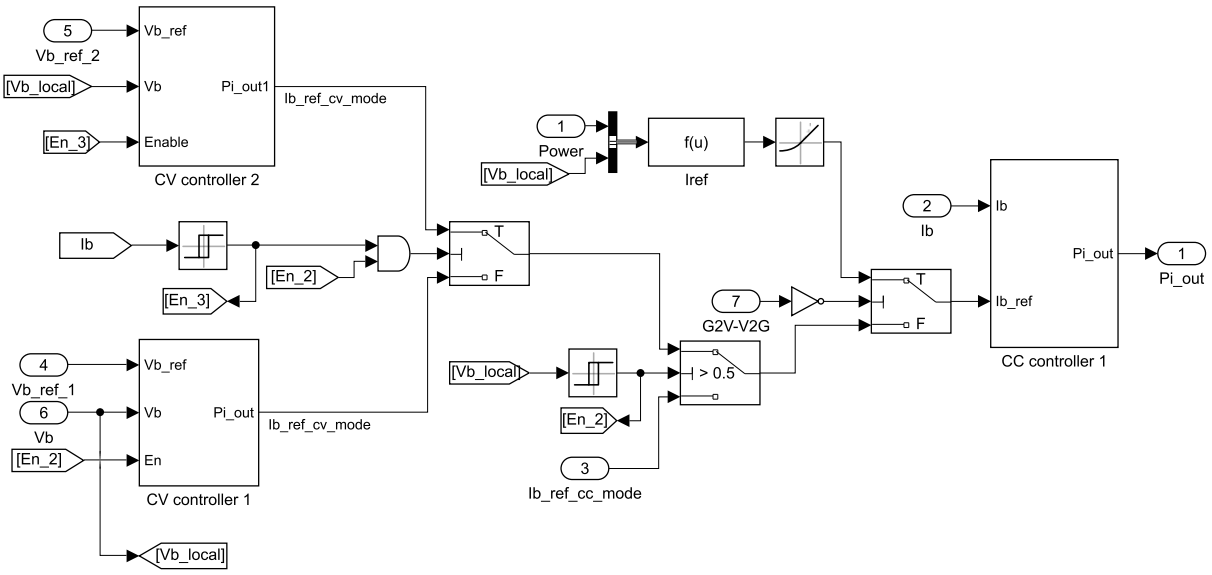

Figure B.3: Diagram of the controllers used for the BDC control

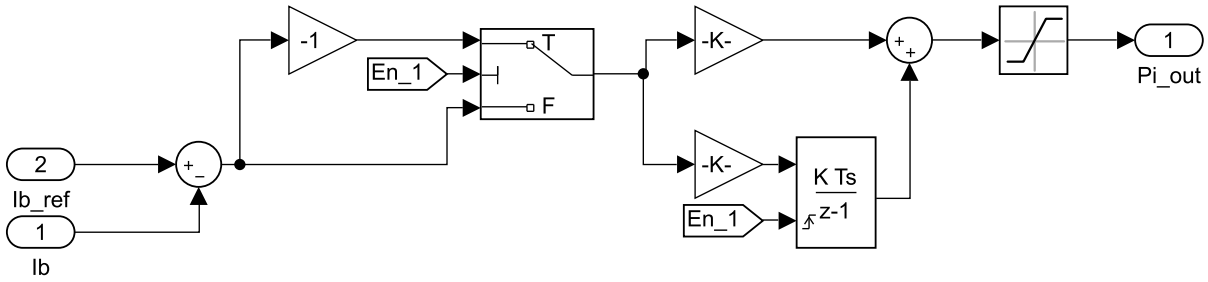

Figure B.4: Current controller used in the discharging mode and in the first stage of the charging mode

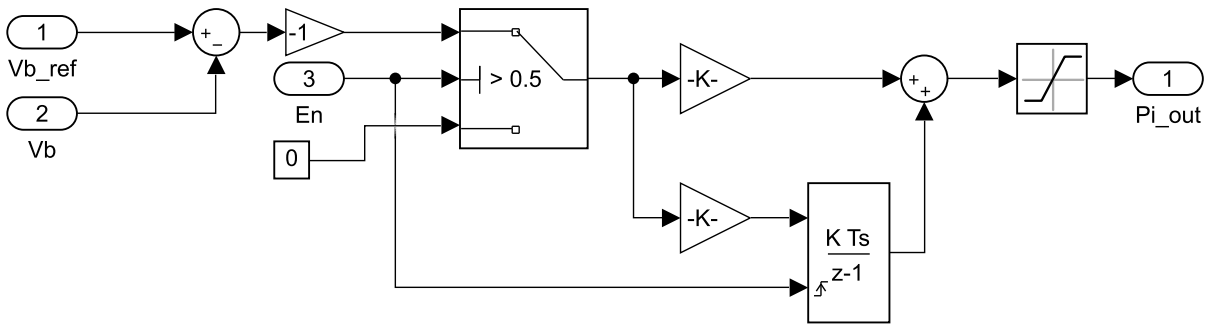

Figure B.5: First constant voltage controller used in the second charging stage

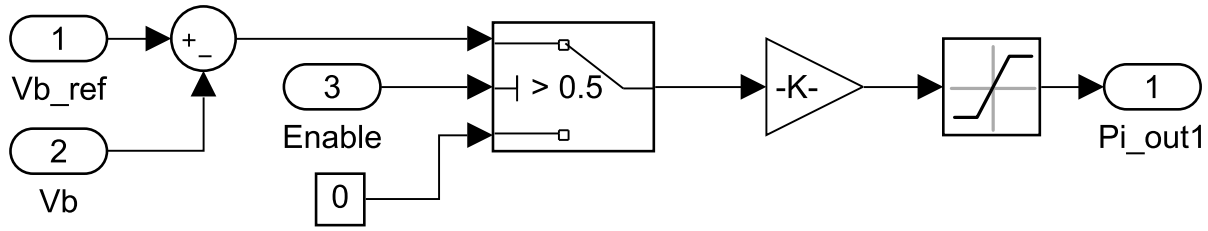

Figure B.6: Second voltage controller used in the third charging stage

B.1.4 Pulse-Width Modulator

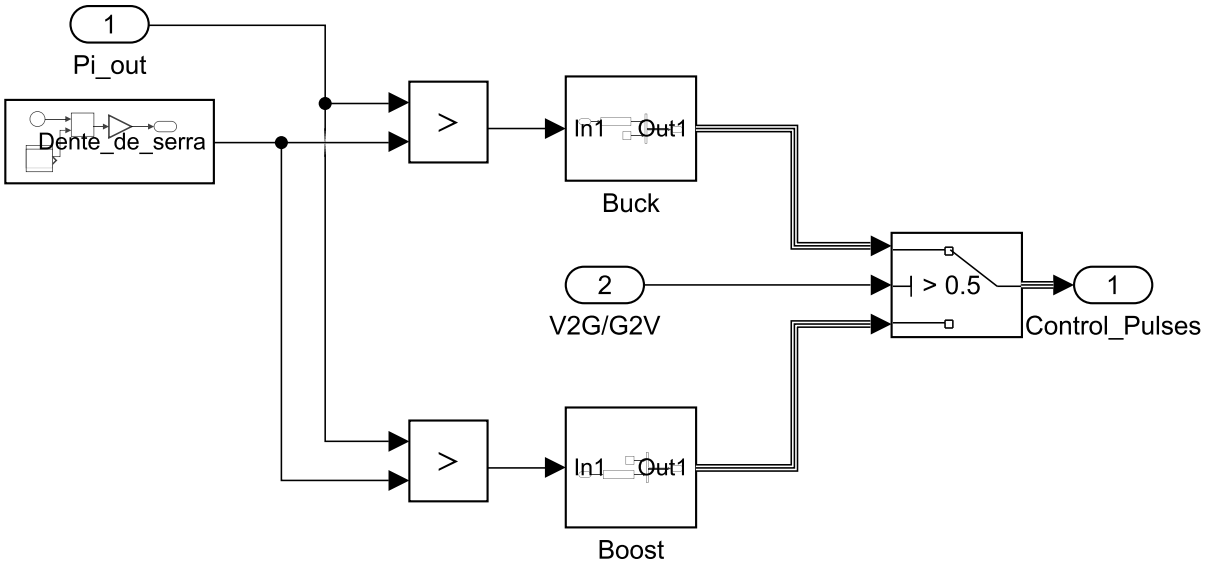

Figure B.7: PWM

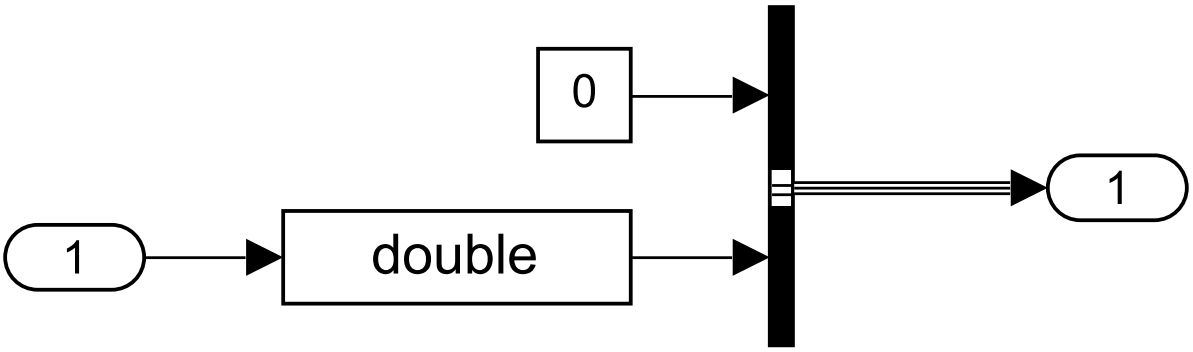

Figure B.8: Control pulses for switches S1 and S2 on discharging mode

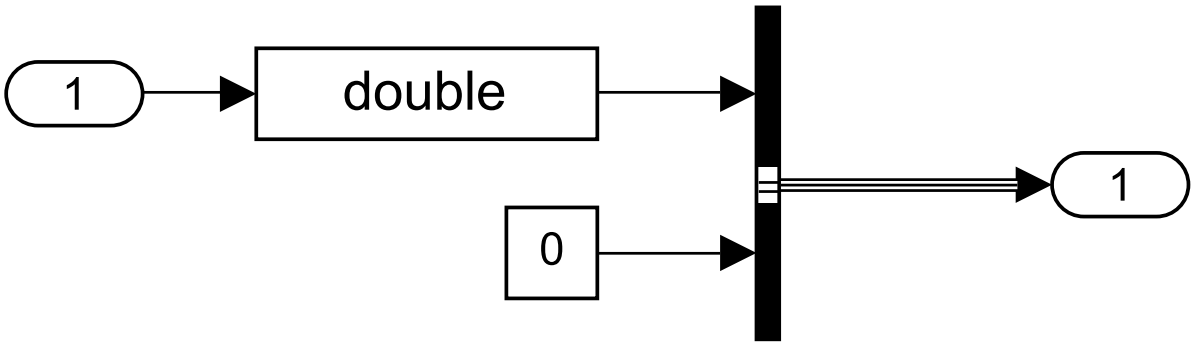

Figure B.9: Control pulses for switches S1 and S2 on discharging mode

B.1.5 Simulation Parameters

Parameter	Variable	Value	Unit
Simulation Parameters			
Power extracted from batteries	input_power	250	w
Physical parameters			
Sample time for PWM simulation	pwm_sample_time	2e-6	s
PLL			
PLL sampling time	pll_sampling_time	2e-6	s
	kSogi	0.2	-
	kom	0.2	-
DC bus			
Parallel resistance value	R_DC	1000	Ohm
Gains for the vDC controller	kp_vDC	0.1	-
	ki_vDC	5	-
Saturation values for the vDC controller	PI_max_dc	+15	-
	PI_min_dc	-15	-
BADC			
Gains for the PI controller	kp_iS	20	-
	ki_iS	30	-
Saturation values for the controller of the quadrature current	PI_max_iq	+330	-
	PI_min_iq	-330	-
Saturation values for the controller of the direct current	PI_max_id	+330	-
	PI_min_id	-330	-
BDC			
Saturation values for the current controller	PI_max_bb	1	-
	PI_min_bb	0	-
Saturation values for the 1st voltage controller	PI_max_cv_1	0	-
	PI_min_cv_1	-4	-
Saturation values for the 2ndvoltage controller	PI_max_cv_2	-0.3	-
	PI_min_cv_2	-0.6	-
Grid Parameters			
Grid frequency	grid_frequency	50	Hz
Grid peak voltage	grid_amplitude	325.27	V
Output filter resistance	R_grid	0.67	Ohm
Output filter inductance	H_grid	18e-3	H
Output filter capacitance	C_grid	1e-6	F

Table B.1: Simulation parameters